
Superconducting Single-Photon Detectors for Integrated Quantum Optics

Zur Erlangung des akademischen Grades eines
DOKTORS DER NATURWISSENSCHAFTEN
Von der Fakultät für Physik des
Karlsruhe Instituts für Technologie (KIT)

genehmigte

DISSERTATION

von

Dipl.-Phys. MPhys. Oliver Kahl

geboren in
Hillerød, Dänemark

Tag der mündlichen Prüfung:	29.01.2016
Referent:	Prof. Dr. Martin Wegener
Korreferent:	Prof. Dr. Wolfram Pernice

CONTENTS

Contents	2
Publications	5
Abbreviations.....	6
1 Introduction	8
1.1 Quantum Optical Integration.....	8
1.2 Single-Photon Generation.....	9
1.3 Single-Photon Detection	10
1.4 Scope and Aim of this Thesis.....	11
2 Fundamentals of Single-Photon Detection	12
2.1 Key Parameters in Single-Photon Detection.....	12
2.1.1 Detection Efficiency	13
2.1.2 Dark Count Rate and Noise-Equivalent Power	13
2.1.3 Recovery Time.....	14
2.1.4 Timing Jitter	14
2.1.5 Spectral Range	14
2.1.6 Photon Number Resolution	15
2.1.7 Concluding Remarks On SPD Performance Parameters	15
2.2 Select Examples of Established Single-Photon Detection Schemes	15
2.2.1 Photo-Multiplier Tube (PMT).....	15
2.2.2 Single-Photon Avalanche Diode (SPAD).....	16
2.2.3 Transition Edge Sensor (TES).....	17
2.2.4 Quantum-Dot-Based SPDs	18
2.2.5 Up-Conversion SPD	19
2.2.6 Visible Light Photon Counter (VLPC).....	20
2.2.7 Overview and Comparison.....	21
2.3 Superconducting Nanowire Single-Photon Detector.....	23
2.3.1 General Principle of Operation	23

2.3.2	Macroscopic SNSPD Detection Mechanism.....	24
2.3.3	Microscopic SNSPD Detection Mechanism.....	26
2.3.4	Spectral Sensitivity and Wire Cross-Section	41
2.3.5	Timing Characteristics.....	41
2.3.6	Enhancement of the Absorption Efficiency	42
2.3.7	Summary	42
3	SNSPD Integration and Characterization	44
3.1	Fundamentals of Integrated SNSPDs	44
3.1.1	Integrated Optics	45
3.1.2	Detection by Near-Field Coupling.....	48
3.1.3	Current State of Integrated SNSPD Research	48
3.2	Material Platform and Properties	49
3.2.1	Silicon Nitride (Si_3N_4).....	49
3.2.2	Niobium Nitride (NbN).....	50
3.3	Detector Design and Fabrication	50
3.3.1	Detector Geometry.....	51
3.3.2	Fabrication	52
3.4	Experimental Setup.....	56
3.4.1	Liquid Helium Flow Cryostat	56
3.4.2	Electronic Driving Circuit.....	58
3.5	Integrated SNSPD Characterization	59
3.5.1	integrated SNSPD Operation Conditions	59
3.5.2	On-Chip Detection Efficiency	59
3.5.3	Dark Counts and Noise-equivalent Power	62
3.5.4	Recovery Time.....	63
3.5.5	Timing Jitter	66
3.6	Concluding remarks on the Detector Characterization	68
4	Single and Multi-Photon Detection.....	70
4.1	Detection Regimes	70
4.2	Quantum Optical Methodology	71
4.2.1	Light Quantization and Photon States	71
4.2.2	Photon Number Statistics	73
4.2.3	Quantum Detector Tomography Basics.....	73
4.3	Experimental Implementation	76

4.4	Detection Regimes	76
4.4.1	Single-Photon Detection Regime	76
4.4.2	Multi-Photon Detection Regimes	77
4.5	Detector Response Extraction	79
4.6	Concluding Remarks.....	81
5	Single-Photon Spectrometry	82
5.1	Spectrometer Concept and Design	83
5.1.1	Basic Concept	83
5.1.2	Design and Parameterization.....	84
5.1.3	Transmission Optimization	85
5.1.4	Parameter Design.....	87
5.2	Multi-Channel Single-Photon Receiver at 1550 nm.....	89
5.2.1	Optical Characterization	89
5.2.2	Detector Characterization.....	90
5.2.3	Spectrally Resolved Single-Photon Detection.....	91
5.3	Single-Photon Spectrometer at 740 nm	92
5.3.1	Silicon Vacancies (SiVs)	93
5.3.2	Scanning Confocal Microscope	93
5.3.3	Spectrometer Characterization.....	95
5.3.4	Results and Discussion	96
5.4	Concluding Remarks.....	98
6	Conclusion and outlook	99
7	References	102
	Appendix.....	118
	Acknowledgments	121

PUBLICATIONS

- O. Kahl, S. Ferrari, V. Kovalyuk, G. N. Goltsman, A. Korneev, and W. H. P. Pernice, "Waveguide integrated superconducting single-photon detectors with high internal quantum efficiency at telecom wavelengths.," *Sci. Rep.*, vol. 5, no. February, p. 10941, 2015.
- O. Kahl, W. Pernice, S. Ferrari, P. Rath, A. Vetter, and C. Nebel, "High efficiency, on-chip single-photon detection for diamond nanophotonic circuits," *J. Light. Technol.*, vol. 8724, no. c, pp. 1–1, 2015.
- P. Rath, O. Kahl, S. Ferrari, F. Sproll, G. Lewes-Malandrakis, D. Brink, K. Ilin, M. Siegel, C. Nebel, and W. Pernice, "Superconducting single-photon detectors integrated with diamond nanophotonic circuits," *Light Sci. Appl.*, vol. 4, no. 10, p. e338, Oct. 2015.
- S. Ferrari, O. Kahl, V. Kovalyuk, G. N. Goltsman, A. Korneev, and W. H. P. Pernice, "Waveguide-integrated single- and multi-photon detection at telecom wavelengths using superconducting nanowires," *Appl. Phys. Lett.*, vol. 106, no. 15, p. 151101, Apr. 2015.
- V. Kovalyuk, W. Hartmann, O. Kahl, N. Kaurova, A. Korneev, G. Goltsman, and W. H. P. Pernice, "Absorption engineering of NbN nanowires deposited on silicon nitride nanophotonic circuits.," *Opt. Express*, vol. 21, no. 19, pp. 22683–92, Sep. 2013.

ABBREVIATIONS

AE	Absorption efficiency
AWG	Arrayed waveguide grating
BCS	Bardeen-Cooper-Schrieffer
BKT	Berezinskii-Kosterlitz-Thouless
CP	Cooper pair
cw	continuous-wave
EBL	Electron beam lithography
FEM	Finite element method
GC	Grating coupler
GL	Ginzburg-Landau
IQE	Internal quantum efficiency
IR	Infrared
MIBK	Methyl isobutyl ketone
NbN	Niobium nitride
NIR	Near-infrared
OCDE	On-chip detection efficiency
PMMA	Poly methyl methacrylate
PMT	Photomultiplier tube
PVD	Physical vapor deposition
QDT	Quantum detector tomography
QKD	Quantum key distribution
QP	Quasi-particle (Bogoliubon)
RIE	Reactive ion etching
SEM	Scanning electron microscope
Si ₃ N ₄	Silicon nitride
SiO ₂	Silicon dioxide
SiV	Silicon vacancy
SNSPD	Superconducting nanowire single-photon detector
SPAD	Single-photon avalanche diode
SPD	Single-photon detector
TES	Transition edge sensor
UV	Ultra-violet
VAP	Vortex-antivortex pair
VLPC	Visible light photon counter
VPS	Vortex-induced phase slip

1 INTRODUCTION

Photons constitute the energy quanta associated with electromagnetic radiation. They play one of the most fundamental roles in science, and more recently also technology. Single photons have been used with great experimental success in examining the foundations of quantum physics and in the realization of quantum information technology. The majority of current quantum optical experiments is, however, based on the use of numerous individually assembled optical components bolted down on optical tables and benches. The scalability, stability and achievable complexity of this approach are clearly limited. Further advances in quantum optical science and technology therefore necessitate photonic integration of all required optical components. In general, three component categories can be identified: single-photon sources which are able to deterministically generate individual photons on request; photonic circuitry which allows for the deliberate and targeted manipulation of single photons; and integrated single-photon detectors which are capable of reliable and accurate detection of individual photons. This thesis reports on the implementation and characterization of a recently developed fully integrated single-photon detector (SPD). Several detector circuits are realized and it is shown that the detectors exhibit supreme detection performance over a wide optical spectrum. Moreover, the immense scalability of the detectors is showcased by the integration and parallel operation of multiple detectors within a single integrated optical circuit. These demonstrations are essential for future developments in integrated quantum optics for quantum information technology and for the examination of fundamental quantum physics.

1.1 QUANTUM OPTICAL INTEGRATION

At the beginning of the 20th century when the concept of the photon was developed most notably by Planck [1] and Einstein [2] it simultaneously heralded a revolution in the understanding of our physical surroundings. Until then two theories were able to explain all physical phenomena known at the time – Newton’s laws of classical mechanics and Maxwell’s description of electrodynamics. Quantum mechanics expanded this view drastically. It very successfully predicts the behavior of nature at a microscopic level, which is sometimes counter-intuitive to our macroscopic perception. Toward the end of the 20th century, the notion developed that harnessing those unique quantum phenomena for technological applications holds much greater potential than the indirect and incomplete control over the quantum system inherent to conventional technology [3]–[7].

The fundamental challenge in the quantum approach is the inherent fragility of quantum systems. Decoherence caused by the susceptibility to external fluctuations and the difficulty in achieving isolated interaction often pose hardly surmountable limitations. In contrast, individual photons for

the most part lack the detrimental interaction with the environment and maintain their coherence over large distances. Photons are therefore ideal quantum objects for the implementation of quantum technology and, on a fundamental level, they can serve as prototypes for the observation and verification of the foundations of quantum mechanics.

The currently most vibrant field of quantum optical technology is that of quantum information in which the photon serves as information-carrying unit. The basic idea is to encode information in the photon's quantum state, for instance its two orthogonal polarization states. The most prominent examples of photon-based quantum information technology are quantum cryptography [8], [9] including quantum key distribution (QKD), which aims at securing information on a fundamental level [10], [11]; quantum communication which exploits the quantum non-locality of entangled states to transmit information [12]–[14]; and arguably the most ambitious goal, linear optical quantum computing (LOQC) which utilizes quantum phenomena to perform computations which are effectively intractable on a classical computer [15]–[20].

From the perspective of fundamental physical research, photons have proven invaluable for the observation and verification of quantum mechanical phenomena which are at the very foundation of our understanding of physics. Quantum entanglement and violations of Bell's inequality [21] which were motivated by the famous Einstein-Podolsky-Rosen Gedankenexperiment [22] were first demonstrated using entangled photons [23]–[26]. Newer developments include demonstrations of larger entangled systems [27], [28] and quantum teleportation [29].

Experimental implementations which utilize single photons, today, consist mostly of optical components which are assembled individually on optical tabletops and benches. Single-photon sources are usually realized in individual sub-circuits and detection is performed by stand-alone units. The approach offers considerable flexibility by being able to quickly adjust or expand the optical setup. However, continually growing demands on the size and complexity of such installations will eventually restrict the feasibility of tabletop implementations. Moreover, potential future commercialization mandates stability outside a laboratory environment. The currently most promising approach to resolve these challenges is miniaturization through integration into chip-scale photonic circuitry. Originally developed for applications in the telecommunications industry it is fully compatible for the use with single photons and likely to meet the demands for scalability, stability, and complexity of advanced quantum optical circuitry. While the integration of the photon-guiding and manipulating circuitry is relatively straightforward, the realization of fully integrated single-photon sources and single-photon detectors (SPDs) is more challenging.

1.2 SINGLE-PHOTON GENERATION

Single-photon sources can be realized by various approaches. The simplest, but approximate implementation is a heavily attenuated laser which produces *on average* one single photon per unit time. This allows for proof-of-principle analyses as we shall see later in this thesis. It is, however, not a true single photon source which is capable of exhibiting quantum interference phenomena. An ideal single-photon source is characterized by the ability to generate an individual photon *on demand* with subsequently generated photons being *indistinguishable* from the first one. Practical implementations of this concept usually employ a single, isolated emitter which is excited either optically or electrically in order to emit one photon upon relaxation. Typical emitters include

quantum dots [30]–[32], single molecules [33]–[35], single atoms [36], [37] or ions [38], or color centers in diamond [39]. However, the scalable integration of such sources is currently constrained by emitter differences which negate photon indistinguishability. Present research efforts are focused on the development of identical emitters. So far, successful demonstrations of identity were limited to emitter *pairs* including quantum dots [40], [41], trapped ions [42], [43], and trapped atoms [44], [45]. However, more than two identical emitters are yet to be realized, which, at present, disallows the scalable integration of deterministic single-photon sources. As such, single-photon sources must still be operated externally. The currently most readily available and thus most favored method is to produce degenerate pairs of single photons by spontaneous parametric down-conversion in a nonlinear optical crystal. Multi-pass configurations enable the generation of more than two indistinguishable photons [46] which are subsequently inserted into the on-chip optical circuit by standard chip-coupling methods which will be explained in detail later in this thesis.

1.3 SINGLE-PHOTON DETECTION

Single-photon detection is a much more mature field. Many schemes to detect single photons have been suggested and successfully implemented. The most prominent candidates, the photo-multiplier tube (PMT) and the single-photon avalanche diode (SPAD), even enjoy great commercial success. SPDs are, however, almost exclusively operated as external, stand-alone units. In 2001, a new type of SPD based on a superconducting nanowire was realized by Gol'tsman et al. [47]. This superconducting nanowire single-photon detector (SNSPD) offers reasonably good detection efficiency over a wide spectral range with outstanding timing characteristics in comparison to established SPD technologies [48]–[50]. The SNSPD's detector element is the nanowire itself. It is commonly fabricated by nano-patterning a sputter-coated thin film of a superconducting material on a semiconductor substrate [51]. One of the major benefits of this process is its compatibility with standard nanophotonic fabrication techniques. SNSPDs are, therefore, amenable to integration with photonic circuitry. Hu et al. [52] first proposed SNSPD integration in 2009 and implementations on gallium-arsenide [53], [54], silicon [55] and silicon-nitride [56] were realized in the early 2010s. Integration with lithium-niobate has also been suggested [57], but is yet to be realized. The integrated SNSPD is based on the nanowire interfacing directly with the on-chip photonic waveguide. It is therefore extremely compact and allows for a plethora of detectors on a single integrated photonic chip. The integration of SNSPDs thereby resolves the aforementioned challenges in scalability and circuit complexity which conventional tabletop implementations face.

Beyond the integration itself, on-chip SNSPDs benefit from new degrees of freedom which do not exist in conventional SNSPDs. In particular, liberties in the geometrical design of the nanowire allow for considerable improvements in the detection efficiency while maintaining the excellent timing characteristics of conventional SNSPDs. Integrated SNSPDs are therefore able to outperform many of the established SPD technologies in multiple aspects. This is particularly attractive for quantum information technologies like QKD and LOQC which are currently limited by the efficiency of available detectors [8], [48], [58]–[62]. Ultimately, the integrated SNSPD is a novel kind of detector with considerable potential for integrated quantum optical applications including quantum information and fundamental physical research.

1.4 SCOPE AND AIM OF THIS THESIS

Integrated SNSPDs are a novel, very potent detector technology. It is the focus of extensive research, yet its detection potential has not yet been fully exploited and its scalability never been demonstrated. This thesis addresses both of these aspects.

The integration of SNSPDs offers performance improvements beyond that of its older sibling and other well-established detection schemes. The dependence of the detector's performance on the geometrical design parameters as well as the operating conditions is assessed. A comparison shows that for on-chip applications integrated SNSPDs are indeed superior with respect to detection efficiency, noise level, timing accuracy, bandwidth and spectral range. Correlations between certain characteristics exist, such that trade-offs are possible, which allows for application-dependent parameter tuning. These results are important for the future development of SNSPDs on integrated quantum optical platforms as they allow for adequate, application-specific detector design.

Moreover, integrated SNSPDs are foundational for a new paradigm in quantum optics in which the detector is integrated together with the photonic circuitry. Parallel integration of eight detectors within one optical circuit is demonstrated for the first time. Two devices in different wavelength regimes are realized. One is operated at 1550 nm and can act as a multi-channel single-photon receiver; the other is designed for operation at 740 nm and serves as a single-photon spectrometer. Those demonstrations are landmark experiments which display the desired scalability of SPDs in integrated quantum optical circuitry.

The content of this thesis is structured in chapters as follows:

Chapter 2 introduces the terminology and the key parameters which are used to describe and assess SPDs in general. Several established and emerging SPD technologies are discussed. These serve as a reference for the comparison to the integrated SNSPD. The main part of the chapter is devoted to the conventional SNSPD. Its design and principle of operation will be addressed and the underlying physical concepts are reviewed.

Chapter 3 addresses the integration of the SNSPD with photonic circuitry. The integration principle and the design parameters are elucidated and the fabrication procedures are described. Several reference devices are characterized at 1550 nm using a cryostat measurement platform. The experimental platform and procedure are explained and the results are presented.

In chapter 4 a different measurement, referred to as quantum detector tomography, is performed in order to assess the detector response in more detail. In particular, the response to multiple photons is investigated. It is found that by adjusting the detector's operating conditions its sensitivity can be adjusted in order to react only to larger photon numbers.

Chapter 5 reports on the integration of multiple detectors in a single photonic circuit. The photonic circuit designs are explained and results of the implementations around 1550 nm and 740 nm are presented. Moreover, the spectrometer at 740 nm is used in combination with a confocal microscope to collect spectral, temporal and spatial fluorescence data from a cluster of diamond color centers.

2 FUNDAMENTALS OF SINGLE-PHOTON DETECTION

This chapter provides a general introduction into the field of single-photon detection. The key parameters and the terminology used in describing single-photon detectors (SPDs) are introduced. A few select examples of established and emerging SPD technologies are examined in order to illustrate the current detection potential and deficiencies. Subsequently, one particular emerging detector, namely the superconducting nanowire SPD (SNSPD), is analyzed in more detail. It offers considerable potential and remedies some of the deficiencies of the current detector establishment. It also serves as the basis for the integrated SPDs which are at the core of this thesis.

2.1 KEY PARAMETERS IN SINGLE-PHOTON DETECTION

Electromagnetic radiation has the remarkable capability to transport energy through space without the need for a carrier medium. In order to detect and measure this energy, detector elements are needed which couple to the electromagnetic wave and convert its energy into a more easily quantifiable form which is usually electrical. Many different mechanisms for such a conversion exist including photoresistors, photodiodes, thermocouples, chemical detectors, solar cells, etc. Each detection mechanism exhibits individually different features in terms of sensitivity, speed, spectral range, temporal accuracy, etc. In this regard, SPDs are mainly photodetectors, which exhibit an extremely high level of sensitivity. While many conventional detection mechanisms show linear sensitivity down to the picojoule per second range and even below, various sources of noise inherently preclude deterministic sensitivity to individual photons which, in the visible or NIR, carry energy in the range of 10^{-19} J. SPDs, therefore, utilize alternative procedures to increase sensitivity while keeping noise levels minimal.

Not only the physical mechanism to detect photons is different in SPDs, but also the information gained. Conventional photodetectors measure the flux of radiation incident on a detection element of a certain area. The optical energy collected over the time of measurement is converted into an electrical signal and eventually presented to the user. SPDs are fundamentally different in this regard as they do not *measure* power; instead they *count* individual energy packets of size $\hbar\omega$, i.e. single photons. In other words, conventional photodetectors produce an *analog* output signal which is

ideally proportional to the incident optical power while SPDs respond *digitally* indicating merely the presence or absence of individual photons. Noteworthy exceptions are number-resolving SPDs which are capable of discriminating numbers of photons up to a certain limit. In the following the key parameters which are generally used to describe the performance of SPDs are introduced.

2.1.1 DETECTION EFFICIENCY

As was mentioned above, SPDs do not measure optical power, they count individual photons. The single-photon detection event is, therefore, commonly referred to as *count*. The detection efficiency η is defined accordingly as the overall probability of registering a count when a photon arrives at the detector [49]. Experimentally, such probability is obtained by sending a well-calibrated number of photons onto the SPD and recording the number of counts. The ratio of the number of counts and the number of incident photons yields the detection efficiency. Often this measurement is performed not with fixed numbers, but with fixed rates such that it is not talked about photon numbers and absolute counts, but about photon flux and count rates:

$$\eta_{de} = \frac{R_c}{\Phi} \quad 2.1.1-1$$

where R_c denotes the detector count rate and Φ is the photon flux incident on the detector.

In most cases, the detection efficiency can be further divided into two independent components: the probability of the photon coupling to and exciting the detecting element is commonly referred to as *external efficiency* η_{ext} , whereas the probability of the detecting element producing a count after excitation is usually called *internal efficiency* or *quantum efficiency* η_{int} [48], [49]. The overall detection efficiency is subsequently the product of those two probabilities

$$\eta_{de} = \eta_{ext} \times \eta_{int} \quad 2.1.1-2$$

The individual contributions of internal and external efficiency depend on the individual detection mechanism and design.

Beside the detection efficiency η_{de} , the system efficiency η_{se} may be equally important in the assessment of detection performance. Particularly in fiber coupled systems, the photon transport from the source to the detector may be lossy, such that an additional contribution, usually called coupling efficiency η_c must be considered. It follows for the description of the complete system efficiency

$$\eta_{se} = \eta_c \times \eta_{de} = \eta_c \times \eta_{ext} \times \eta_{int} \quad 2.1.1-3$$

2.1.2 DARK COUNT RATE AND NOISE-EQUIVALENT POWER

Almost all SPD mechanisms exhibit a non-zero probability to record counts even in the absence of photons [48], [49]. Such false counts are commonly referred to as *dark counts*. Their origin is manifold: beside external instabilities of the detection system including mostly its susceptibility to electrical noise, internal factors such as material defects or impurities in the detecting element give rise to dark counts. The exact source of dark counts as well as its magnitude depends on the individual detection mechanism. A third contribution arises from black-body background radiation which occurs predominantly in detectors designed for longer wavelengths. Dark counts from black-

body photons are different from the usual dark counts as they do, in fact, originate from real photons. These parasitic photons must be filtered out in order to reduce their dark count contribution.

In general, dark counts can be regarded as noise which has to be overcome by a count rate signal in order to be measurable. The relative magnitude of count rate and dark count rate is commonly referred to as *signal-to-noise ratio* (SNR) and can serve as a simple metric to describe a detector's sensitivity. It does, however, not account for differences in detection bandwidth which differs from detector to detector. In order to allow for comparisons among detectors of different bandwidths, the *noise-equivalent power* (NEP) [48] is commonly used. It is given by

$$NEP = \frac{\hbar\omega}{\eta} \sqrt{2R_{dc}} \quad \text{2.1.2-1}$$

where η denotes the detection efficiency introduced above, and R_{dc} is the detector dark count rate. It describes the detector's sensitivity and commonly serves as a general figure of merit.

2.1.3 RECOVERY TIME

The detector recovery time – sometimes also called *dead time* – is the duration after the detection of a photon, which the detector needs to reset to a state in which it can reliably detect the next photon [48], [49]. The factors which influence the detector recovery time vary significantly from one detector design to the other. In some cases, the recovery time is not limited by the detection mechanism itself, but by the detector's electronic circuitry. The recovery time limits the maximum count rate or bandwidth of the detector.

2.1.4 TIMING JITTER

The timing jitter represents the temporal uncertainty in the time interval between the arrival of a photon and the generation of the electrical output signal [48], [49]. Commonly, the timing jitter is quantified by the full width at half-maximum (FWHM) of the temporal distribution which represents the uncertainty. Additionally, information about the type of statistical distribution itself (Gaussian, Lorentzian, arbitrary...) must be provided since not all detectors obey the same statistics. Depending on the physical processes involved in the detection mechanism timing jitters can vary significantly.

2.1.5 SPECTRAL RANGE

The spectral range refers to the variation of the detection efficiency with photon energy or wavelength. Physically, it is defined as the spectrum of photon energies which is capable of coupling to and exciting the detector element [50]. Most detectors exhibit a characteristic spectral range which is determined by the constituent materials and the physical mechanism employed for the detection process. The most common example is the bandgap limitation in semiconductor-based detectors. Most SPD technologies are designed either for the visible regime or the near-infrared (NIR). In the visible well-established SPD technologies exist and detection efficiencies are good. In the NIR spectrum the number of efficient SPDs declines and beyond the telecom wavelengths around 1550 nm available detector technologies become increasingly scarce.

2.1.6 PHOTON NUMBER RESOLUTION

Most SPDs are inherently binary devices: they detect either the presence or absence of photons. In this regard, presence refers to the detection of *one or more* photons in the case of almost all SPDs. Very few SPDs have the inherent capability to discriminate photon numbers, i.e. the electrical output signal magnitude is directly dependent upon the number of photons absorbed by the detector [48]–[50]. In the case of non-photon-number-resolving SPDs additional pre-selection equipment such as spatial or temporal multiplexers can be employed to achieve photon number resolution.

2.1.7 CONCLUDING REMARKS ON SPD PERFORMANCE PARAMETERS

The parameters introduced above quantify the salient performance aspects of SPDs. They are universally applicable and thus allow for a direct comparison of different SPD technologies. Within this thesis, they will serve as basis for the characterization and comparison of the fabricated detectors.

2.2 SELECT EXAMPLES OF ESTABLISHED SINGLE-PHOTON DETECTION SCHEMES

In order to gain a better understanding of the benefits and advantages of SNSPDs, it is useful to provide a reference frame to compare them to. In this section, a brief summary of a few established and emerging SPD technologies is provided. While there are numerous variations in the specific layout and design of the detection schemes, the focus is on the basic principles of the technologies.

2.2.1 PHOTO-MULTIPLIER TUBE (PMT)

2.2.1.1 PRINCIPLE OF OPERATION

The PMT was first demonstrated in 1949 and is thus the first detector which achieved resolution down to the single-photon level [63]. Today, various versions of PMT units are commercially available and their use is wide-spread in scientific as well as industrial applications.

The general principle of operation is based on the photoelectric effect: the PMT's detector element is a photocathode from which electrons can be dislodged by the absorption of photons – one photon liberates one electron (see Figure 2.2-1). The freed electron is accelerated onto a sequence of dynodes on each of which additional electrons are liberated. The entire set of electrons (usually $\sim 10^6$ electrons [49]) forms an electrical pulse upon collection on the anode, which can be amplified and

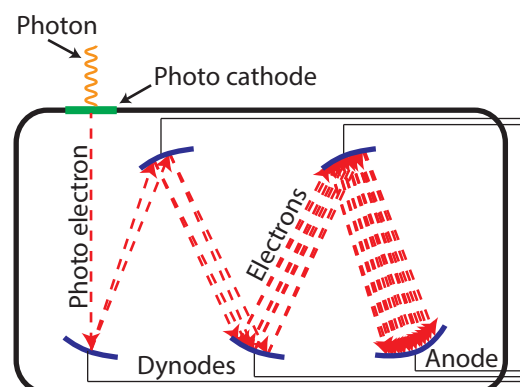


Figure 2.2-1: Schematic view of a PMT showing electron multiplication process (red dashed lines).

evaluated using standard electronic read-out equipment. The final pulse's magnitude is, in general, only weakly dependent upon the incident photon number, yet by choosing appropriate dynode materials the photon number dependence can be increased to levels at which the PMT effectively becomes number-resolving [64], [65]. The multiplication process itself is based on high operating voltages in the kilovolt range and requires ultra-high vacuum conditions, which significantly impairs device lifetime, reliability and scalability.

2.2.1.2 SPECTRAL RANGE AND EFFICIENCY

The spectral response of PMTs is limited by the cathode material's work function: the photoelectric effect necessitates photon energies above the work function in order to dislodge a photoelectron. The efficiency is, therefore, mostly determined by the chosen cathode material.

In the ultraviolet and visible regime from 230 nm to 900nm, bi-alkali, multi-alkali, GaAs, and GaAsP are predominantly used. Maximal efficiencies vary between 15% and 40% depending on the material and there exists a trade-off between spectral range and efficiency [50]. In the NIR between 1.0 and 1.7 μm , InGaAs, InGaAsP, and InP – sometimes in combination – make up the photocathode. The achieved efficiencies are rather poor and barely exceed a few percent.

The noise incurred during the multiplication process is mainly due to thermionic emission from the photocathode or the dynodes. Although acceptably low in bi-alkali-based PMTs, in multi-alkali and InGaAs-based PMTs thermionic emission causes dark count rates in excess of 10,000 counts per second [50]. As a consequence, Peltier cooling is used to lower the operation temperature. In addition to noise issues, the PMT is plagued by *afterpulsing*, i.e. an additional false pulse following the original photon-triggered pulse, from the ionization of residual gases in the vacuum tube. Extensive operation times at strong illumination can reduce the afterpulsing effect due to ion-trapping at the electrodes, yet permanent reduction remains to be seen.

2.2.1.3 TIMING CHARACTERISTICS

The PMT dead time is on the order of several nanoseconds. Its timing resolution is decent in the visible with a FWHM jitter value of 140 ps for multi-alkali photocathodes and 200-350 ps for GaAsP photocathodes, yet less optimal in the near-infrared with jitter values around 1 ns [50]. The timing uncertainty is mainly due to the transit time spread, i.e. the variation in the time it takes the electron pulse to propagate from cathode to anode. The differences in transit time are predominantly determined by random emission directions, velocities, and locations of the initial photoelectron.

2.2.2 SINGLE-PHOTON AVALANCHE DIODE (SPAD)

2.2.2.1 PRINCIPLE OF OPERATION

SPADs follow a similar concept as PMTs: an individual photon creates charge which multiplies and is eventually collected and read out in an external circuit. The difference is that instead of the liberation of an electron through the *external* photo-electric effect, the SPAD uses a semiconductor P-N or P-I-N junction in which an electron-hole pair is created through the *internal* photo-electric effect [50], [66], [67]. The charges are multiplied by reverse-biasing the diode beyond its breakdown voltage: the applied electric field accelerates the charges and transfers sufficient kinetic energy to

dislodge additional charges which are, in turn, accelerated themselves and create even more free charges [49], [68]–[70]. The mode of operation is commonly referred to as *Geiger mode* and the multiplication process is known as *avalanche effect*. The charge multiplication due to the avalanche effect is self-sustaining and must be stopped deliberately by external quenching circuitry.

2.2.2.2 SPECTRAL RANGE AND EFFICIENCY

The two most often utilized diode materials are silicon for visible light achieving efficiencies up to 65% [71] and InGaAs for near-infrared applications around 10% detection efficiency [66], [72]. Two standard designs are commonly realized: one featuring a thick junction (depletion area) to boost efficiency, the other utilizes a thinner junction in order to reduce dark counts [50]. Room temperature operation of SPADs usually introduces large amounts of dark counts such that thermoelectric coolers are typically employed to enable diode temperatures as low as 100 K [49], [66], [73]. At these temperatures dark count rates below 10 Hz are achieved, but the electronic noise incurred during the multiplication process prevents photon-number resolution.

In addition, the incomplete depletion of charge carriers from the active element can easily trigger unwanted second avalanches leading to afterpulses. In order to reduce SPAD afterpulsing, either long waiting times, i.e. recovery times, are needed or gated mode operation is chosen [74]. The afterpulsing effect is particularly severe in IR-SPADs.

2.2.2.3 TIMING CHARACTERISTICS

Depending on the mode of operation – passively quenched or gated – maximal count rates vary between a few and 100 MHz [48]–[50]. The timing jitter varies strongly depending on the particular design: shallow junction SPADs show excellent jitter values below 50ps, whereas the timing jitters of thick junction devices are almost an order of magnitude larger [48]. In addition, the applicability of SPADs in quantum information applications is further limited by so-called *backflash photons* resulting from the relaxation of hot avalanche electrons [75] and scalability is clearly limited.

2.2.3 TRANSITION EDGE SENSOR (TES)

2.2.3.1 PRINCIPLE OF OPERATION

Transition edge sensors (TESs), in contrast to PMTs and SPADs, are bolometers, i.e. the detection mechanism is based on a rise in temperature rather than the direct creation of charge [48]–[50], [76], [77]. As the name implies, TESs are detectors which are operated at the edge of the *resistance-free* superconducting to *resistive* normal-conducting transition: when cooled down to a point barely below the critical temperature, any small perturbation of the system will initiate the transition to the normal-conducting phase and thus cause an enormous increase in ohmic resistance. The dimensions of a TES are chosen such that the absorption of a single photon provides sufficient *heat* to the system to induce said transition and, thereby, increase its resistance. Under suitable electrical biasing conditions the voltage signal associated with the increase in ohmic resistance can be read out and amplified using SQUID¹ circuitry. TESs commonly employ tungsten as their superconducting

¹ SQUIDs are *superconducting quantum interference devices* which are commonly used to measure ultra-small magnetic fields [50], [130], [137].

active element and must thus be operated at temperatures around 100mK which necessitates elaborate cooling techniques.

One particularity pertaining specifically to TESs is that the extent of the transition depends on the degree of perturbation [78]. In other words, the increase in electrical resistance is determined by the energy supplied by the photon. The TES is, therefore, one of the few SPDs which is sensitive not only to the presence or absence of a photon, but also its energy (see Figure 2.2-2). In turn, if the TES is used only with photons of one particular energy, the output signal scales directly with the number of photons absorbed thus making the TES a truly number-resolving detector.

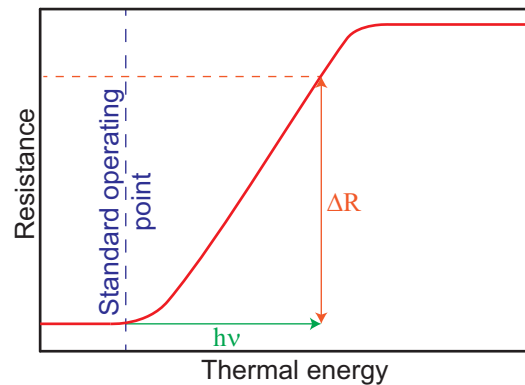


Figure 2.2-2: TES principle of operation: Photon absorption leads to increase in resistance proportional to the absorbed energy.

2.2.3.2 SPECTRAL RANGE AND EFFICIENCY

Due to the superconductivity-based detection mechanism which requires only small amounts of energy to produce relatively large, well-measurable signals, TESs exhibit fair detection efficiencies of up to 20% over a broad range from 350 nm to at least 1,550 nm [48], [50]. Additional degrees of freedom in the geometrical design allow the TES to be situated inside a resonant cavity which significantly enhances the detection efficiency. In the latter case, efficiencies of up to 95% have been realized [79]. The intrinsic dark count rate of a TES can be as low as 10 Hz, yet in most practical applications it is raised by additional dark counts from room temperature black body radiation [80].

2.2.3.3 TIMING CHARACTERISTICS

Contrary to the excellent detection efficiency, the TES's timing characteristics are rather poor. The detector's dead time is determined by the thermal recovery of the superconducting element which is on the order of a microsecond. At higher transition temperatures, the recovery times can be reduced, yet faster SQUID read-out electronics are required [81]. The timing jitter is similarly poor at 100 ns FWHM [57].

2.2.4 QUANTUM-DOT-BASED SPDS

2.2.4.1 PRINCIPLE OF OPERATION

A less common approach toward SPD utilizes the trapping of charge in quantum dots² (QDs). The basic layout is a field-effect transistor (FET) structure with an absorber and a thin QD layer between the gate electrode and the conduction channel [82]–[86]. Photo-excited charges from the absorber propagating toward the collector or emitter become trapped in the QD layer which shields the gate potential and effectively alters the channel conductance. By monitoring the channel current, the

² Quantum dots are semiconductor nanoparticles with dimensions of a few nanometers which confines the charge carriers in all three spatial dimensions.

absorption of a single photon can thus be registered. The conductance increase will self-reset when the trapped charge has been removed or has recombined. Both concepts – hole-trapping as well as electron-trapping – have been successfully demonstrated.

A similar approach is based on the enhancement of resonant tunneling through a semiconductor hetero-structure double-barrier [87], [88]. In the unexcited state, the resonance condition is not met such that tunneling is maximally suppressed. The photo-generation of an electron-hole pair by photon-absorption leads to the trapping of the hole in a QD. The trapped hole induces a field in the QD layer which shifts the structure closer to resonance and drastically increases the tunneling rate.

As such, both QD-based SPD schemes are sensitive to the number of holes trapped in the QDs which, in turn, reflects the number of photons absorbed. QD-based SPDs have, therefore, demonstrated photon-number-discriminating abilities although this may require cryogenic cooling to 77 K or even 4.2 K [49].

2.2.4.2 SPECTRAL RANGE AND EFFICIENCY

The spectral sensitivity of QD-based SPDs depends strongly on the individual detector design and can span from the visible into the near-infrared and in one extreme case even the far-infrared [89]. Efficiencies in the visible reach values of up to 68% in the case of QD-based FET structures and 12% in tunneling structures.

2.2.4.3 TIMING CHARACTERISTICS

As these devices are still in their infancy, many device characteristics and parameters have yet to be investigated. The timing performance of one tunneling structure has been reported as rather poor at several hundred nanoseconds recovery time and timing jitter values around 1 ns [87].

2.2.5 UP-CONVERSION SPD

2.2.5.1 PRINCIPLE OF OPERATION

In contrast to the previous detection schemes, SPD through parametric up-conversion does not constitute a detector per se, but a means of converting low energy photons which are more difficult to detect into more easily detectable high energy photons [48]–[50]. The idea is to utilize a crystal with a pronounced second order nonlinearity, such as periodically poled lithium niobate [90], in combination with a strong pump laser at frequency ω_p . Individual photons ω_i incident on the crystal will undergo a parametric conversion process in which a new photon of the sum of the incident photons' frequencies is generated, i.e. $\omega_s = \omega_p + \omega_i$. The newly created photon of higher frequency is subsequently detected with higher efficiency than the original photon using conventional SPDs, such as SPADs or PMTs.

2.2.5.2 SPECTRAL RANGE AND EFFICIENCY

While the general principle sounds fairly simple, the implementation suffers from technical difficulties thus limiting the conversion efficiency. Providing sufficient optical pump energy at the right time is generally hard to achieve: continuous-wave illumination [90] of the crystal provides time-independent conversion, but causes stability issues due to heating and background

fluorescence; conversely, gated operation [91] mitigates stability problems at the cost of overall reduced conversion efficiency. Various approaches to improve the conversion efficiency externally include the utilization of a resonant cavity which yields efficiencies up to 90% [90] or the use of an optical waveguide [92] to concentrate the pump power to a smaller interaction volume. Overall detection efficiencies are limited by the choice of SPD and can reach up to 50% at 1550 nm. Dark counts from residual fluorescence are a common problem, introducing dark count rates up to 800 kHz [93].

2.2.5.3 TIMING CHARACTERISTICS

As the parametric conversion is an ultra-fast electronic process, no additional timing uncertainty or delay is incurred. The timing accuracy and decay time are thus limited by the SPD of choice.

2.2.6 VISIBLE LIGHT PHOTON COUNTER (VLPC)

2.2.6.1 PRINCIPLE OF OPERATION

The VLPC is a semiconductor hetero-structure-based SPD [49], [94]–[96]. Three layers of different materials are sandwiched between two electrodes. The cathode is located at the detector input facet and, as such, is made from an optically transparent material. It follows an intrinsic silicon region, a moderately As-doped gain region, and the anode is made from heavily As-doped silicon (see Figure 2.2-3). The absorption of a visible photon in either the intrinsic silicon region or the gain region creates an electron-hole pair. The electron and hole are separated and accelerated toward the electrodes by an applied voltage. The As-impurities inside the gain region form a donor band which lies only 54 meV below the conduction band. If a photo-generated hole now traverses the gain region, it carries sufficient kinetic energy to impact-ionize one of the As-impurities thus creating additional free charge. The acceleration of the second charge creates additional carriers which effectively results in avalanche multiplication throughout the gain region. The electron avalanche can be readily read out using conventional electronics.

The benefit of the As-doped gain region is hole-trapping. Contrary to SPADs where electrons and holes are created by the avalanche multiplication, in VLPCs only free electrons are created through impact ionization while the holes remain trapped inside the As-impurities and propagate only very slowly via conduction hopping [48], [94]. As a consequence, the multiplication process in VLPCs is almost noise-free and differences in avalanche magnitude resulting from varying numbers of absorbed photons can be readily discriminated. The VLPC thus exhibits excellent photon-number-resolving capabilities.

One major drawback of the VLPC counter is the very shallow donor band in the gain region. Operation temperatures of 6-7 K are prerequisite in order to avoid thermal donor excitation into the conduction band.

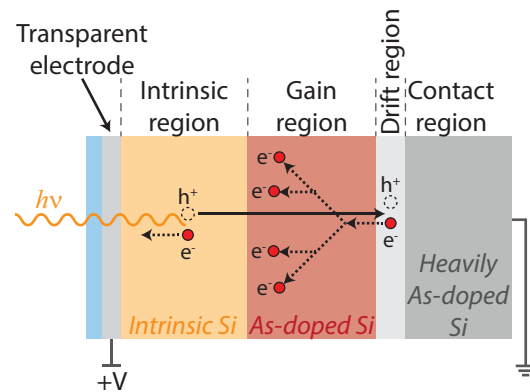


Figure 2.2-3: VLPC design illustrating the different heterostructure regions and functions

2.2.6.2 SPECTRAL RANGE AND EFFICIENCY

The VLPC operation is mostly limited to the visible range where detection efficiencies up to 88% have been realized [95]. In the IR the VLPC is plagued by extremely high dark count rates which are due to the shallow donor band in the gain region that is extremely sensitive to photo-excitation through black-body background radiation. The bi-layer structure (intrinsic Si / As-doped Si) is chosen specifically to suppress infrared absorption as such photons are absorbed only in the As-doped gain region [94]. At the same time, this reduces the infrared detection efficiencies to only a few percent. The residual dark count level is on the order of 20 kHz [48].

2.2.6.3 TIMING CHARACTERISTICS

The detector dead time is limited by the carrier extraction time and is approximately 100 ns. The lowest timing jitter reported was around 250 ps [48].

2.2.7 OVERVIEW AND COMPARISON

Detector	Detection efficiency	Dark Count Rate	Timing Jitter	Max. Count Rate	Number Resolution	Reference
PMT (vis)	40% @500 nm	100 Hz	300 ps	10 MHz	Yes	[97]
PMT (IR)	2% @1550 nm	200 kHz	300 ps	10 MHz	Yes	[97]
SPAD (vis, thick junction)	65% @650 nm	25 Hz	400 ps	10 MHz	No	[71]
SPAD (vis, thin junction)	49% @550 nm	25 Hz	35 ps	10 MHz	No	[49]
SPAD (IR, gated)	10% @1550 nm	91 Hz	370 ps	10 kHz	No	[98]
SPAD (IR, self-differencing)	10% @1550 nm	16 kHz	55 ps	100 MHz	No	[99]
TES	50% @1550 nm	3 Hz	100 ns	100 kHz	Yes	[80]
TES	95% @1556 nm	-	-	100 kHz	Yes	[79]
QD Tunnel Diode	12% @550 nm	2 mHz	150 ns	250 kHz	Yes	[87]
QD FET	68% @805 nm	-	-	1 Hz	Yes	[85]
Up-Conversion	50% @1550 nm	460 kHz	-	5 MHz	No	[90], [91]
VLPC	88% @694 nm	20 kHz	40 ns	10 MHz	Yes	[95]
VLPC	40% @ 633 nm	25 kHz	240 ps	10 MHz	Yes	[100]

The detector technologies presented above all excel in specific areas, yet fail in others. The choice of detector is therefore mostly determined by the application. The table above shows a summary of the important SPD parameters. In the visible regime, there exist several detector which offer good detection characteristics in all performance categories. In the IR the trade-offs between the individual aspects of the detection performance become more pronounced. Only the TES or up-conversion-based detectors reach levels above 50%, but at the cost of large timing jitter or dark counts, respectively. The TES is a particularly interesting detector because it offers outstanding characteristics in all categories, but fails badly in timing accuracy. Dark count levels vary significantly with the TES and the SPAD reaching low Hertz levels and the QD-based tunnel diode even a few milli-Hertz. Ultimately, every detector involves some degree of trade-off between two or more parameters. Moreover, all of above detectors are operated as bulky, external, stand-alone units, which significantly limits their scalability.

The remaining part of this chapter is dedicated to the review of the superconducting nanowire single-photon detector (SNSPD). This detector offers reasonably high detection efficiency over a broad spectral range from the visible into the NIR paired with outstanding timing characteristics. The

combination of high-level performance in all categories has made the SNSPD much sought after, especially for demanding applications in the NIR. Furthermore, photonic integration of the SNSPD has been achieved which makes this SPD uniquely capable of solving the scalability issue which SPDs currently face. The remaining part of this chapter is therefore devoted to the SNSPD, its principle of operation and design parameters. Its integration will be addressed in the following chapter.

2.3 SUPERCONDUCTING NANOWIRE SINGLE-PHOTON DETECTOR

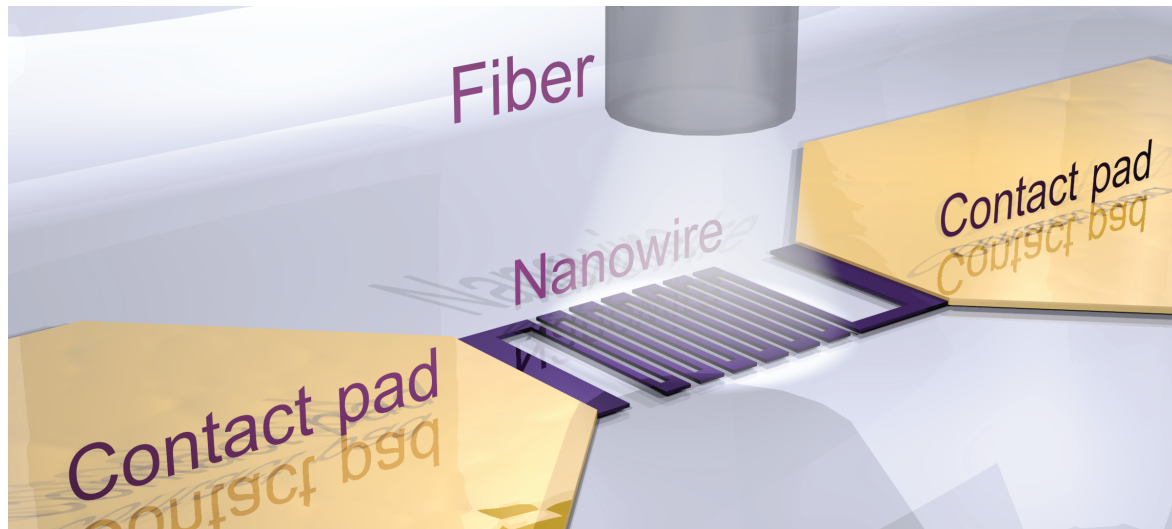


Figure 2.2-1: SNSPD layout for normal incidence detection. The meandering nanowire is connected to contact pads and an optical fiber mounted above the nanowire.

The SNSPD belongs to the group of emerging SPD technologies and forms the backbone of the waveguide-integrated detectors fabricated for this thesis. In comparison to the detectors introduced above, SNSPDs are sensitive over a significantly wider spectral range from the UV to the IR at moderate to high efficiency levels and extremely low dark count rates. They offer outstanding timing characteristics with recovery times of a few nanoseconds and timing jitter levels below 100 ps and do not suffer from afterpulsing effects.

The aim of this section is to gain an understanding of this detector which allows for the design of integrated SNSPDs. The general principles of SNSPD operation and the associated fundamental physical concepts will therefore be reviewed. This includes a macroscopic electrodynamic model in which the detector element is regarded as a simple switching element and a more detailed microscopic model which investigates the fundamental physics of the detection process. The degree of depth in this review is determined by the desire to build and characterize integrated detectors.

2.3.1 GENERAL PRINCIPLE OF OPERATION

Although the basic concept of using a thin superconducting film for particle detection was already suggested by Sherman in 1962 [101] its application in photo-detection and, in particular, in single-photon detection were mostly pioneered by Gregory N. Gol'tsman et al. in the 1990s and early 2000s [47], [102]. The fundamental concept, as the name implies, is based on a superconducting nanowire which is switched from its superconducting state to normal conductivity upon the absorption of one single photon. Figure 2.2-1 shows a schematic of the detector consisting of a long meandering nanowire with electrodes on either end and an optical fiber mounted above the nanowire for photon insertion under normal incidence.

As long as the wire is in its superconducting state, an externally applied bias current flows unimpeded at zero ohmic resistance. Given a suitable geometry and biasing conditions, the absorption of a single photon has the potential to locally destroy superconductivity throughout the nanowire cross-section. As a consequence, the wire's ohmic resistance increases from zero when superconducting to several hundred ohm when normal-conducting. This causes a significant voltage drop across the wire which can be measured using fast electronic read-out equipment. Subsequently, superconductivity is restored and the supercurrent returns into the wire within a few nanoseconds. At this point the nanowire is ready to detect the next photon.

Different geometrical nanowire layouts exist, including wide, narrow and bowtie-shaped bridges which consist only of a short section of superconducting material between two electrodes, or superconducting nanowire avalanche photodetectors (SNAPs) which are composed of multiple nanowires connected in parallel. Figure 2.3-2 shows the most frequently used implementation of a long meandering nanowire. Typical nanowires are around 100 nm wide and 4-6 nm thick. The specific detector operation varies slightly among the different layouts, but the detection mechanism remains the same.

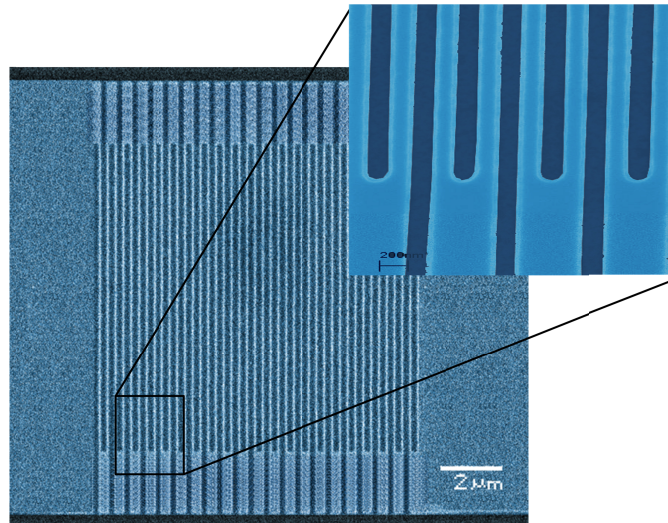


Figure 2.3-2: Scanning electron micrograph of a NbN nanowire. Provided courtesy of V. Kovalyuk at Scontel

Generally, the SNSPD concept is similar to the TES which was introduced in section 2.2.3. In contrast to the TES, SNSPDs are not operated in a bolometric regime close to the transition temperature. SNSPDs are predicated on the complete superconductivity breakdown upon photon absorption instead of a transition into a meta-stable region. As a consequence, the increase in resistance in SNSPDs is independent of the number of photons resulting in the SNSPDs' inability to discriminate photon numbers.

Usually, the superconducting nanowire is niobium-based with niobium nitride (NbN) and niobium titanium nitride (NbTiN) being the most frequent material choices. However, SNSPDs made from tungsten silicide (WSi) [103], magnesium di-boride (MgB_2) [104], and tantalum nitride (TaN) [105] have also been demonstrated. The SNSPDs fabricated for this thesis are all based on NbN. All of the descriptions and explanations throughout this thesis are therefore intended for, but not necessarily limited to NbN as detector element.

2.3.2 MACROSCOPIC SNSPD DETECTION MECHANISM

The key ingredient in SNSPDs is superconductivity. It manifests macroscopically as a switching mechanism by which the wire's ohmic resistance changes drastically upon the absorption of a photon. Microscopically, the switching mechanism is attributed to magnetic vortices which cross the nanowire and thereby locally destroy superconductivity. For a better understanding it is helpful to

discuss these two views separately. We will begin with the macroscopic view which crudely considers the wire as an electrical switch. This will provide new insights regarding the wire geometry and serves as a necessary basis for the microscopic picture which will be explained subsequently.

2.3.2.1 SUPERCONDUCTING-RESISTIVE SWITCHING

In its steady state, the nanowire is superconducting and finite bias current flows through it. Upon absorption of a photon the wire is temporarily switched to resistive, normal conductivity. The recovery of superconductivity is established by cooling, i.e. heat dissipation into the environment. The switching capability is commonly exploited to route current either mostly through the wire itself when it is superconducting or mostly through a parallel $R_L = 50 \Omega$ circuit when it is resistive (see Figure 2.3-3). Although current is never completely blocked from either arm, the large differences in resistance between the two states ensure small enough residual current which can be eliminated entirely by additional electronics as will be shown below. The nanowire’s inductive load L_K has particular consequences in the switching dynamics which will be elucidated further below.

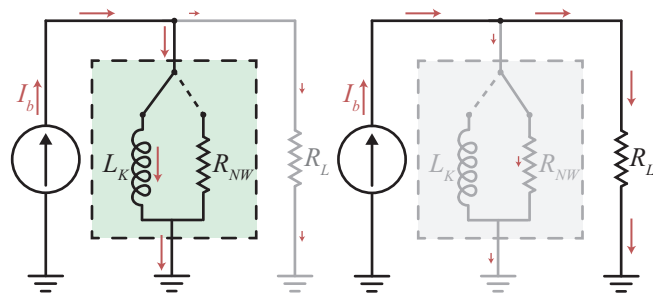


Figure 2.3-3: Conceptual illustration of superconducting nanowire (green box) switching mechanism. Left: the current (red arrows) is flowing through the resistance-free nanowire in its superconducting state. Right: the large resistance of the normal-conducting wire drives the current into the 50Ω shunt. The inductor L_K denotes the nanowire’s kinetic inductance.

2.3.2.2 GENERAL ELECTRONIC LAYOUT

The general electronic layout for SNSPD operation is shown in Figure 2.3-4. A bias current I_b of several micro-Ampères is supplied to the nanowire by a constant current source through a bias-tee which separates RF and DC components. The current entry into the nanowire through the bias-tee’s DC port inductor acts as a low-pass filter and reduces undesired current fluctuations. In the superconducting state, the current will flow directly through the highly conductive nanowire and the bias-tee’s capacitor prevents any current from leaking into the read-out electronics. Upon destruction of superconductivity, the nanowire’s transient increase in resistance causes charge to temporarily accumulate on the bias-tee’s capacitor, which results in a short-lived voltage pulse in the RF exit line. The magnitude of the voltage pulse is determined by the applied bias current I_b and the line’s resistive load which is usually $R_L = 50 \Omega$. In order to obtain large and easily distinguishable voltage pulses V_s high bias currents I_b are desirable. Generally, several micro-Ampères bias current produce voltage pulses of several hundred microvolts. Adequate amplification is thus needed. The signal pulse magnitude is thus given by

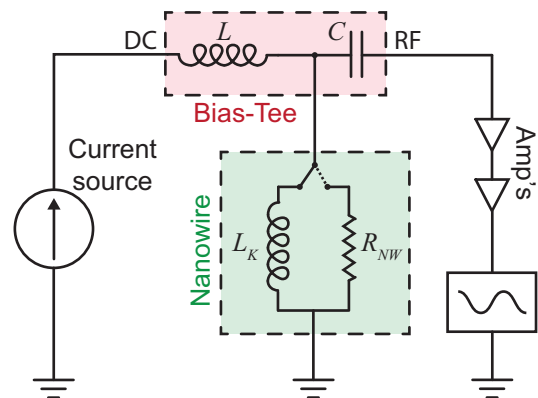


Figure 2.3-4: Basic SNSPD electronic circuit schematics with the nanowire being depicted as resistive switching element with inductive load

$$V_s = R_L I_b G \quad \mathbf{2.3.2-1}$$

where G denotes the gain factor of the employed amplifiers. The amplified signal is sent to advanced electronic equipment for further processing and analysis. Upon return to superconductivity the current through the nanowire will start to build up again until the initial state has been reached.

2.3.2.3 SWITCHING DYNAMICS AND KINETIC INDUCTANCE

The recovery of superconductivity after its destruction happens on a short timescale (<1 ns) due to rapid heat dissipation into the environment [106], [107]. In contrast, the supercurrent recovery is more time-consuming. This is mainly due to the nanowire's *kinetic inductance* L_K which leads to a recovery time of $\tau_R = L_K/R_L$ where $R_L = 50\Omega$ is the RF load line's impedance.

Kinetic inductance is best described in analogy to magnetic inductance: the energy of a magnetic field induced by a current I is proportional to the magnetic inductance L_M of the circuit, i.e. $E_M = 1/2 L_M I^2$. Equivalent to this phenomenon, one can describe the kinetic energy required to generate the supercurrent I_s as

$$E_K = \int_{\mathbb{R}^3} n_s \frac{mv^2}{2} dV = \frac{1}{2} L_K I_s^2 \quad \mathbf{2.3.2-2}$$

where n_s is the superconducting charge carrier density, v denotes the charge carrier velocity, and L_K is the kinetic inductance. By recalling the definition of the supercurrent density $j_s = n_s q_s v$, where $q_s = 2e$ is the superconducting charge, we can define the kinetic inductance as

$$L_K = \frac{m_s}{2n_s e^2} \int_{\mathbb{R}^3} \frac{j_s^2}{I_s^2} dV \quad \mathbf{2.3.2-3}$$

For sufficiently small nanowires, we can assume a spatially uniform current density such that for a nanowire of cross-sectional area A , length l , and width w such that $V = lA$ and $I_s = j_s A$ above equation yields

$$L_K = \frac{m_s}{2n_s e^2} \frac{l}{A} \quad \mathbf{2.3.2-4}$$

As can be seen from above equation, the kinetic inductance is proportional to the length of the nanowire l and inversely proportional to its cross-section A . In the case of long nanowires with small cross-sectional area which are commonly employed in SNSPDs, kinetic inductance reaches relatively large values. The kinetic inductance is thus the predominant current-recovery-limiting factor in SNSPDs causing recovery times of several nanoseconds [106], [107]. It is therefore important to realize that the wire geometry has a direct influence on the SNSPD's recovery time: increases in wire cross-section and reductions in wire length decrease the recovery time.

2.3.3 MICROSCOPIC SNSPD DETECTION MECHANISM

The basic principle of SNSPD operation and the involved electrodynamics are adequately explained by regarding the superconducting nanowire as a fast switching element. We saw that the wire geometry directly impacts the detector's recovery time through the kinetic inductance. Yet, the

macroscopic picture offered no insight into the other performance parameters including the detection efficiency, spectral range, dark counts, and timing jitter. In the following, therefore, the perspective will be changed and the SNSPD analyzed on a microscopic scale.

2.3.3.1 DETECTION EFFICIENCY

In section 2.1.1, the concept of detection efficiency η_{de} as the product of internal and external contributions, η_{int} and η_{ext} , respectively was introduced. In SNSPDs these parameters are commonly referred to as *absorption efficiency (AE)* η_{ae} which quantifies the probability of absorption given a photon arrives at the detector, and *internal quantum efficiency (IQE)* η_{iqe} which represents the probability that the absorption of a photon leads to a detection event. The detection efficiency of a SNSPD is thus given by

$$\eta_{de} = \eta_{ae} \times \eta_{iqe} \quad \mathbf{2.3.3-1}$$

The possibility to lose photons on the way from a distant source to the detector element is accounted for by the coupling efficiency η_c . The complete SNSPD system efficiency is thus given by $\eta_{se} = \eta_c \eta_{ae} \eta_{iqe}$. The coupling efficiency η_c is, however, a macroscopic engineering parameter which is affected by fiber connections, fiber placement, etc. and will thus not be discussed here.

ABSORPTION EFFICIENCY

The absorption efficiency (AE) η_{ae} – the probability of an incident photon being absorbed by the superconducting nanowire – is, generally, given by Beer’s law and thus depends on the material specific absorption coefficient and the absorption length. In normal incidence SNSPDs, the absorption length is determined by the wire’s thickness. With only a few nanometers, the thickness poses a major limitation in SNSPDs of this configuration. Optical cavities have therefore been employed to artificially extend the distance over which the photon is absorbed [108]–[111]. This will be addressed in more detail below. The absorption coefficient itself is to the largest extent determined by the superconducting material of choice. A small degree of adjustment is offered by the extent of the nanowire-covered area. For a large filling fraction, i.e. larger wire widths and smaller gaps, the absorption coefficient is larger than for small filling fractions, yet the wire geometry also affects the IQE as will be explained below. In general, the AE is a purely geometry and material-dependent parameter and thus constitutes a *linear scaling factor* for the detection efficiency $\eta_{de} = \eta_{ae} \times \eta_{iqe}$.

INTERNAL QUANTUM EFFICIENCY

The probability that the absorption of a photon leads to a detection event is referred to as internal quantum efficiency (IQE) η_{iqe} . In the case of SNSPDs, it is given by the likelihood that the photon absorption initiates a mechanism which eventually leads to the formation of a normal-conducting domain across the entire nanowire cross-section. The involved mechanism shows clear dependencies on the energy of the absorbed photon, the applied bias current, and the nanowire cross-section. The microscopic details of the mechanism are the focus of considerable research efforts, but a universal model capable of a complete description of the SNSPD’s detection mechanism is yet to be devised [112]. The currently most accurate and widely applicable models [113]–[117] are based on the formation of magnetic vortices which cross the nanowire and thereby

form a normal-conducting domain. We will review the basic aspects of those models in order to gain a fundamental understanding of the parameters which influence the performance of SNSPDs.

2.3.3.2 COUNT RATE AND DARK COUNT RATE DEPENDENCE ON BIAS CURRENT

In the previous paragraph it was mentioned that the energy of the absorbed photon, the applied bias current, and the nanowire cross-section inherently influence the detection mechanism. For a better understanding it is helpful to provide a realistic and practical context for these parameters before they are elaborated on a microscopic level.

The design of SNSPDs is usually intended for a specific optical wavelength or wavelength range. The photon energy is therefore a parameter with limited or no tunability during SNSPD operation. The wire-cross-section can be adjusted during the design phase and therefore provides a means to tailor the detector to specific needs. The bias current I_b represents the only³ tunable parameter during SNSPD operation and allows for the flexible adjustment of certain detection characteristics. In an idealized measurement in which the photon energy is fixed and a constant flux of photons Φ is incident on the detector, a characteristic dependence of the measured count rate R_c on the applied bias current I_b is found (green curve in left graph of Figure 2.3-5): for low bias current values the detector does not register any counts; from a certain bias current value onward – the *threshold current* I_{th} – the count rate R_c is highly current-dependent and grows monotonously until it saturates at some larger current value, called *saturation current* I_{sat} [114].

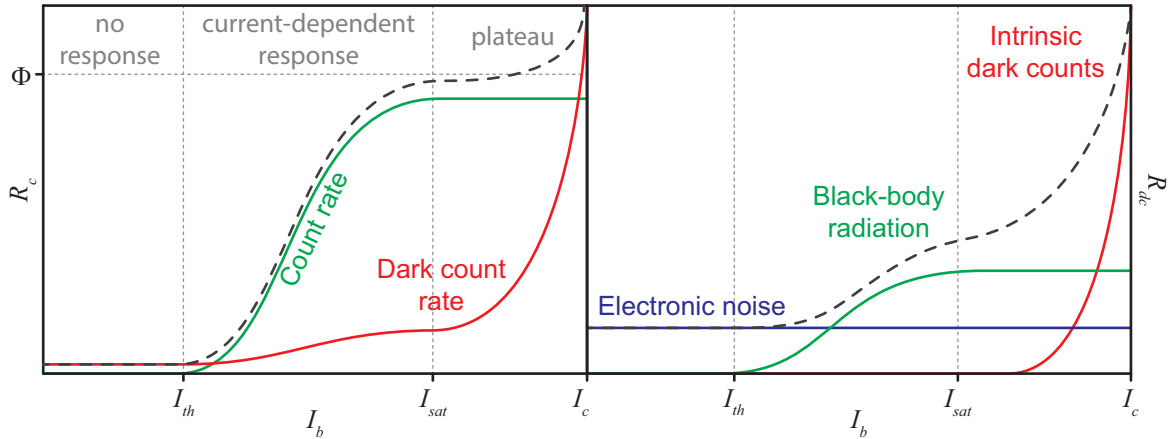


Figure 2.3-5: Left: idealized count rate (green) and dark count rate (red) curves as a function of bias current for fixed nanowire geometry; the dashed line represents the combined measured count rate curve. Right: dark count rate contributions as a function of bias current; the dashed line represents the combined dark count rate curve.

The portrayed count rate behavior generally reflects the dependence of the detection efficiency $\eta_{de}(I_b) = R_c(I_b)/\Phi$ on the bias current I_b . Since the absorption efficiency η_{ae} is independent of the bias current, it follows from eqn. 2.3.3-1 that the curve shape is determined by the internal quantum efficiency (IQE) η_{iqe} which saturates above I_{sat} . SNSPD operation in the plateau is therefore desirable.

Operation close to the critical current I_c is, however, plagued by a growing dark count contribution (red curve in left graph of Figure 2.3-5). The dark count rate, i.e. the count rate with no light incident

³ In principle, the operation temperature and external magnetic fields provide additional means for adjustment. This was, however, not studied as part of this thesis and is therefore disregarded here.

on the detector, in SNSPDs is generally very low compared to other SPDs. It is composed of multiple contributions which show individually different dependencies on the bias current (see right graph in Figure 2.3-5): the electronic noise (blue line) generally forms a weakly current-dependent to current-independent noise floor; counts from black-body radiation (green line) depend on the detection efficiency η_{de} and thus follow the same trend as the count rate; and the intrinsic dark counts (red line) exhibit a usually exponential dependence on bias current. The latter contribution is similar in nature to the detection mechanism and also the subject of current research. Multiple models exist [118]–[125] which describe the dark counts with varying accuracy. The details will be described together with the microscopic models on the detection mechanism.

It is important to note, that the positions of the threshold current I_{th} , saturation current I_{sat} , and critical current I_c depend on the wire geometry including the cross-sectional area and the wire shape [105], [126]–[128]. They can be at independently different positions, the depiction in Figure 2.3-5 is only a general example. In unfavorable cases the critical current can even be smaller than the saturation current, i.e. $I_c < I_{sat}$, in which case no plateau exists. The wire geometry therefore provides possibilities to adjust and optimize the characteristic current values. Considering the influence of the dark counts it is desirable to operate the SNSPD at a bias current which minimizes the dark count contribution and maximizes the IQE. The latter is achieved by operation on the plateau, the former by operating far away from the critical current I_c . The optimal SNSPD would thus provide a large plateau regime, i.e. a saturation current I_{sat} which is far below the critical current I_c . Therefore, geometrical configurations which maximize the plateau are desirable.

In the following a more in-depth review of the SNSPD's microscopic behavior will be conducted in order to extract information about the geometrical factors which affect the plateau. The review includes the basics and a few select topics of superconductivity with particular focus on vortex formation and to a certain degree the microscopic models which describe the SNSPD detection mechanism.

2.3.3.3 SUPERCONDUCTIVITY BASICS

The following theoretical aspects of superconductivity are introduced on a very general basis. Its association with SNSPDs will be made where possible, but the explicit description of the nanowire dynamics requires the full background of the involved phenomena and therefore follows after this introduction.

In general, superconductivity is characterized as a thermodynamic state in which electrical resistance vanishes and magnetic fields are expelled from the superconductor's interior [129]–[133]. Three theories have prevailed for the description of these phenomena. The theory devised by Bardeen, Cooper, and Schrieffer (BCS) [134], [135] aims at describing the microscopic origins of superconductivity in general. It is capable of describing superconductivity on a fundamental level. It will be used in the following to explain the disappearance of the wire's ohmic resistance and the excited state which arises immediately after the photon absorption. The theory is very successful in describing low-temperature superconductors and earned the authors the Nobel Prize in physics in 1972. The older purely phenomenological theories by the London brothers, and Ginzburg and Landau produce accurate results in specific areas and benefit from reduced complexity. They are used for the most part of the microscopic models which describe the detection mechanism and the occurrence of dark counts. The relevant aspects will be introduced below.

COOPER PAIRS

The core element of superconductivity is the *condensation* of electrons to a thermodynamically stable state of lower energy. According to BCS theory, such a condensation arises through the interaction of pairs of electrons to form bound two-electron states called Cooper pairs (CPs). In this section we will briefly review the interaction which yields the binding energy $\Delta E < 0$ of a single CP. In the next section we will expand this discussion to the entire electron sea.

Cooper was able to show that despite the usual Coulomb repulsion the Fermi sea is unstable against the formation of at least one bound electron pair given a finite attractive interaction – regardless of how weak⁴ – exists between them [136]. The detailed description of the attractive interaction potential $V_{kk'}$ and its origin are well documented in standard literature [129]–[133], [137], [138], here we will restrict ourselves to the salient results: a CP's binding energy arises from a short-lived phonon exchange given the energy difference between the pair-composing electrons is smaller than the Debye energy $\hbar\omega_D$. The interaction potential $V_{kk'}$ is maximized for electrons of anti-parallel momenta and anti-parallel spins. Given these properties, it can be assumed that the interaction potential $V_{kk'}$ is completely isotropic, i.e. $V_{kk'} = -V_0$. The binding energy of a CP is then found to be $\Delta E \approx -2\hbar\omega_D \exp[-1/N(E_F)V_0]$ where term $N(E_F)$ denotes the joint density of states at the Fermi level. This result indicates that a CP's binding energy is smaller than zero given a finite interaction potential. In other words, CPs will always form as long as $V_0 > 0$.

BCS GROUND STATE AND EXCITED STATES

We will now expand the previous concept of CP formation from a single pair to the collective. If the Fermi sea is unstable against the formation of CPs given a net attractive interaction, then it follows that electrons will continue to form CPs until the binding energy for one additional CP has reduced to zero. The difficulty in handling such a scenario quantitatively is the enormous number of particles to be described. Bardeen, Cooper, and Schrieffer resolved this predicament by employing *mean-field theory* in which the occupation probability of a state \mathbf{k} is only dependent upon the *mean occupation probability* of all other states⁵. Thereby, they were able to formulate a ground state wavefunction, usually referred to as BCS ground state, whose energy eigenvalue at $T = 0$ yields an energy reduction similar to that of CP formation [129]:

$$E_{\text{cond}}(T = 0) = -\frac{1}{2}N(E_F)\Delta^2(0) \quad \mathbf{2.3.3-2}$$

where $\Delta(T)$ represents the average pairing potential per CP and $N(E_F)$ is the joint density of states at the Fermi level. The quantity is commonly referred to as *condensation energy* E_{cond} of the electron collective. It constitutes the system's energy reduction by making a transition into the superconducting state and, in turn, represents the amount of energy necessary to destroy

⁴ Conduction electrons around the Fermi edge usually possess energies of a few eV which corresponds to $>10^4$ K. Superconductivity is found at a few Kelvins which suggests an interaction energy of a few meV. Because of this enormous energy difference, it is rather surprising that even the weakest attraction can lead to CP formation [138].

⁵ In this approach, only the mean particle number \bar{N} is fixed and the actual number N is uncertain. Effectively, this describes a grand canonical ensemble where the huge number of particles ensures that the error incurred by fixing \bar{N} and leaving N variable is small.

superconductivity. A more intuitive interpretation of the condensation energy goes as follows: the CP pairing potential Δ represents the average condensation energy per CP; the superconducting condensate contains a specific number of CPs which can be approximated by $1/2 N(E_F)\Delta$; subsequently, the total condensation energy is given by the product of the two terms which equals eqn. 2.3.3-2. A quantity which is often used instead of the condensation energy is the *thermodynamic critical field* which is defined by

$$\frac{B_{cth}^2}{2\mu_0} = \frac{1}{2}N(E_F)\Delta^2(0)V \quad 2.3.3-3$$

where V denotes the volume. The thermodynamic critical field is originally derived from Ginzburg-Landau Theory and will be used later in the microscopic description of the SNSPD.

Having identified the unexcited BCS ground state, we will now review what happens when we externally excite this state as would occur, for instance, by the absorption of a photon. Bogoliubov [139] and Valatin [140], independently from one another, devised a convenient model to describe BCS excited states. They introduced a *quasi-particle (QP)* which is associated with the quantized BCS excitation. The creation of a single QP corresponds to the breaking or annihilation of one CP. The QPs – sometimes also referred to as *Bogoliubons* – have a distinct energy spectrum which is given by [129]

$$E_{\mathbf{k}} = (\xi_{\mathbf{k}}^2 + |\Delta_{\mathbf{k}}|^2)^{1/2} \quad 2.3.3-4$$

where $\xi_{\mathbf{k}} = \epsilon_{\mathbf{k}} - \mu$ is the single particle energy relative to the chemical potential (Fermi energy at $T = 0$). Figure 2.3-6 depicts the QP excitation spectrum (solid lines) and the usual dispersion relation $E_{\mathbf{k}} = \xi_{\mathbf{k}}$ for free electrons and holes (dashed lines). The graph displays the *energy gap* of size $\Delta_{\mathbf{k}}$ in the excitation spectrum. In order to create a QP, an excitation energy of $\hbar\omega \geq 2\Delta_{\mathbf{k}}$ is thus necessary⁶. The superconducting energy gap $2\Delta_{\mathbf{k}}$ can be loosely interpreted as the superconductor's equivalent to the semiconductor bandgap energy E_g below which no valence electrons can be excited into the conduction band. In the SNSPD detection process, QP excitations are partially responsible in the switching of the nanowire into its resistive state.

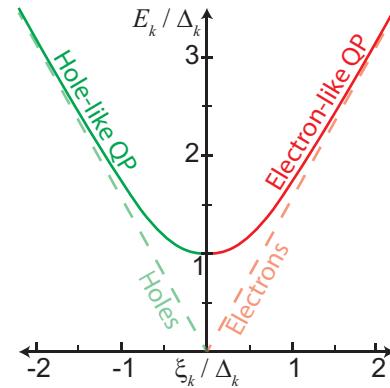


Figure 2.3-6: Quasiparticle excitation spectrum (solid lines) and pure electron and hole excitations (dashed lines)

DISSIPATION-LESS CURRENT

For a complete picture of the SNSPD's principle of operation, it is reasonable to briefly address the origin of the disappearance of the nanowire's resistance. In normal-conducting materials, a transport current is commonly described by the conduction electrons moving *on average* in one particular direction [131], [141]. The free electron gas thus possesses non-zero average momentum $\langle \mathbf{k} \rangle$ in the direction of motion. In \mathbf{k} -space this is commonly visualized by the Fermi sphere being

⁶ The factor two accounts for the fact that two electrons must be excited; an excitation of only $\Delta_{\mathbf{k}}$ would result in the non-physical creation of single-electron CP.

displaced off-center by $\langle \mathbf{k} \rangle$ (see Figure 2.3-7). Opposing this movement, or constant displacement in \mathbf{k} -space, are electron scattering processes which include phonon, lattice defect, impurity, and surface scattering. In the normal-conducting state, scattering causes individual electrons to relax to states of lower energy under the observation of Pauli's exclusion principle (see Figure 2.3-7a) [141]. Due to the abundant availability of final states after the scattering process, the Fermi sphere's displacement tends to reduce rapidly and the current decays to zero. As a consequence, an external, current-driving source is needed in order to sustain an electrical current inside a normal conductor [141].

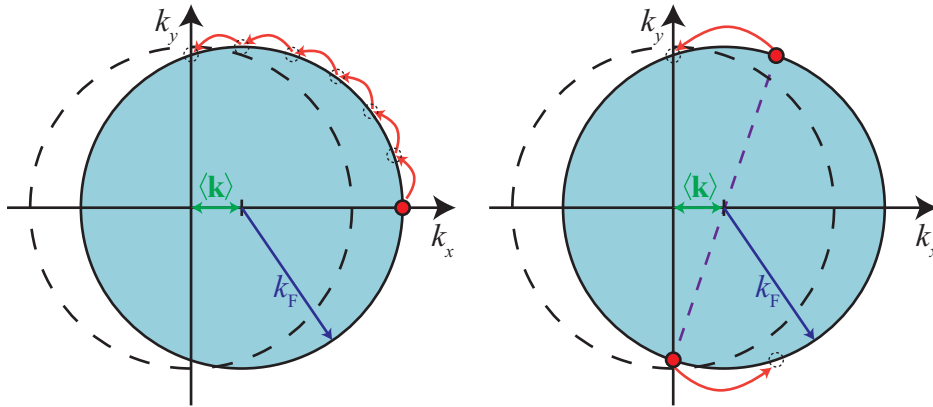


Figure 2.3-7: Comparison of electron transport in a normal-conducting (left) and a superconducting material (right). The solid circle represents a two-dimensional projection of the displaced Fermi sphere. For comparison, the empty dashed circle is the Fermi sphere's location for vanishing electron current. Left: the free conduction electron relaxes to its energy minimum through repeated scattering processes along the “softened” area around the Fermi surface. Right: scattering of a CP causes one electron to lose momentum while the anti-parallel momentum requirement results in an increase of the other electron's momentum. CP scattering, therefore, occurs only around the Fermi sphere surface without reducing the overall average momentum $\langle \mathbf{k} \rangle$.

In the case of a superconductor, the situation changes due to the paired electrons' antiparallel momenta and subsequent limitations in the availability of final states. In detail, the current-carrying particle in a superconductor is the CP $(\mathbf{k} \uparrow, -\mathbf{k} \downarrow)$. In the case of finite transport current the condensate possesses collective momentum $\langle \mathbf{k} \rangle$ similar to the normal-conducting case. As a consequence, the CP's constituent electrons possess anti-parallel momenta with respect to the center of the Fermi sphere, i.e. $(\mathbf{k} + \langle \mathbf{k} \rangle \uparrow, -\mathbf{k} + \langle \mathbf{k} \rangle \downarrow)$ [141]. This can be visualized by their wave vectors lying on opposite sides of the displaced Fermi sphere (see Figure 2.3-7b). The aforementioned scattering thus affects both electrons, yet their final states must also be anti-parallel $(\mathbf{k}' + \langle \mathbf{k} \rangle \uparrow, -\mathbf{k}' + \langle \mathbf{k} \rangle \downarrow)$, i.e. lie on the Fermi sphere surface. Electrons in a CP are, therefore, scattered around the Fermi sphere surface while maintaining their total momentum $\langle \mathbf{k} \rangle$. This description applies equally to all current forming CPs, such that the total collective momentum $\langle \mathbf{k} \rangle$ is conserved and the Fermi sphere remains displaced despite scattering. Any electrical supercurrent, once established, will therefore flow indefinitely [138]. The magnitude of the applicable current is, however, limited by the magnetic field which is induced by the supercurrent itself. In order to explain this, we will first look at the impact and expulsion of magnetic fields.

LONDON PENETRATION DEPTH

In the following we will abandon the description of superconductivity by BCS theory and utilize an older theory which was originally devised by the London brothers in 1935 [142]. It follows a purely

electrodynamic concept and is therefore more tangible than BCS theory. The London model is predicated on a *two-fluid model* in which the charge carriers are divided into two species, namely normal-conducting and superconducting fractions, n_n and n_s , respectively. The normal-conducting charges n_n continue to obey the usual Maxwellian description. On the superconducting charges, which are essentially represented by the Cooper pairs from BCS theory, the London brothers imposed additional rules [129], [130]. The supercurrent density \mathbf{j}_s was described to exist even in the absence of electric fields which is equivalent to infinite conductivity. The expulsion of the magnetic field was found to decay exponentially inside the superconductor, i.e. $\nabla^2 \mathbf{B} = \lambda_L^{-2} \mathbf{B}$. The parameter λ_L denotes the *London penetration depth* which is given by

$$\lambda_L = \left(\frac{m}{4\mu_0 n_s e^2} \right)^{1/2} \quad \mathbf{2.3.3-5}$$

The penetration depth is material and temperature dependent and is usually on the order of several hundred angstroms [130]. It can be shown from classical electrodynamic considerations in the London model that the field decay is caused by circulating surface currents which exactly cancel the external field and thus actively expel any magnetic field from the superconductor's interior [130].

GINZBURG-LANDAU COHERENCE LENGTH

The Ginzburg-Landau (GL) theory is a thermodynamic model which accounts for the phase transition at a critical temperature T_c by a reduction in the system's free energy [129], [130], [137]. Therefore, the free energy density g is expanded in powers of an *order parameter* X , i.e. $g_s = g_0 + \alpha X + \beta X^2 + \dots$. The order parameter X is zero above the transition point and increases gradually below T_c until it saturates at a system-specific value [131], [143]. Ginzburg and Landau chose the superconducting charge carrier density $n_s = |\psi|^2$ from the London model as order parameter and terminated the series after the second term⁷ [129], which yields $g_s = g_0 + \alpha |\psi|^2 + \frac{1}{2} \beta |\psi|^4$. The approach directly yields the condensation energy and the thermodynamic critical field $\Delta g = g_s - g_0 = \alpha |\psi|^2 + \frac{1}{2} \beta |\psi|^4 = B_{ctn}^2 / 2\mu_0$. In contrast to the London theory, Ginzburg and Landau allowed the order parameter $\psi(\mathbf{r})$ to vary spatially. This allows for a treatment of local perturbations of the superconducting state, which are reflected in a local decrease in the order parameter. Ginzburg and Landau were able to show that such local perturbations recover over a characteristic length ξ_{GL} . It is commonly referred to as *coherence length* and is given by

$$\xi_{GL} = \left(\frac{\hbar^2}{2m_s |\alpha|} \right)^{1/2} \quad \mathbf{2.3.3-6}$$

The coherence length ξ_{GL} represents a central quantity in the general description of superconducting phenomena. In particular, for nanowires it represents the characteristic length below which the system's dimensionality changes. It is therefore a central parameter for superconducting systems on the nanoscale and for SNSPDs, in particular, it constitutes the motivation for the thin film approach, i.e. the reason why the nanowire's thickness is smaller than the coherence length. The details will be introduced in the subsequent section.

⁷ Due to this early series termination the GL theory produces accurate results only in the vicinity of T_c .

CRITICAL CURRENT

Although superconductors are characterized by vanishing electrical resistance, the magnitude of supercurrents is limited by the self-induced magnetic field. If the self-induced field exceeds the critical field strength H_c or H_{c2} , respectively, superconductivity is no longer sustainable. The critical fields thus set an upper limit for the supercurrent density, commonly referred to as *pair-breaking critical current density* j_c . From GL-theory it can be shown that the critical current density depends upon the penetration depth and the coherence length as $j_c \propto \lambda_L^{-2} \xi^{-1}$ [130]. In most practical contexts, the experimentally realized critical current densities lie well below the theoretical prediction. This is mainly due to material imperfections.

The critical current density clearly limits the practically achievable critical current I_c in a nanowire. For a perfectly uniform current distribution within the wire, the critical current would be directly proportional to the wire's cross-section. Non-uniformities in the current distribution, however, cause effective reductions in the attainable critical current value and therefore the maximally applicable bias current of a SNSPD. The geometrical impact will be addressed in detail further below.

MAGNETIC FIELDS AND ABRIKOSOV VORTICES

There exist two different types of superconductors which are distinguished by their response to magnetic fields. These fields can be either externally applied or self-induced by transport currents. Microscopically the difference between type-I and type-II superconductors is determined by the relative length scales over which the magnetic field ($\sim \exp(-x/\lambda_L)$) and the order parameter ($\sim \exp(-x/\xi)$) decay (solid lines in Figure 2.3-8). In a thermodynamic context, the expulsion of the magnetic field from the superconductor requires energy E_B while the development of the superconducting state (recovery of the order parameter ψ) frees energy in the amount of the condensation energy E_C (dashed lines in Figure 2.3-8). The relative magnitudes of the characteristic lengths thus determine the total energy balance and, therefore, the equilibrium state of superconductivity in relation to the magnetic field. In particular, two cases are of interest [129], [144], [145]:

- For $\lambda_L \leq \xi_{GL}/\sqrt{2}$ there exists a specific critical field strength H_c below which the energetically preferable situation is the complete expulsion of the magnetic field from the conductor, barring a thin volume of depth λ_L below the superconductor surface as described above. In case the external field exceeds H_c , the energy required to expel the field becomes too large to sustain the screening surface currents such that the field penetrates into the superconductor's interior and superconductivity is destroyed. Superconducting materials of this sort are referred to as **type-I superconductors**.
- The situation changes drastically when $\lambda_L > \xi_{GL}/\sqrt{2}$: below a certain threshold H_{c1} , the superconductor is able to maintain its field-free state as in the case of type-I superconductors (Meissner state). If the magnetic field, however, exceeds H_{c1} , the energetically preferable state is not the complete collapse of the screening current, but a spatial reconfiguration in which the superconductor becomes interspersed with normal-conducting, magnetic field-carrying regions of size ξ_{GL} , called *Abrikosov vortices* (see Figure 2.3-9) [145]. Each of these vortices is surrounded by screening ring currents which contain the magnetic flux to the inside of the vortex. A remarkable phenomenon which will not be addressed here in detail is the quantization of the magnetic flux to integer multiples of

$\Phi_0 = h/2e$. The total magnetic flux per vortex is thus quantized as $\Phi = n\Phi_0$ with $n = 1, 2, 3 \dots$. The screening currents fall off with $1/r$ from the vortex center and start to decay exponentially at $r \approx \lambda_L$. Such a configuration is energetically favorable due to the shorter distance over which ψ recovers compared to the relatively long decay length of the magnetic field. With growing field strength the vortex number gradually increases until above a second threshold $H_{c2} > H_{c1}$ superconductivity is no longer sustainable. The intermediate state is commonly referred to as *vortex state* or *Shubnikov phase* (see Figure 2.3-9). Materials which exhibit the Shubnikov phase belong to the class of **type-II superconductors**.

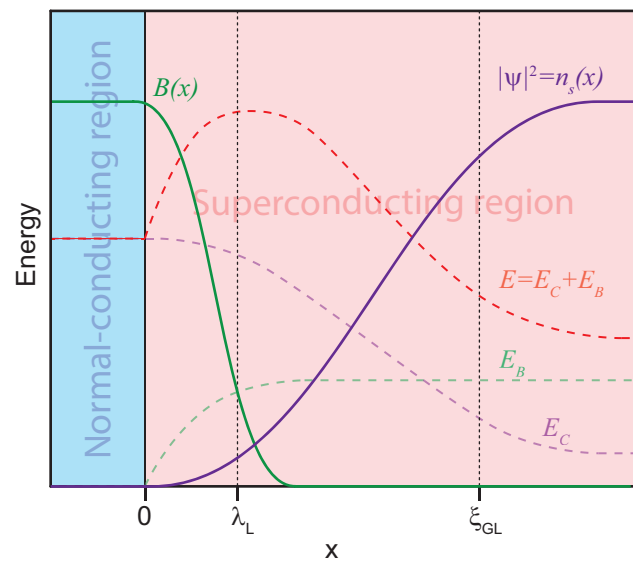


Figure 2.3-8: Interface from normal-conductor to superconductor plotted for the case of $\xi_{GL} > \lambda_L$. The magnetic field (solid green line) decay with λ_L and the superconducting charges build up with ξ_{GL} (solid purple line). The associated energies are depicted as dashed lines: magnetic expulsion energy (green), condensation energy (purple), energy balance (red).

It is important to note that in strong type-II superconductors vortices can exist even in the absence of magnetic fields [146], [147]. The superconductors which are usually employed in SNSPDs belong to this class.

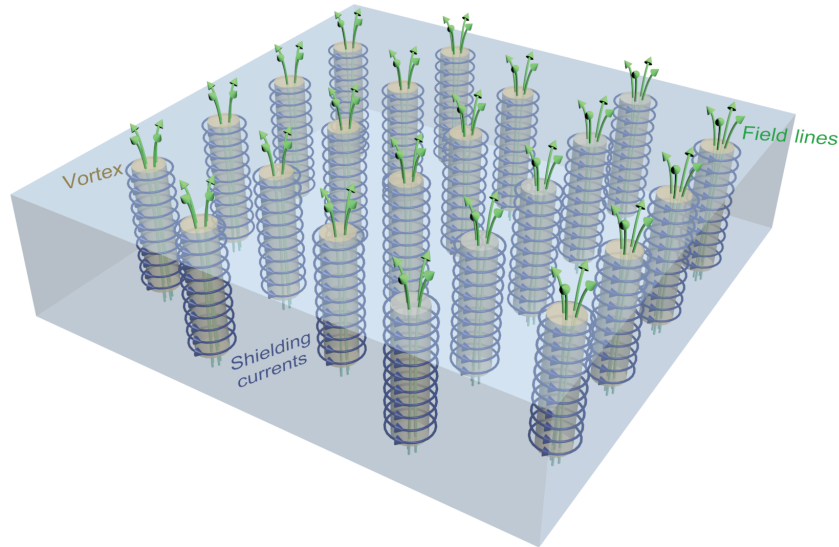


Figure 2.3-9: Illustration of a type-II superconductor in the Shubnikov phase. A regular array of vortices (yellow) permeates the superconductor. The shielding supercurrents are indicated by the blue ring arrows around the vortices and the magnetic field by the green arrows inside the vortices.

PEARL VORTICES

Magnetic fields were previously said to decay over the London penetration depth λ_L into the superconductor. In a SNSPD, the nanowire's thickness $d \approx 4$ nm is, however, significantly smaller than the penetration depth $\lambda_L \approx 350$ nm in NbN [113]. Judea Pearl was able to show that in the case of $d \ll \lambda_L$ the magnetic field penetration depth increases and is given by [148]

$$\Lambda = \frac{2\lambda_L^2}{d} \quad \mathbf{2.3.3-7}$$

The quantity Λ is commonly referred to as *Pearl length*.

As a consequence, the Abrikosov vortices which form in the Shubnikov phase of type-II superconductors change their size and conformation. The normal-conducting core size maintains its diameter ξ , yet the ring current density decays over a longer distance until $r \approx \Lambda \gg \lambda_L$. This effectively translates into a vortex diameter increase from λ_L for Abrikosov vortices in bulk superconductors to Λ for *Pearl vortices* in thin film superconductors.

VORTEX NUCLEATION IN NANOWIRES AND PHASE SLIP LINES

It is well-known that physical behavior changes when system dimensions approach characteristic length scales. This was already the case in above description of the Pearl vortex. The other characteristic length which can be larger than the dimensions of the superconductor is the coherence length ξ . A superconducting nanowire whose thickness d falls below the coherence length ξ effectively becomes a two-dimensional (2D) superconductor. This is the case for most NbN-based SNSPDs where $d \approx 4$ nm and $\xi \approx 5$ nm.

Vortex formation remains possible in 2D nanowires unless the wire is too narrow. Konstantin K. Likharev was able to show that a minimum width of $w > 4.41\xi$ is necessary to allow for the nucleation of vortices [149]. In general, vortex nucleation is induced by externally applied or self-

induced magnetic field. If the field strength exceeds the lower critical field H_{c1} , vortices begin to form as a consequence of energy minimization. Due to the reduced size of superconducting nanowires, the impact of the surface on the vortex formation has to be considered. By virtue of the method of images [150], the interaction of the vortex with the surface can be interpreted as the interaction of the vortex with a mirror image of itself. The interaction leads to an increased energy potential at the surface. In the case of $\xi \ll \lambda_L$ which is true for NbN ($\xi \approx 5$ nm and $\lambda_L \approx 350$ nm [113]), it can be shown that the critical field is increased to $H_{bl} = \frac{H_{c1}\hbar}{\sqrt{2}} > H_{c1}$ [151], [152]. The associated potential barrier increase for vortex entry at the surface is commonly referred to as *Bean-Livingston barrier* [153]. In current-carrying, narrow nanowires the barrier conditions are slightly modified [154]–[157] and its calculation is subject of current research efforts [112]–[114], [124], [158], [159].

The vortex entry barrier can be overcome by sufficiently energetic perturbations, e.g. the absorption of a photon or thermal fluctuation. Upon formation, the vortex is immediately subjected to a Lorentz force which is exerted by the bias current. As a consequence, the vortex is pushed across the entire width of nanowire leaving a trail of normal-conductivity in its wake (see Figure 2.3-10). The normal-conductivity line arises due to slow recovery of superconductivity relative to the movement of the vortex [113]. It is referred to as *phase slip line* in analogy to Little phase slips which occur in 1D nanowires (see annex A1 for details). In similar analogy, the formation of the normal-conducting domain in a 2D nanowire is referred to as *vortex-induced phase slip (VPS)* [112], [160].

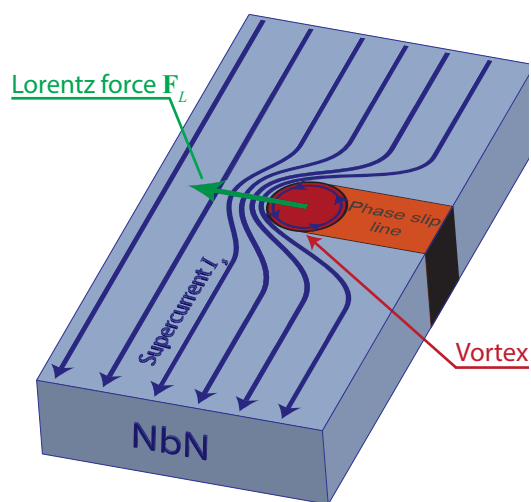


Figure 2.3-10: Phase slip line created by vortex moving across nanowire.

Beside single occurrences, vortices can also manifest in bound pairs, so-called vortex-antivortex-pairs (VAPs). VAPs are characterized by ring currents of opposite direction and a finite binding energy. They form only at temperatures below the Berezinsky-Kosterlitz-Thouless (BKT) transition⁸ [131], [161], [162], yet standard SNSPD operating conditions fulfill this requirement. VAPs, therefore, represent a second possible vortex excitation in 2D superconducting nanowires which particularly in wider nanowires become more dominant due to reduced spatial constraints [125].

In contrast to a single vortex which directly feels a Lorentz force upon formation, a VAP experiences a net zero force due to the oppositely directed ring currents. It feels, however, a finite torque which causes the VAP to align perpendicularly to the transport current [112]. This alignment lowers the VAP's binding energy and upon the supply of additional energy, e.g. by thermal fluctuations, VAPs can unbind. The resulting unbound vortices now experience a Lorentz force in opposite directions and thus move across the wire cross-section and cause a VPS.

⁸ The BKT transition is a second order phase transition found in 2D crystals below which long range orientational order sets in [131]. A full account is beyond the scope of this thesis.

SUMMARY OF SUPERCONDUCTING EFFECTS

In the foregoing section we reviewed the basic concepts of superconductivity. Several characteristic parameters were developed, various effects discussed. In the following we will relate these parameters and phenomena to the SNSPD in order to describe the detection mechanism and the occurrence of dark counts. We will begin by assessing the effect of the nanowire geometry on the critical current.

2.3.3.4 NANOWIRE STEADY STATE AND CRITICAL CURRENT

In section 2.3.3.2 it was shown that geometries which maximize the critical current are desirable. In the following we will assess which geometrical parameters affect the nanowire's critical current value.

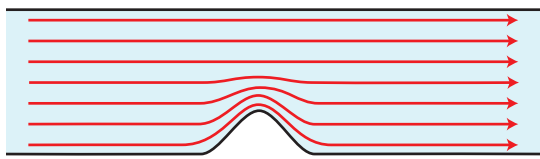


Figure 2.3-12: Illustration of current density increase at nanowire constriction

The nanowires in SNSPDs are fabricated from thin films of thickness $d \approx 4$ nm which is similar to the zero-temperature coherence length in NbN $\xi(0) \approx 4$ nm [113]. At finite temperatures $d \leq \xi$ thus applies. The nanowire width w is usually on the order of several tens above or below one hundred nanometers such that $w > \xi$. This

effectively renders the nanowire a 2D superconductor. Moreover, the London penetration depth at low temperatures $\lambda_L \approx 350$ nm such that the Pearl length $\Lambda \approx 40$ μ m [113] is significantly longer than the wire width, i.e. $\Lambda \gg w$. The superconducting current density can therefore be assumed as completely uniform throughout the wire cross-section [112], [126], [129]. A simple argument would thus lead one to believe that the critical current I_c is directly proportional to its cross-sectional area. This is, however, only true for perfectly homogeneous, straight nanowires. Geometrical inhomogeneities, i.e. variations in wire width and thickness cause undesired reductions in the critical current I_c at positions of smaller cross-sectional area (see Figure 2.3-12). Local reductions in the critical current I_c , however, affect the nanowire globally as bias currents in excess of the local critical current will always lead to the loss of superconductivity. Geometrical homogeneity is thus crucial for large critical current values.

Moreover, the otherwise uniform current density distribution across the wire cross-section incurs non-uniformities at intended bends and turns in the wire. Here, the current density increases toward the inside edge of the bend [105], [126]–[128] (see Figure 2.3-11). Ultimately, the critical current I_c of a nanowire with non-straight features is reduced relative to that of a perfectly straight superconducting nanowire.

The consequences of local reductions in the critical current are summarized in the count rate curve of Figure 2.3-13 (green solid line) in analogy to Figure 2.3-5. In case of an ideal nanowire with a perfectly uniform current distribution the SNSPD is limited by its depairing critical current $I_{c,dep}$. Constrictions and other current crowding effects reduce the

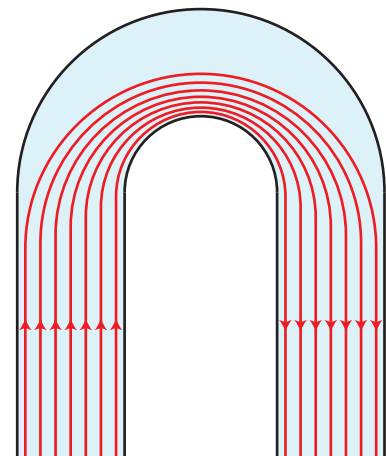


Figure 2.3-11: Illustration of the current crowding effect at nanowire bends

experimentally achievable critical current to a lower value $I_{c,exp} < I_{c,dep}$. With respect to the count rate curves introduced at the beginning of this section, the reduction in achievable critical current curtails the plateau. Therefore, in order to enable large experimentally achievable critical current values and thereby maximize the detection plateau, geometries which reduce current crowding effects are desirable. Such geometries should avoid sharp edges and small bend radii. Moreover, a flawless and consistent fabrication process which prevents the formation of constrictions along the nanowire is crucial.

2.3.3.5 INTRINSIC DARK COUNTS

The dark count contributions in an SNSPD were described in section 2.3.3.2. Dark counts originate from three sources: noise in the employed electronic circuitry, imperfect shielding from black-body radiation, and decoherence effects within the nanowire. The microscopic origin of the latter contribution is the subject of extensive research. Early investigations assumed that fluctuations in the order parameter lead to intrinsic dark counts [118]–[121]. Nowadays, the prevalent theories suggest that dark counts are caused by vortex-induced phase slips [113], [122]–[124]. Thermal activation is assumed to be the most probable cause for single vortex and vortex-antivortex pair excitations, although vortex tunneling has also been suggested [163], [164]. Most models assume an exponential dependence of the vortex generation rate Γ on the vortex entry barrier ΔE in the form of $\Gamma \propto \exp(-\Delta E/k_B T)$ which is derived from the 1D LAMH model [165], [166]. The exact description of the entry barrier ΔE , however, varies significantly from model to model as does the dependence of the dark count rate R_{dc} on the generation rate Γ . Some models are successful in describing specific scenarios, but a universal model which describes the complete dark count curve on the bias current or on the wire geometry is yet to be devised.

Experimental measurements of dark count rates indicate an exponential dependence on the normalized critical current, i.e. the ratio of bias current and experimental critical current. The dependence on the experimental critical current can be explained by the lowering of the vortex entry barrier and the nucleation of vortices at points of locally reduced critical current (bends, constrictions, etc.) [126]. The experimentally obtained trend is depicted alongside the count rate curve in Figure 2.3-13 (red solid line). In terms of detector design which aims at reducing the dark count rate, it can be concluded as before that large experimental critical current values are important in reducing the dark count rate.

2.3.3.6 PHOTON COUNTS

Several models have been suggested to describe the superconductivity breakdown dynamics after photon absorption on a microscopic scale. Early models were based on the idea of a photon-induced hotspot of suppressed or reduced superconductivity and the subsequent redistribution of the bias current [47], [167]. Newer models involve magnetic vortex excitation in the detection process [113],

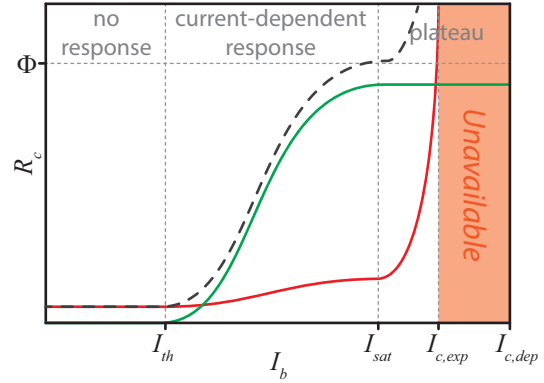


Figure 2.3-13: Illustration of reduced experimental critical current on count rate (green) and dark count rate (red). The dashed line represents the combined curve

[114]. The most recent studies use numerical approaches [115], [159], [168]. A detailed review of the individual models can be found ref. [112], here the salient aspects will be reported. Although none of the models are currently able to reproduce the SNSPD's behavior under all circumstances and conditions, agreement with experimental data clearly indicates the involvement of quasi-particle diffusion and vortex nucleation. In the first instance, the photon absorption creates an athermal, excited state which causes the creation of quasi-particles (QPs). The QPs diffuse and cause a local reduction of the superconducting order parameter, which locally reduces the vortex entry barrier. For sufficiently strong bias currents, the entry barrier vanishes completely and vortices begin to form. Being subjected to the bias current these vortices experience a Lorentz force as described in section 2.3.3.3, which leads to the formation of a normal conducting domain by vortex-induced phase slips (VPSs).

The models differ in their description of numerous parameters. For instance, some models assume a complete suppression of the order parameter, others merely a reduction; some models only include the formation of QPs, others allow for the re-condensation into Cooper pairs. The list of differences is large, yet the inclusion of QP diffusion and vortex nucleation into the models currently reproduce experimental data more accurately than other models [112].

An implicit, but important consequence of the QP diffusion is the resulting dependence of the detection efficiency on the nanowire's cross-sectional area. The diffusion of QPs covers a finite volume which is determined by the photon energy and limited by the wire's spatial boundaries. In narrower⁹ nanowires, the relative spatial extent over which the order parameter is reduced is larger than in wider nanowires. As a consequence, vortices will form more easily in narrower nanowires than in wider nanowires, given constant photon energy. As a consequence, lower bias current strengths are needed to diminish the vortex entry barrier in narrower wires which effectively causes a reduction in the saturation and threshold current values (see Figure 2.3-14). In the normal incidence configuration, a reduction in wire width is accompanied by a reduction in the absorption efficiency due to the decreased filling fraction of the absorbing detector element. Nevertheless,

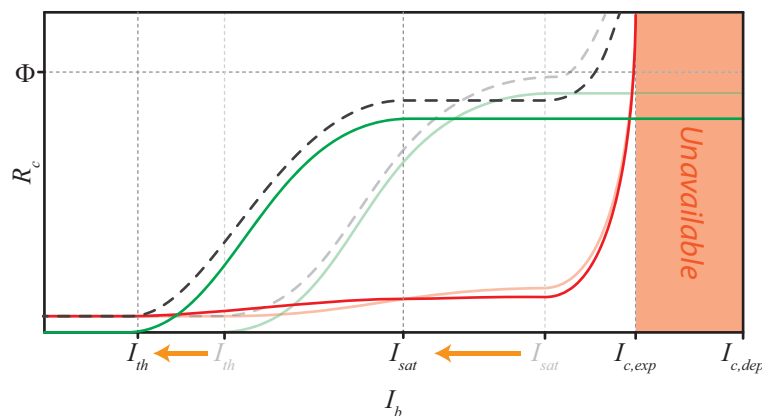


Figure 2.3-14: Idealized illustration of down-shifted threshold and saturation current in nanowires of smaller cross-section. The dark green and dark red solid lines represent the count rate and dark count rate, respectively, of a SNSPD using a narrow nanowire; the light green and light red solid lines represent the same quantities of a comparable SNSPD using a wide nanowire. The dashed lines depict the combined curves. The difference in magnitude originates from a change in the absorption efficiency.

⁹ The cross-sectional area is the determining factor, but it is safe to assume constant thickness along wire.

adjustments of the nanowire width provide a means to expand the SNSPD's detection plateau. Alternatively, it can be exploited to increase the detector's sensitivity for smaller photon energies. This will be addressed in the next section.

2.3.4 SPECTRAL SENSITIVITY AND WIRE CROSS-SECTION

The spectral sensitivity is closely related to the detection models presented in the foregoing section. It was mentioned, in particular, that the photon energy and bias current both contribute to the reduction of the edge barrier. Renema et al. were able to show experimentally that the two quantities are linearly dependent such that deficiencies in the one can be counterbalanced by proportional increases in the other [169]. This contrasts SNSPDs from semiconductor based devices which are limited by the bandgap of the material. Yet, the SNSPD's bias current can only be adjusted within a certain range to compensate for low photon energies. When the bias current approaches the wire's critical current, the dark count rate will increase drastically. Yet, as was outlined in the previous section, the vortex entry barrier which needs to be reduced in order to facilitate superconductivity breakdown is not only current-dependent, but also volume-dependent. Therefore, in order to maintain the energy density for different photon energies, the nanowire cross-section has to be adjusted. In turn, this enables spectral sensitivity tuning through adjustments in wire width and thickness. Studies have shown that NbN-based SNSPDs could theoretically be operated over a spectral range extending from 500 nm in the visible to 5.6 μm in the infrared [170]. Standard applications mostly aim for visible light detection or NIR detection around 1,550 nm. In this range SNSPDs efficiencies usually lie above the 50% threshold with some approaching unity [111].

2.3.5 TIMING CHARACTERISTICS

SNSPDs are especially sought after because of rapid response, fast recovery, and low timing jitter. In the following we will review those characteristics and explain their origins to the extent possible.

2.3.5.1 RISE TIME

Experimentally obtained SNSPD rise times are on the order of a few hundred picoseconds [47], [171]. The timing is determined by the microscopic mechanisms involved, i.e. electron-phonon scattering, quasi-particle diffusion, and vortex-crossing time. The vortex crossing time suggests a weak dependence on the wire geometry.

2.3.5.2 RECOVERY TIME

The detector recovery time τ_R is mostly limited by the wire's kinetic inductance L_K , i.e. $\tau_R = L_K/R_L$. The kinetic inductance is determined by the length and the cross-section of the nanowire, i.e. $L_K \propto \frac{l}{A}$ (see section 2.3.2.3). Longer nanowires increase the kinetic induction, while larger cross-

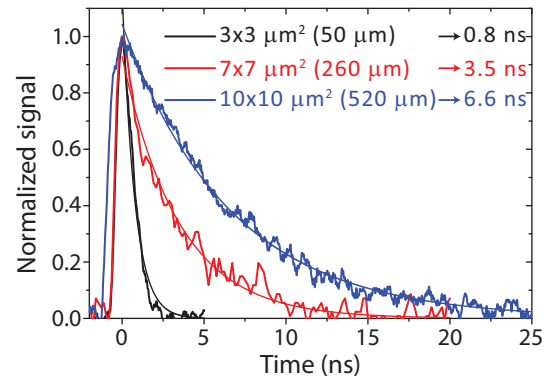


Figure 2.3-15: Decay times of three differently sized SNSPDs designed for normal incidence boasting a 50 μm long (black), a 260 μm long (red), and a 520 μm long (blue) meandering nanowire to obtain the area coverages indicated in the graph. Data provided courtesy of V. Kovalyuk at Scontel.

sections lead to its reduction (see Figure 2.3-15). The length and cross-section, therefore, constitute degrees of freedom to adjust the recovery time within a certain limit for specific application needs.

The intrinsic superconductivity recovery time, on the other hand, is much shorter (< 700 ps [171]). It is determined by the phonon escape time $\tau_{es} \approx 40$ ps [107], [167], i.e. the time it takes thermalized phonons inside the nanowire to dissipate into the environment. The exact times clearly depend on the employed materials, the geometry, and the ambient temperature.

2.3.5.3 TIMING JITTER

The timing jitter in SNSPDs is very low at values around 50 ps. The physical origins have not yet been thoroughly investigated. There seems to be a dependence on the bias current strength with the jitter reducing for stronger currents [172]. Some aspects of the timing jitter will be addressed as part of this thesis, but the intrinsic mechanisms which determine the timing jitter have yet to be uncovered.

2.3.6 ENHANCEMENT OF THE ABSORPTION EFFICIENCY

It was explained at the beginning of this section on SNSPDs that the detection efficiency is the product of the detector's internal quantum efficiency (IQE) and absorption efficiency (AE). The IQE inherently depends on the microscopic breakdown dynamics. Bias current, photon energy, and wire geometry were shown to offer means for an optimization of the IQE. The AE, on the other hand, depends on the material properties and the distance over which photons can be absorbed. This distance is given by the very small nanowire thickness of $d \approx 4$ nm and limits the SNSPD's detection efficiency to a few percent [59]. Multi-element SNSPDs have been implemented in a first instance which enabled an increase of the detection efficiency to 25% [173] and even 36% [174]. Alternatively, resonant cavities have been used to artificially extend the absorption length [108], [109]. One particular implementation achieved detection efficiencies of 93% through cavity enhanced absorption [111]. The use of cavities as a means to increase the absorption efficiency, however, adversely impacts the timing resolution and bandwidth of the detector. In the case of the cavity SNSPD reported ref. [111], the voltage signal pulse decayed over 120 ns and the timing jitter was as large as 150 ps. Ultimately, the use of cavities enables a significant enhancement of the detection efficiency, but at the cost of poorer timing performance.

2.3.7 SUMMARY

The SNSPD is an emerging detector technology which offers extremely good performance in almost all important detection categories (see table below): it is sensitive over an extremely wide spectral range; it exhibits extremely low dark count rates down to less than one Hertz; its timing accuracy around 50 ps timing jitter is excellent; and recovery times in the nanosecond range allow for high count rates. The combination of these factors makes the SNSPD a unique detector which is highly attractive for demanding applications, in particular, in the field of quantum information.

Being based on a superconductor instead of a semiconductor offers the critical advantage of sensitivity over a broad spectral range. The detection mechanism is based on the local formation of a normal-conducting domain upon the absorption of a photon. The photon energy needed to induce the formation is given by the edge barrier potential of the superconducting nanowire which can be

adjusted by the nanowire cross-section and the applied bias current. This allows for sensitivity tuning over a broad spectral range.

Detector	Detection efficiency	Dark Count Rate	Timing Jitter	Max. Count Rate	Number Resolution	Reference
PMT	40% @500 nm	100 Hz	300 ps	10 MHz	Yes	[97]
PMT	2% @1550 nm	200 kHz	300 ps	10 MHz	Yes	[97]
SPAD (thick junction)	65% @650 nm	25 Hz	400 ps	10 MHz	No	[71]
SPAD (thin junction)	49% @550 nm	25 Hz	35 ps	10 MHz	No	[49]
SPAD (gated)	10% @1550 nm	91 Hz	370 ps	10 kHz	No	[98]
SPAD (self-differencing)	10% @1550 nm	16 kHz	55 ps	100 MHz	No	[99]
TES	50% @1550 nm	3 Hz	100 ns	100 kHz	Yes	[80]
TES	95% @1556 nm	-	-	100 kHz	Yes	[79]
QD Tunnel Diode	12% @550 nm	2 mHz	150 ns	250 kHz	Yes	[87]
QD FET	68% @805 nm	-	-	1 Hz	Yes	[85]
Up-Conversion	50% @1550 nm	460 kHz	-	5 MHz	No	[90], [91]
VLPC	88% @694 nm	20 kHz	40 ns	10 MHz	Yes	[95]
VLPC	40% @ 633 nm	25 kHz	240 ps	10 MHz	Yes	[100]
SNSPD	0.7% @1550 nm	10 Hz	60 ps	100 MHz	No	[59]
SNSPD (multi-element)	36% @1550 nm	280 Hz	-	100 MHz	Yes	[174]
SNSPD (cavity)	93% @1550 nm	1 Hz	150 ps	25 MHz	No	[111]

A major limitation of the otherwise excellent detection capabilities is its low absorption efficiency which limits the overall detection efficiency to around 1%. Multi-element SNSPDs are able to increase the efficiency up 36% [174] and by the use of cavities to artificially extend the absorption length efficiencies close to unity have been reached [111]. This increase is, however, accompanied by an undesired reduction in timing performance. An alternate possibility to increase the absorption length, but maintain the SNSPD's outstanding timing characteristics can be achieved by photonic integration. This will be discussed in the following chapter.

3 SNSPD INTEGRATION AND CHARACTERIZATION

The integration of the SNSPDs with nanophotonic circuitry allows for the tunable enhancement of the detector's efficiency and the realization of almost limitless scalability. This chapter provides a brief introduction into the concept of waveguide integration. The detector design parameters and the fabrication procedure are explained. Several detectors of different geometries for the telecommunication wavelength at 1550 nm on a silicon-nitride platform are fabricated and characterized. For specific designs, close to unity detection efficiency with plateau behavior is realized.

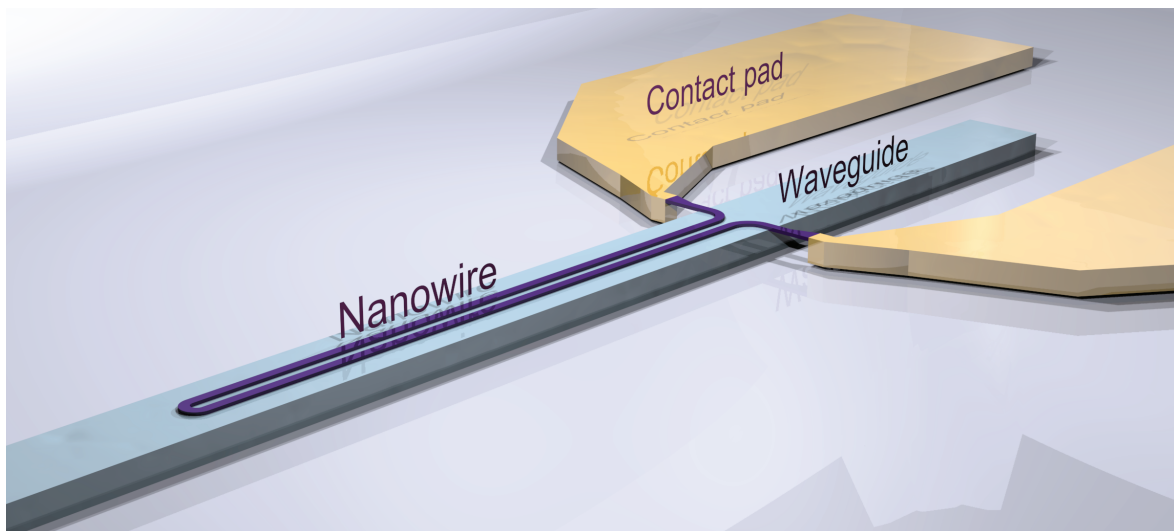


Illustration of waveguide-integrated SNSPD

3.1 FUNDAMENTALS OF INTEGRATED SNSPDs

The motivation for integrating SNSPDs with nanophotonic circuitry is twofold: by exploiting near-field coupling over an extended distance along the waveguide the limitation of the short absorption length in conventional SNSPDs is overcome; secondly, the integration resolves the scalability issue which presently exists with conventional SPD technologies.

In 2009 Hu et al. proposed two configurations for the photonic integration of SNSPDs [52]. One of those two designs suggested a layout in which the nanowire interfaces directly with an optical

waveguide. By using such a configuration the detection efficiency is substantially enhanced and detector scalability is realized.

The first implementations by Sprengers on a gallium-arsenide (GaAs) ridge waveguide in 2011 [53], Pernice on silicon in 2012 [55], and Schuck on silicon-nitride (Si_3N_4) in 2013 [56] used a slightly altered design, but the same general concept in which the superconducting nanowire is situated directly on top of an optical waveguide (see picture at chapter beginning). Newer implementations were employed to detect the emission of on-chip quantum dots [54] or surface plasmon polaritons in plasmonic waveguides [175], [176].

The transition from the normal incidence configuration to the integrated layout has virtually no impact on the detection mechanism of the SNSPD such that its basic features and properties remain unchanged. However, some additional degrees of freedom arise in the integrated design. Some of these offer additional room for optimization which will be addressed in the following sections.

3.1.1 INTEGRATED OPTICS

In order to understand the principle of a nanowire used as a detector element on top of an optical waveguide, it is advisable to review the basics of photonic waveguiding structures. From a basic perspective, integrated optics and photonics is the optical equivalent to the electronic integrated circuit (IC). Instead of guiding electronic signals through conductors, waveguides made from an optically transparent medium are used to route light signals across a chip.

WAVEGUIDES

Light confinement in integrated optics and photonics is, in general, achieved by launching light into a guiding structure of higher optical density than its surrounding materials. By designing suitable geometries it is possible to effectively eliminate divergence and guide light along a predefined path. One hence speaks of *guided optical modes* [177]–[179].

The basic phenomenon leading to optical confinement and guided modes can be understood even in a simplified ray optics picture. Figure 3.1-1 shows a dielectric slab of two different materials with refractive indices n_1 and n_2 with $n_2 > n_1$. For light propagating inside the inner material, there exists a minimal angle of propagation α^* relative to the interface below which light is *completely* reflected at the boundary. The effect is commonly referred to as *total internal reflection*. Light, if launched into the central layer under a sufficiently shallow angle (smaller than α^*), will thus remain confined inside the inner *guiding layer* without any loss into the surrounding layers.

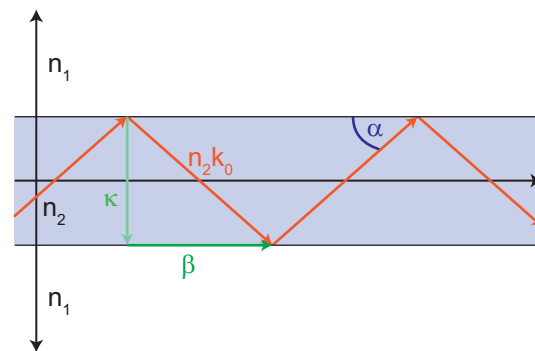


Figure 3.1-1: Two-dimensional sketch of optical confinement principle inside a slab waveguide using ray optics picture. The rays will be reflected 100% at the interface as long as the angle of incidence is below the angle of total internal reflection.

The simplified treatment used above lends itself nicely for an intuitive explanation, yet it fails to explain more complex phenomena, such as mode leakage and mode coupling. To explain these effects, a rigorous electromagnetic analysis of guided modes is required.

Standard waveguide geometries are invariant under translation in the direction of propagation and common guiding materials are lossless and homogeneous in their respective geometrical domain. As a consequence, simple plane waves constitute valid solutions to the wave equation in those areas [177], [180]:

$$\begin{aligned}\mathbf{E}(\mathbf{r}) &= \boldsymbol{\mathcal{E}}_m(x, y)e^{i(\omega t - \beta_m z)} \\ \mathbf{H}(\mathbf{r}) &= \boldsymbol{\mathcal{H}}_m(x, y)e^{i(\omega t - \beta_m z)}\end{aligned}\quad \mathbf{3.1.1-1}$$

where the $\boldsymbol{\mathcal{E}}_m(x, y)$ and $\boldsymbol{\mathcal{H}}_m(x, y)$ denote the spatial mode profiles, β_m is the mode's propagation constant, and the subscript m designates the mode itself. The spatial mode profiles are obtained by matching the boundary conditions to ensure wave function continuity. Under certain circumstances this can be achieved analytically; the more usual approach, however, involves the utilization of numerical methods such as the Finite Element Method (FEM). For the work conducted for this thesis, a commercial FEM solver, COMSOL Multiphysics®, was employed.

A typical mode profile obtained from a COMSOL simulation is depicted in Figure 3.1-2. As can be seen, the mode is predominantly located inside the waveguide with smaller sections – called *evanescent fields* – leaking into the surrounding areas. The fields inside the waveguide usually possess a pattern similar to standing waves in an optical resonator and the evanescent tails decay exponentially into the environment. The degree of mode confinement is determined by the refractive index contrast between the waveguide and the environment, and by the spatial constraints set by the waveguide geometry. As light confinement is limited by diffraction, reducing the waveguide volumes will result in increasing evanescent tails until the guided mode eventually becomes an uncontained radiative mode [177]. Conversely, the extension of the waveguide volume enables the formation of higher order modes.

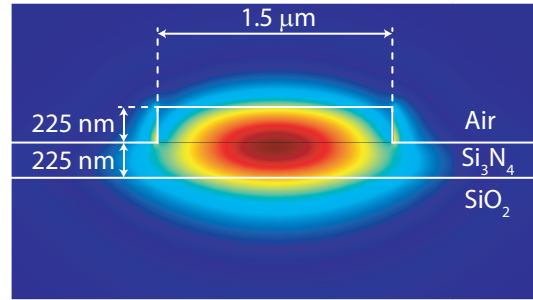


Figure 3.1-2: Electric field mode profile of a typical ridge waveguide structure calculated by COMSOL Multiphysics. The ridge is 225 nm high and 1.5 μm wide situated atop a 225 nm high layer of the same material.

The propagation of guided modes is affected proportionately by all permeated materials: the core part of the mode experiences the waveguide material's refractive index, whereas the evanescent fields 'feel' the refractive indices of the surrounding materials. The optical mode as a whole therefore propagates with a mode propagation constant β_m which is proportional to an *effective refractive index* or *mode index* n_{eff}^m :

$$\beta_m = n_{eff}^m \frac{2\pi}{\lambda}\quad \mathbf{3.1.1-2}$$

where λ denotes the optical wavelength in vacuum.

From a mathematical perspective, equations 3.1.1-1 form a complete, orthonormal set of solutions to Maxwell's equations [181]. The mutual orthogonality is especially useful as it enables

the simultaneous, but independent existence of multiple modes in the waveguide. In other words, if a specific number of modes is launched into a specific waveguide, these modes will propagate independently, i.e. without any coupling between them, along the waveguide; no additional modes arise and none are lost unless perturbed externally.

GRATING COUPLERS

In order to couple light into a photonic waveguide an appropriate optical mode must be excited. Various methods exist for this purpose (e.g. end coupling, prism coupling [177], [180]). In this thesis, *grating couplers* (GCs) are chosen. Although limited in efficiency the benefit of using GCs is the possibility to couple light into and out of the on-chip circuitry with experimental ease by positioning an optical fiber in close proximity to the GC. Certain coupling conditions must be fulfilled for successful mode excitation which can be understood in a picture analogous to a diffraction grating (see Figure 3.1-4): the grating is composed of a periodic arrangement of ridges at the end of a waveguide. The ridges are of the same material as the waveguide itself and the grating's geometry is defined by two independent variables – the periodicity Λ , and the filling fraction FF which defines the ratio of ridge width and gap.

The well-known diffraction grating equation $\Lambda \sin \alpha + \Lambda \sin \alpha' = m\lambda$ with $m \in \mathbb{N}$ determines the insertion conditions for the diffraction order m at angle α' of light incident onto the grating at angle α [177]. Although intuitively correct, the diffraction analogy fails to explain the polarization dependence, bandwidth and efficiency of the coupling. For a complete analysis, coupled mode theory must be employed [180]. This approach regards the grating as a perturbation which under phase matched conditions allows for the incident mode to couple to the waveguide mode. The phases are matched by adjusting the periodicity Λ as well as the fill factor FF of the grating. The grating couplers fabricated for this thesis were initially designed using the grating equation and subsequently optimized by experimentally varying the

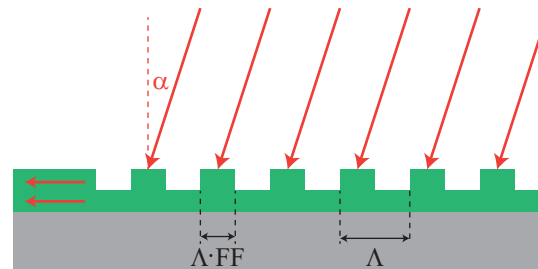


Figure 3.1-4: Illustration of grating coupler operation based on diffraction grating principle

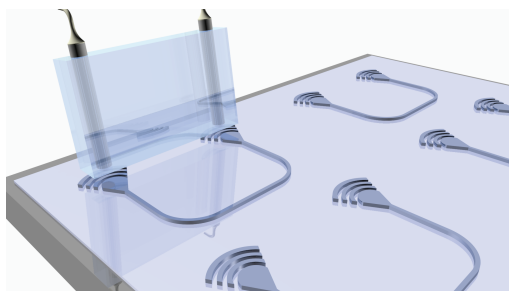


Figure 3.1-3: Light is coupled into and out of a photonic waveguide by positioning an array of optical fibers above the GCs.

grating period and fill factor. This method was chosen over a rigorous theoretical approach due to fabrication uncertainties. Figure 3.1-3 depicts the coupling method used in this thesis: the ends of an array of optical fibers are encased in a glass housing which can be positioned on top of the GCs for light insertion and extraction. Different versions of the array with up to twelve fibers enable simultaneous coupling on multiple GC ports. The array can be moved freely across the chip which allows for flexible access to numerous devices.

3.1.2 DETECTION BY NEAR-FIELD COUPLING

The integration of a SNSPD with a photonic waveguide is achieved by placing the nanowire in the optical mode's evanescent field on top of the waveguide structure. The nanowire thereby causes the field lines to rearrange and crowd around the nanowire's edges (see Figure 3.1-5). Due to the nanowire's absorptivity, the optical mode is gradually absorbed by the nanowire as it propagates. The photon absorption therefore occurs over the length of the nanowire-covered area inside the waveguide without the need to route photons off-chip into external detection units.

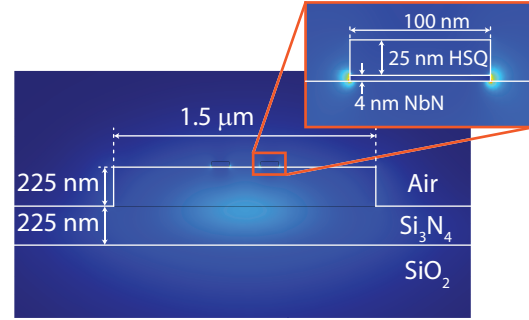


Figure 3.1-5: FEM simulation of the waveguide mode including 4 nm thick NbN stripes; 25 nm non-removable HSQ resist from fabrication have been included.

In analogy to the conventional SNSPD's detection efficiency η_{de} , it is useful to define the detection efficiency for on-chip applications, i.e. the *on-chip detection efficiency* (OCDE)

$$\eta_{OCDE} = \eta_{ae} \times \eta_{iqe} \quad 3.1.2-1$$

where η_{ae} and η_{iqe} denote the previously defined absorption efficiency (AE) and internal quantum efficiency (IQE), respectively. In contrast to the normal incidence configuration in which the AE is limited by the absorption distance $d \approx 4$ nm, the integrated SNSPD offers the potential for almost limitless AE by extending the nanowire-covered area on the waveguide. Practical limits are set by the spatial dimensions of the photonic circuitry and the fabrication.

3.1.3 CURRENT STATE OF INTEGRATED SNSPD RESEARCH

SNSPD integration is a new technology and a vibrant field of research. It is therefore useful to review the current state of research in detail to provide context for the results presented in this chapter.

The first realization of a waveguide-integrated SNSPD used GaAs as waveguiding material and a NbN nanowire structure consisting of four 100 nm wide, 50 μ m long, parallel stripes and three U-turn bends (W-shape) [53]. A moderately high OCDE of $\eta_{OCDE} = 19.7\%$ was achieved with a timing jitter of 60 ps and a few nanoseconds recovery time. They report a numerically calculated absorption efficiency of $\eta_{ae} = 90\%$ and attribute the resulting internal quantum efficiency (IQE) of $\eta_{iqe} = \eta_{OCDE}/\eta_{ae} = 17.7\%$ to fabrication-related imperfections of the nanowire.

The implementation on silicon waveguides employed two long parallel NbN stripes with a single U-turn bend of varying width and length [55]. The presented data shows a maximal OCDE of $\eta_{OCDE} = 91\%$ for a 100 nm wide, 20 μ m long SNSPD, but no clear OCDE trend with respect to wire width or length. Timing jitter values of 50 ps and decay times in the nanosecond range are reported. Analysis of the decay time shows a clear linear growth with wire length which indicates limitation by the wire's kinetic inductance.

Schuck et al. performed several studies in which they analyzed the width, length and wavelength dependence of NbTiN-based integrated SNSPDs on Si₃N₄ [56], [182]. A clear difference was seen in the response to wavelengths in the visible at 768 nm and the NIR at 1542 nm with the OCDE values in the visible being significantly higher at lower bias current and saturating for higher currents. The plateau behavior was found to increase with reducing wire width and the overall OCDE value tends to grow with wire length. OCDE values as large as $\eta_{OCDE} = 80.1\%$ were achieved in the visible. In the NIR regime at 1550 nm, a similar trend was found, but the efficiency reduced to $\eta_{OCDE} = 67.7\%$. OCDE saturation in the NIR was not seen. Additionally, the noise levels were studied and found to be in the milli-hertz range which corresponded to a noise-equivalent power (NEP) of 10^{-20} WHz^{-1/2}.

Reithmeier et al. used a meandering SNSPD geometry which resembles the conventional fiber-coupled, normal-incidence SNSPDs [54] integrated with a GaAs waveguide. An on-chip photoluminescence experiment is reported in which the SNSPD collected the emission from a quantum dot at 940 nm with a relatively poor detection efficiency of 0.1% which is mainly a consequence of small IQE due to a very thick 10 nm NbN layer. Timing accuracy is excellent at 72 ps.

Heres et al. performed experiments using a pair of SNSPDs integrated with plasmonic waveguides in order to measure the quantum interference of surface plasmon polaritons in an integrated plasmonic circuit [175], [176]. By placing the detector close to the metallic guiding structures, near-field coupling was enabled and Hong-Ou-Mandel interference was measured in a temporal coincidence measurement. High accuracy was achieved due to the low timing jitter of 50 ps of the integrated SNSPDs.

Initial data show extremely promising results with OCDE values approaching unity in the visible and also the NIR. Geometrical dependencies have been experimentally evaluated, yet in the IR the indicated trends show potential for optimization. Timing accuracy appears to be as small as in conventional SNSPDs below 100 ps and the recovery times are in the usual nanosecond range.

3.2 MATERIAL PLATFORM AND PROPERTIES

Before delving into the details of device design it is necessary to introduce the materials which are employed for device fabrication. The photonics material platform is based on silicon nitride (Si₃N₄) and the superconducting nanowires are made from NbN. In this section a few material parameters will be examined more closely and a motivation for the choice of materials is given.

3.2.1 SILICON NITRIDE (Si₃N₄)

The utilized Si₃N₄ platform is commercially available¹⁰ and consists of a standard three layer system of – from top to bottom – a stoichiometric Si₃N₄ layer, a silicon dioxide (SiO₂) layer, on intrinsic silicon. Two different layer thickness configurations were used: photonic devices designed for NIR applications used a 450 nm Si₃N₄ layer on 2.6 μm SiO₂, whereas visible light applications are based on a 200 nm Si₃N₄ layer on 2.0 μm SiO₂. According to the manufacturer's specifications the layer thicknesses vary by no more than 5%.

¹⁰ Rogue Valley Microdevices, Medford, OR 97504, USA

Si_3N_4 is used as a basis for optically integrated devices since the late 1980s [183] and is fully compatible with well-established CMOS processes. It offers several advantages over the commonly used silicon-on-insulator (SOI) platform, among them broad optical transparency from the UV to the IR due to an electronic bandgap just below 5 eV, low free carrier concentration for reduced absorptive losses, and its large refractive index enables tight optical confinement [184]–[187]. Of particular interest for quantum optical applications is the recently discovered surface-nonlinearity ($\chi^{(2)}$) which holds promise for the creation of non-classical light sources on Si_3N_4 [188].

The following Sellmaier equation from ref. [189] was used to obtain refractive index data for the simulations in this thesis

$$n^2 - 1 = \frac{2.8939\lambda^2}{\lambda^2 - 0.13967^2} \quad \text{3.2.1-1}$$

3.2.2 NIOBIUM NITRIDE (NBN)

NbN is a type-II superconductor with a bulk transition temperature of 16 K [129], [138]. This is comparatively high for a low temperature superconductor. In thin films and nanowires, the transition temperature is reduced to 8 – 10 K (see Figure 3.2-1) due to the proximity effect at the normal-conductor to superconductor interface. NbN is, furthermore, compatible with Si_3N_4 such that thin NbN films can be deposited onto Si_3N_4 without negatively affecting its superconducting properties.

The sputter-coated NbN films utilized for the fabrication of the nanowires are prone to oxidization under standard atmospheric conditions [190], [191]. At room temperature, the oxidization appears to be slow enough that samples are not affected if stored inside a desiccator. At elevated temperatures, the oxidization process is accelerated and material degradation sets in. This is particularly critical during fabrication.

The refractive index data used for the simulations in this thesis were taken from ref. [192]

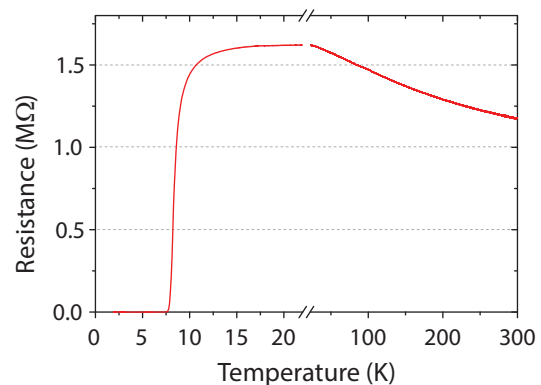


Figure 3.2-1: Resistance vs. temperature curve measured at 80 nm wide, 4 nm thick nanowire

3.3 DETECTOR DESIGN AND FABRICATION

As part of this thesis integrated SNSPDs for the detection of single photons in the NIR at 1550 nm and in the visible at 740 nm were designed and fabricated. In this chapter the detectors for the NIR will be presented. The designs used half-etched 225 nm high, 1.5 μm wide ridge waveguide structures to support transverse-electric (TE) mode propagation at 1550 nm.

3.3.1 DETECTOR GEOMETRY

The detector geometry consists of two long, straight stripes which are connected at one end to form a long single wire (see Figure 3.3-1). In contrast to conventional SNSPD designs which use rectangular turns, semi-circular turns are employed in order to reduce current crowding effects.

The geometry provides degrees of freedom which are utilized as design parameters: the nanowire stripe *width*, the *gap* between the stripes, and the length along the waveguide which we will refer to as *detector length*. It should be emphasized that the nanowire length is different from the detector length: in the chosen geometry the nanowire is twice as long as the detector and the absorption distance is determined by the detector length.

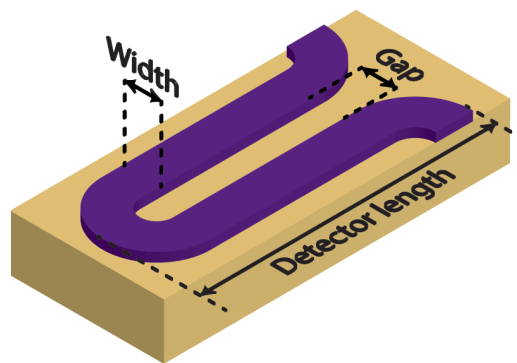


Figure 3.3-1: Sketch of the integrated SNSPD geometry fabricated for this thesis. The waveguide (yellow) is covered by a U-shaped nanowire (purple)

The three parameters can be chosen to realize varying detector characteristics. For instance, an extension of the detector length directly increases the absorption efficiency (AE) and therefore the on-chip detection efficiency (OCDE). On the other hand, the longer nanowire also increases the kinetic induction and, therefore, the recovery time. The experimental study presented in this chapter aims at identifying the influence of the geometrical parameters in order to optimize the OCDE at 1550 nm.

A preliminary assessment to restrict the parameter range is advisable. An immediate limitation is given by the employed electron beam lithograph's write-field size of $100 \times 100 \mu\text{m}^2$. In order to avoid stitching errors¹¹ during the fabrication, the nanowire should fit inside one write-field and is thus constrained to an area of $100 \times 100 \mu\text{m}^2$.

Furthermore, the effect of width and gap variations on the AE can be assessed numerically. The nanowire designs are translationally invariant along the waveguide and for sufficiently long detectors the absorption contributions from the nanowire tip and contact pad area can be neglected. As a consequence, the absorption along the detector is independent of its position such that according to Beer's law $dI/dz = -\alpha I$ the AE scales exponentially with wire length. This fact can be exploited for numerical mode calculations in order

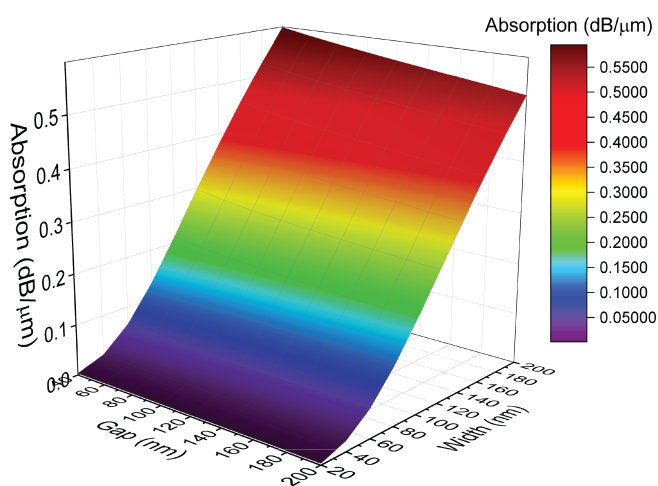


Figure 3.3-2: Absorption coefficients of nanowire for varying width and gap on a half-etched 225 nm high, 1.5 μm wide ridge waveguide

¹¹ Stitching errors are caused by misalignment of neighboring write fields in electron beam lithography.

to obtain the propagation loss constant α : the 2D mode solver of COMSOL Multiphysics can be used to calculate the effective mode index of the nanowire-covered waveguide. Its imaginary part κ is related to the absorption coefficient through $\alpha = 4\pi\kappa/\lambda$ where λ is the light's wavelength. The resulting absorption coefficient for a half-etched 225 nm high, 1.5 μm wide ridge waveguide are shown in Figure 3.3-2.

Two trends are visible in Figure 3.3-2: the absorption grows strongly with increasing wire width and it declines as the gap between the stripes grows. The dependence of the absorption on the gap between the stripes is weak: while a gap reduction from 200 nm to 40 nm yields an average¹² gain of 10% in absorption; in contrast, an increase in nanowire width from 20 nm to 200 nm produces a 200-fold gain. The variations in wire width by far dominate the absorption and thus the AE in SNSPDs. As a consequence of the minor impact of the gap parameter, it was decided to focus mainly on the evaluation of detector length and wire width. Although for the simulations performed for one particular waveguide geometry – half-etched 225 nm high, 1.5 μm wide ridge waveguide – the general trend is believed to be generally applicable.

3.3.2 FABRICATION

The nanophotonic structures and integrated detectors in this thesis were all fabricated using conventional nano-lithographic techniques. These include electron beam lithography (EBL), reactive ion etching (RIE), and physical vapor deposition (PVD). Moreover, a standard spin-coater was used to deposit the resists used during EBL, and a white light reflectometer allowed for the precise analysis of thicknesses of deposited and etched layers.

The fabrication recipes were adjusted many times over the course of this thesis, partially in an attempt to improve on previous fabrication runs, and partially in order to compensate for changes in the fabrication conditions. In particular, the aforementioned NbN degradation due oxidization had to be addressed. Conventional baking, drying, and cleaning steps had to be altered. High temperatures were reduced and oxygen cleaning plasmas were first reduced and eventually abandoned. Here, the most reliable fabrication procedure is presented. Details about the individual recipes can be found in annex A1.

STEP 1: CIRCUIT DESIGN

The individual photonic circuit and detector designs were created using self-made Python scripts. The approach was chosen as it constitutes an easy, reliable and unrestricted way to generate and freely parameterize all components. Numerous libraries containing single components and more advanced layouts were created throughout this thesis. The final layered circuit layout is saved as a conventional

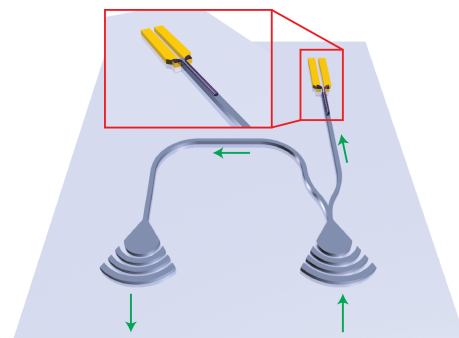


Figure 3.3-3: Photonic circuit layout for SNSPD characterization

¹² The average pertains to the range of the simulation.

GDSII¹³ file which is compatible with standard nanofabrication machines.

For the work presented in this chapter, the circuit design shown in Figure 3.3-3 was created. It represents the standard layout for integrated SNSPD characterization. This design separates light which is input through a GC into two arms by a 50:50 Y-splitter. Half of the light is guided toward the detector and the other half is routed toward the output GC. The output signal serves as reference from which the exact photon number travelling toward the detector can be extracted.

STEP 2: NBN DEPOSITION

The starting material for the fabrication of the hybrid superconducting-nanophotonic circuitry is the Si₃N₄ multilayer structure introduced in the preceding section. As a first step, a thin NbN layer is deposited by magnetron-sputtering in an argon-nitrogen atmosphere [51]. This step was performed externally by our collaborators Gol'tsman et al., and in particular by Vadim Kovalyuk, at the Moscow State Pedagogical University. The layer thickness is usually 4 nm. Right after fabrication the sheet resistance is measured, which will later serve as basis in determining the nanowire width. Usual sheet resistance values are $R_{sq} \approx 600 \Omega/\text{sq}$.

In the following the individual fabrication steps will be presented in chronological order. The detailed parameters including e.g. exposure dose and spin speed, are presented in appendix A1.

STEP 3: CONTACT PADS AND ALIGNMENT MARKERS

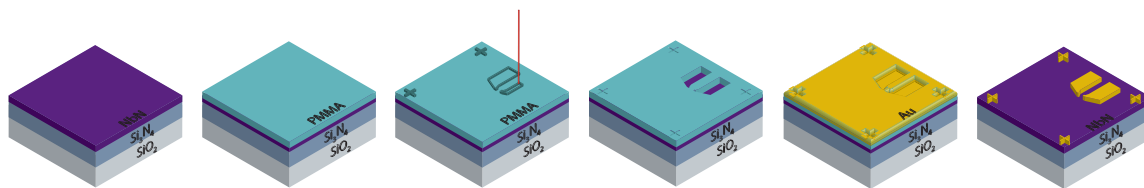


Figure 3.3-4: Fabrication procedure for contact pads and alignment markers

The first lithographical step entails the realization of contact pads for electrical connectivity of the devices and alignment markers for subsequent lithography steps. A graphical representation of the following steps is given by Figure 3.3-4. An 800 nm thick coat of poly methyl methacrylate (PMMA) 450k 8% is used as positive tone resist in an EBL exposure in order to transfer the designed pattern into the resist layer. The exposed sample is developed in a mixture of isopropanol and methyl isobutyl ketone (MIBK) leaving behind an 800 nm thick positive PMMA mask. The contact pad material is deposited onto the sample using a PVD process: a 5 nm thin chromium (Cr) layer serves as adhesion promoter for the 120 nm gold (Au) contact pad layer. A lift-off procedure in an acetone bath removes the unexposed PMMA including the Cr and Au remains on top leaving behind a clean sample with Au contact pads and alignment markers.

STEP 4: NANOWIRES

In this step, the NbN layer is structured in order to create the nanowires which later serve as detector elements. Figure 3.3-5 graphically illustrates this step. Initially, a 5 nm thin layer of SiO₂ is

¹³ GDSII (Graphic Data System v2) represents the industry's standard file format for the exchange of integrated circuit layouts.

deposited by PVD. It serves as adhesion promoter for a 55-60 nm thin coat of hydrogen silsesquioxane (HSQ) 2% negative tone resist. During a second EBL exposure the nanowire pattern is transferred into the resist. The sample is developed in a 6.25% tetramethylammonium hydroxide

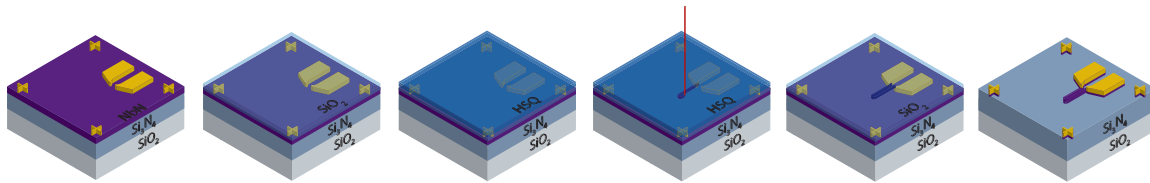


Figure 3.3-5: Fabrication procedure for nanowire

(TMAH) bath which creates a solid HSQ etch mask. The ensuing reactive ion etching (RIE) step utilizes a tetrafluoromethane (CF_4) plasma to first completely remove the 5 nm SiO_2 adhesion layer and, subsequently, etch the 4 nm NbN layer to its full depth thus transferring the nanowire structures into the NbN layer. The Au layer is almost unaffected by this etch process. After this step, the sample contains the previously defined Au contact pads and alignment markers as well as the NbN nanowires. Figure 3.3-7 shows SEM pictures of two examples of finalized NbN nanowires.

It should be noted that the NbN etch step has to be very carefully timed. Continued etching after the complete removal of the NbN layer causes etching into the Si_3N_4 layer underneath. As Si_3N_4 is etched much faster than NbN, a ridge will quickly form below the NbN nanowire. Effectively, this suspends the nanowire from the waveguide which significantly reduces the mode-coupling to the NbN and ultimately diminishes detector efficiency. Furthermore, as the etch process is not perfectly isotropic and since the HSQ resist layer is not perfectly uniform across the wire, over-etching will likely reduce the nanowire's width (see Figure 3.3-6). Conversely, incomplete etching of the NbN layer requires repetition of the etch step to complete the process, which appears to cause material degradation in the NbN. The degradation manifests in severely reduced critical

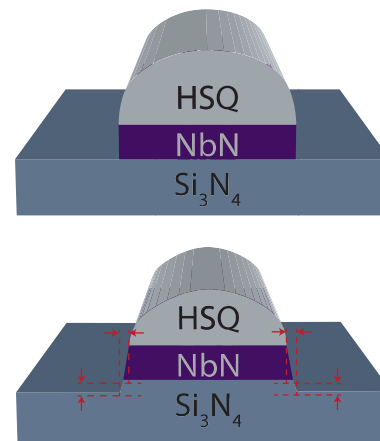


Figure 3.3-6: Illustration of nanowire width reduction by over-etching. Top: perfectly etched NbN layer with residual HSQ on the nanowire. Bottom: excessive etch ablates Si_3N_4 layer and reduces NbN width.

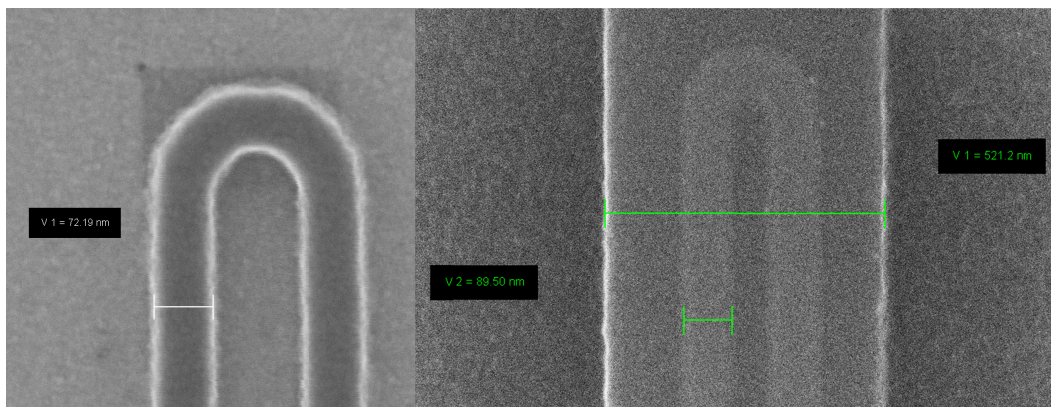


Figure 3.3-7: Left: scanning electron micrograph showing etched 70 nm wide NbN nanowire covered with HSQ remains. Right: SEM picture showing finalized 520 nm wide waveguide with 90 nm wide NbN nanowire on top.

current strengths or even the inability to achieve superconductivity altogether.

STEP 5: PHOTONIC CIRCUITRY

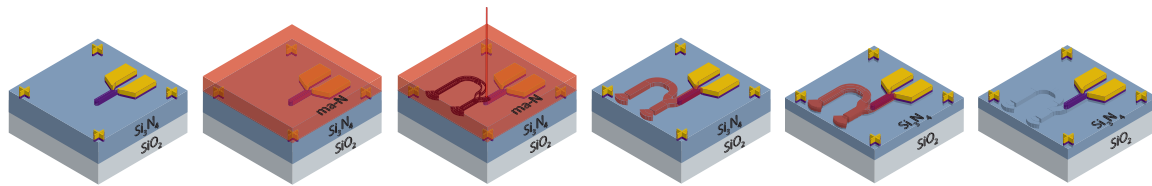


Figure 3.3-8: Fabrication procedure for photonic circuitry

The photonic circuitry is realized by a third EBL exposure using a 340nm thick coat of ma-N 2403 as negative tone resist. After development in MF-319 (2.5% TAMH solution), the photonic structures are transferred into the Si_3N_4 layer by a carefully timed RIE step using a Trifluoromethane (CHF_3) and oxygen plasma. Resist which remains on the structures after the etch process is removed in a N-methyl-2-pyrrolidone (NMP) bath. The completed circuitry is shown in Figure 3.3-9.

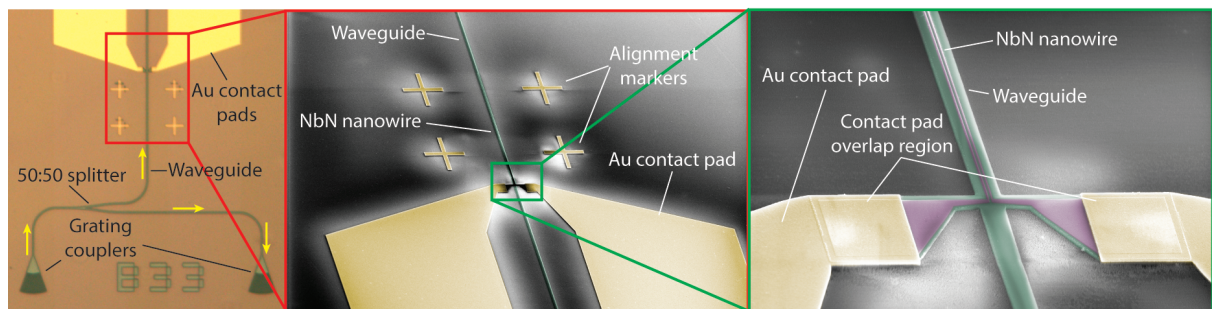


Figure 3.3-9: Optical and false-color SEM pictures showing the completed circuit including the integrated SNSPD. *This data has been previously published in ref. [193]*

FABRICATION ANALYSIS

Every fabrication step includes various tests and checks. In the simplest case, this involves an optical screening using a light microscope, for instance in order to assess the Au contact pads and alignment markers, or reflectometry in order to analyze layer thickness after or before etching or resist thickness before EBL. Moderately advanced checks include width and length measurements of the developed HSQ resist layer before the NbN etch using a scanning electron microscope (SEM) or atomic force microscope (AFM), or optical transmission measurements of the photonic circuitry.

The most important analysis – concerning the nanowire after the NbN etch step – is also the most limited. For a complete detector characterization, knowledge about the exact nanowire width as well as the precise etch depth is necessary. The geometrical width of the nanowire can be indirectly determined by SEM and AFM scans (see Figure 3.3-7 and Figure 3.3-10). The measured

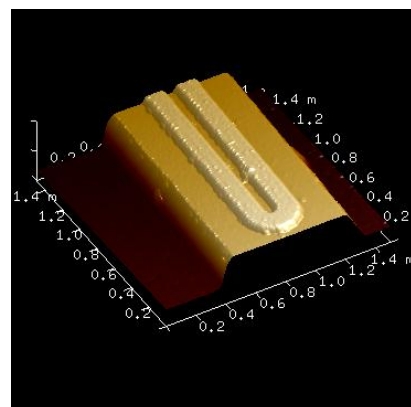


Figure 3.3-10: AFM image of nanowire on top of waveguide. *This data has been previously published in ref. [236].*

entity is, however, not the nanowire itself, but that of the 25 nm thick HSQ layer which remains atop the nanowire after etching and cannot be removed without destroying the sample. The nanowire itself is, therefore, inaccessible to SEM and AFM. As a consequence, its width is only known indirectly from the HSQ cover whose width is not necessarily identical. Resist roll-off at the edges is assumed to introduce an uncertainty of approximately 5 nm on either side of the nanowire. The reported nanowire widths are therefore accurate down to 10 nm.

A precise etch depth examination of the NbN layer by reflectometry is precluded due to limitations in the reflectometer's precision. In order to ensure etch completeness after the NbN RIE process, a measurement of the nanowire's ohmic resistance is performed. Remains of a closed NbN film which has not been completely removed are revealed by extremely low resistance.

3.4 EXPERIMENTAL SETUP

The experimental analysis of the integrated SNSPDs entails the characterization of the salient SPD parameters introduced in chapter 2. In the following the experimental implementation for the assessment of these parameters will be looked at. This includes a review of the cryostat setup for measurements at low temperatures which are required for SNSPD operation and the electronic setup which enables SNSPD read-out.

3.4.1 LIQUID HELIUM FLOW CRYOSTAT

In order to become superconducting, the SNSPDs must be cooled down below their critical temperature at around 8-10 K (see Figure 3.2-1). For this purpose a specially designed helium-4 flow cryostat¹⁴ which has been modified to accommodate for highly flexible fiber optical and electronic access to a cooled specimen is utilized.

3.4.1.1 GENERAL LAYOUT AND CRYOGENIC COOLING

A general layout of the cryostat is shown in Figure 3.4-1. The cryostat itself consists of a long column which, during operation, is inserted into an isolating dewar filled with liquid helium. Two nested chambers are located at the column's end. The specimen including four piezo-positioners as well as electronic and optical connections is located inside the sample chamber. The outer chamber serves as an isolation layer from the 4.2 K cold helium bath. A hollow cylinder with small volume, the *1 K pot*, is located on a second plate right above the sample chamber top flange, also inside the outer chamber. From the 1 K pot as well as from both chambers separate pump lines exit the cryostat. The pump lines from the 1 K pot and the sample chamber combine and connect to a helium pump while the outer chamber pump line is connected to a turbomolecular pump. Each pump line possesses its own valve to regulate the degree of pumping.

¹⁴ Manufactured by Janis Research Inc., Woburn, MA 01801, USA

Figure 3.4-2). The fiber array – when properly aligned – is then able to couple light into and out of the photonic circuitry using the on-chip GCs.

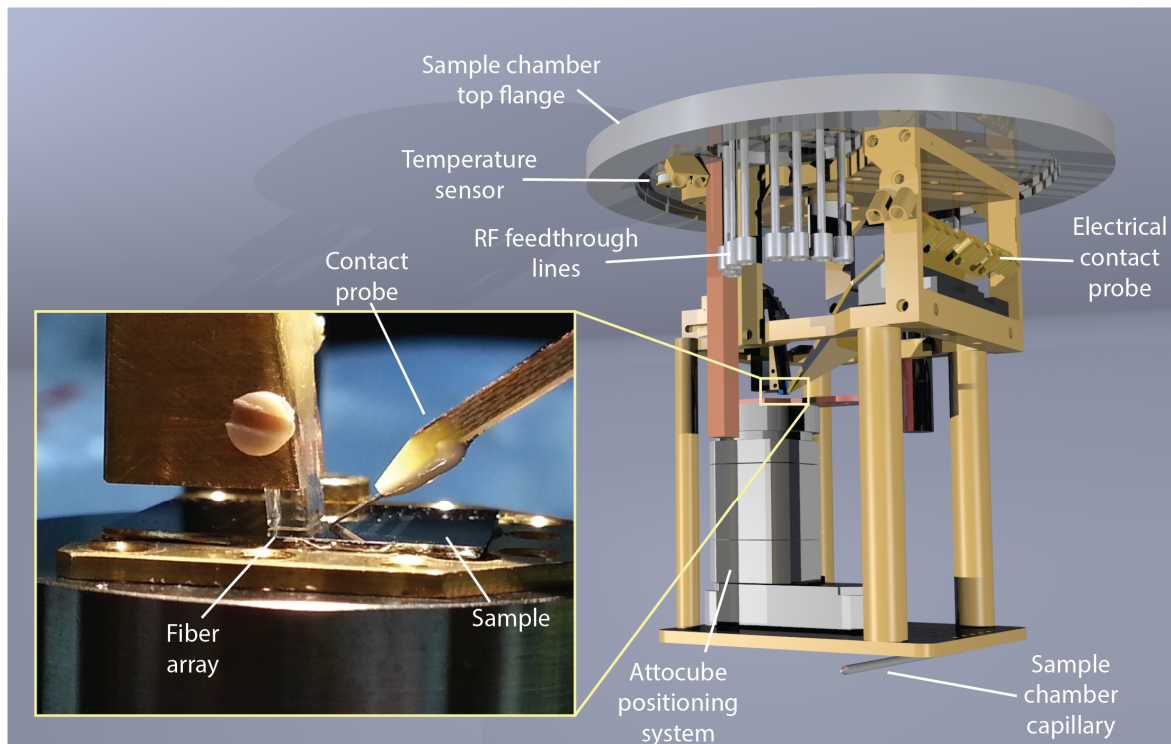


Figure 3.4-2: Rendered illustration of sample holder mounted on sample chamber top flange. Inset: Photograph of optically and electrically connected sample: electrical probe (right) is in physical contact with on-chip contact pads and fiber array (left) is aligned to photonic input and output grating couplers. Note: picture in inset previously published in ref. [193].

3.4.2 ELECTRONIC DRIVING CIRCUIT

The electronic circuit used for all measurements reported in this thesis is depicted in Figure 3.4-3. This electronic setup is similar to the one introduced before in section 2.3.2.2 with a few small additions and changes to accommodate for laboratory-related properties. The bias current to the integrated SNSPD is supplied by a Keithley 2400 source meter operated in voltage mode and a 1 M Ω resistor in series for current stabilization. A low pass filter is added in order to reduce low-frequency current fluctuations. The bias-tee provides additional RF-filtering and connects the circuit to the cryostat's RF line which terminates at the contact probe inside the cryostat's sample chamber. RF signal pulses from the integrated SNSPD are amplified by two low-noise small-signal-amplifiers with +25 dB gain each. The resulting amplified pulses are evaluated using fast electronic read-out equipment.

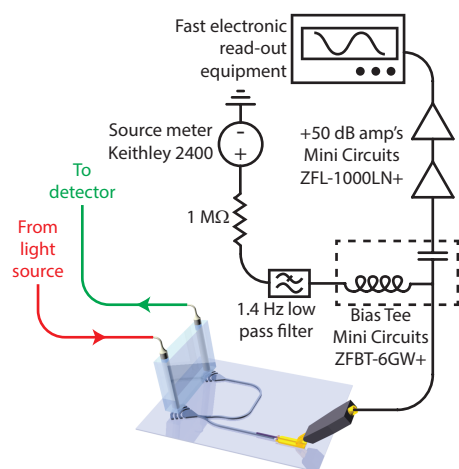


Figure 3.4-3: Electronic driving circuit for SNSPD operation

3.5 INTEGRATED SNSPD CHARACTERIZATION

Numerous detectors with nanowire widths ranging from 60 nm to 200 nm and lengths ranging from 40 μm to 90 μm were fabricated in order to find an optimal geometry for an integrated SNSPD optimized for 1550 nm. Here, the most relevant results where near unity detection efficiency was achieved are presented.

Note: The data and pertinent results presented in this section have been previously published refs. [193]–[195].

3.5.1 INTEGRATED SNSPD OPERATION CONDITIONS

When cooled below their transition temperature, the integrated SNSPDs become operational and are able to detect individual photons. Upon the absorption of a photon, the detectors produce voltage pulses of a specific magnitude which is determined by the applied bias current I_b and the amplifiers' combined gain G . Typical voltage pulse magnitudes range from several tens to a few hundred millivolts depending on the biasing conditions. As the bias current is ultimately limited by the critical current, large critical current values are desirable. A typical voltage signal pulse is shown in Figure 3.5-1.

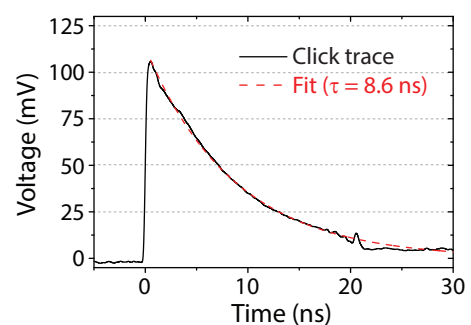


Figure 3.5-1: Typical voltage signal trace measured at 80 nm wide, 4 nm thick wire; depicted trace was averaged 100 times

Since the nanowires' critical current scales with temperature (see Figure 3.5-2), lower operating temperatures are desirable in order to allow for higher critical currents and, by extension, maximize the detection plateau.

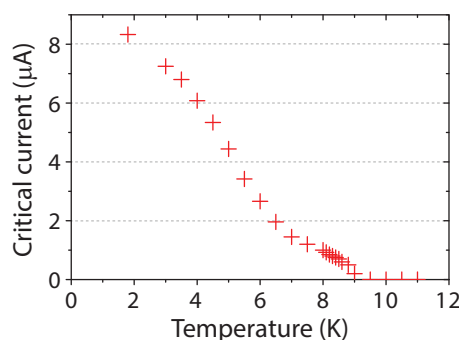


Figure 3.5-2: Critical current vs temperature measured at 80 nm wide, 4 nm thick wire

The evaluation of the signal pulses is performed by fast electronic read-out equipment. This equipment generally triggers on the rising edge of the signal pulse, ideally at the half-maximum level. For measurements with constant bias current this is a straightforward procedure. If the bias current is, however, adjusted during the measurement – as is e.g. the case when measuring the OCDE – careful attention has to be paid to the correct trigger level setting.

3.5.2 ON-CHIP DETECTION EFFICIENCY

3.5.2.1 EXPERIMENTAL SETUP AND MEASUREMENT PROCEDURE

The detection efficiency of a SPD is usually assessed by comparing the detector count rate to a well-calibrated photon flux on the detector (see eqn. 2.1.1-1). In the case of integrated SNSPD OCDE

are of concern, so a precise number of photons must arrive inside the waveguide toward the detector.

In order to achieve this, the optical setup depicted in Figure 3.5-3 is employed. Light from a stable continuous-wave (cw) laser source (New Focus TSL-6600) is separated by a 50:50 fiber splitter. Half of the light is attenuated by two adjustable optical attenuators (HP 8156A) in order to realize the desired photon flux. The other half of the light is guided toward a multi-channel power meter (HP 8163A) where the optical input power is constantly monitored. On the chip, the stream of photons is separated one more time. Half the light is routed toward the detector, the other half toward the output GC where it is coupled out from the chip toward the power meter. The simultaneous measurement of the input and output power enables an accurate determination of the required attenuation to produce a specific photon flux inside the waveguide toward the detector. An explicit mathematical derivation can be found in annex A3. The photon flux is usually set to $\Phi = 10^5 \text{ s}^{-1}$ during the measurement.

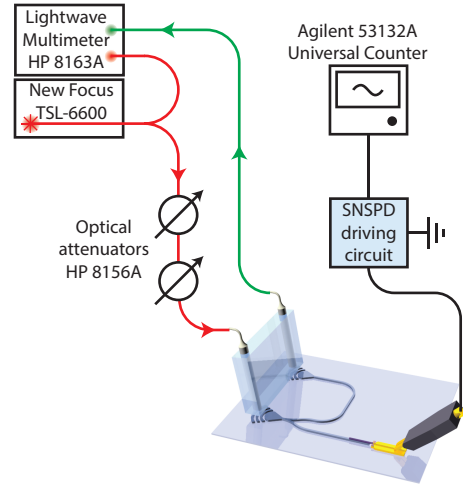


Figure 3.5-3: Experimental setup for OCDE assessment

The integrated SNSPD itself was powered by the previously described biasing and read-out electronics. As a first measurement, the nanowires critical current was determined. In order to record the count rates, a fast electronic counter (Agilent 53132A) is used. The count rates were measured for varying bias currents at a constant photon flux. The starting current was chosen by the onset of a reliable count rate of 1 Hz and was incrementally increased until superconductivity was no longer sustainable. Multiple data points were measured per current value (usually ten) and the integration time was usually set to one second in order to enable count rate measurements of 1 Hz per data point. The dark count rates were measured by the same method without any photons entering the system. For this reason metal shielding caps were used to block ambient light from entering the optical fibers. From the count rate measurements the OCDE can be extracted in analogy to eqn. 2.1.1-1 by

$$\eta_{OCDE} = \frac{R_c - R_{dc}}{\Phi} \quad \text{3.5.2-1}$$

where R_c and R_{dc} denote the registered photon count rate and dark count rate, respectively.

3.5.2.2 RESULTS AND DISCUSSION

The critical current values serve as a general criterion for device quality – the larger the critical current, the higher the quality of the fabricated nanowire. Figure 3.5-4 shows the experimentally obtained critical current values. Using a linear fit a critical current density of $j_c = (35.5 \pm 3.9) \text{ nA/nm}^2$ was extracted from this data. The large variation is attributed to fabrication-related

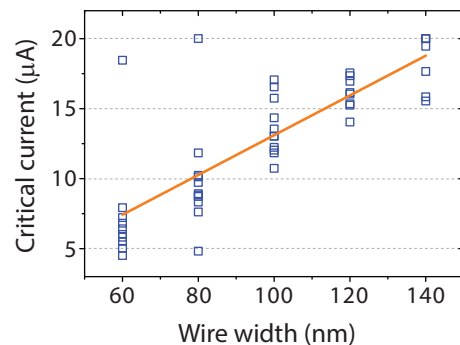


Figure 3.5-4: Experimentally obtained critical current values plotted as a function of wire width

constrictions in the nanowire as well as uncertainties in the wire width and thickness.

Figure 3.5-5 shows on-chip detection efficiency (OCDE) curves of 80 μm long integrated SNSPDs of varying nanowire width extracted from count rate measurements. The data has been normalized with respect to their critical currents. As can be seen, the OCDEs reach generally large values toward the high current end, with a maximum of 84% for the integrated SNSPD with an 80 nm wide wire. The generally high efficiencies are mainly a consequence of the extended absorption length realized by photonic integration.

As the AE is independent of bias-current the curve shape is solely determined by the IQE. All curves – except the magenta curve representing the 140 nm wide wire – exhibit a sigmoidal shape

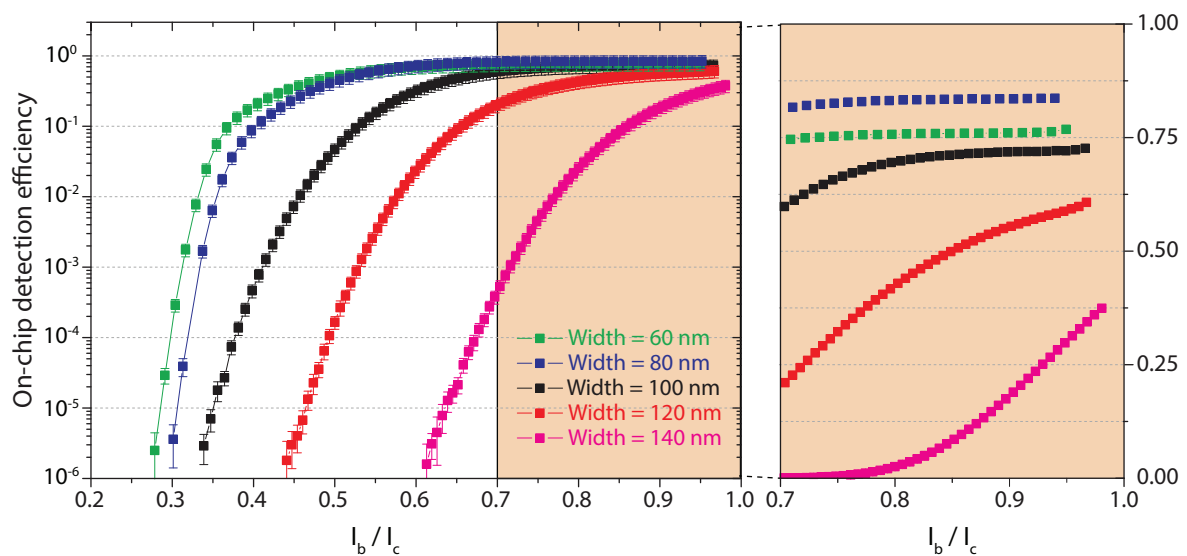


Figure 3.5-5: OCDE as a function of normalized bias current measured at 80 μm long integrated SNSPDs of different nanowire widths plotted on a semi-logarithmic scale (left) and on a linear scale for high bias currents (right). *This data has been previously published in ref. [193].*

with a monotonous increase in OCDE for growing bias currents. The narrower wires exhibit plateau behavior between from 70% of the critical current onward as seen in the linear zoom-in Figure 3.5-5. The wider wires are far from a plateau with the 140 nm wide wire barely reaching its inflection point. The plateau behavior indicates saturation of the IQE.

An interesting cross-over region is presented by the 60 nm and 80 nm wide wires. Up to 80 nm width the OCDE increases as the width is reduced. Yet from 80 nm width down to 60 nm the trend is reversed and the OCDE starts to decline. This can be explained by strong reductions in the AE which the growing IQE is no longer able to compensate. At this turning point the overall OCDE begins to drop despite growing IQE. As the AE continues to decrease for even narrower wires, the trend can be expected to continue also for the OCDE. The trend can, however, be counterbalanced by extensions of the detector length.

Numerical calculations of the absorption efficiency using COMSOL Multiphysics® allow for the calculation of the AE and extraction of the IQE:

Width	60 nm	80 nm	100 nm	120 nm	140 nm
OCDE	76.7%	84.0%	72.6%	60.7%	37.4%
Abs. coefficient	0.08 dB/ μm	0.12 dB/ μm	0.19 dB/ μm	0.27 dB/ μm	0.34 dB/ μm
AE	77.1%	89.0%	97.0%	99.3%	99.8%
IQE	98.7%	94.7%	74.9%	61.2%	37.5%

The IQE follows the expected trend and reaches almost unity in the case of the 60 nm wide nanowire which agrees with the qualitative assessment. The AE clearly increases with wire width. Their combined maximum is found at 80 nm wire width.

3.5.3 DARK COUNTS AND NOISE-EQUIVALENT POWER

The measured dark count curves for 80 μm long SNSPDs with nanowires of different widths are depicted in Figure 3.5-6. As can be seen, up to 60% of the critical current all curves show dark count levels below the 10 Hz mark, in some cases even below 1 Hz. Above this current value, the dark count rates begin to increase slowly until at approximately 90% of the critical current the dark count rate begins to grow exponentially. In order to identify the limitations of this measurement the individual contributions to the dark count rate are analyzed. Below 60% of the critical current, the dark count rate is expected to mostly depend on a weakly current-dependent noise contribution from the utilized electronic equipment. Above 90% of the critical current, the dark count rate diverges as is expected (see section 2.3.3.5). In the range between 60% and 90% of the critical

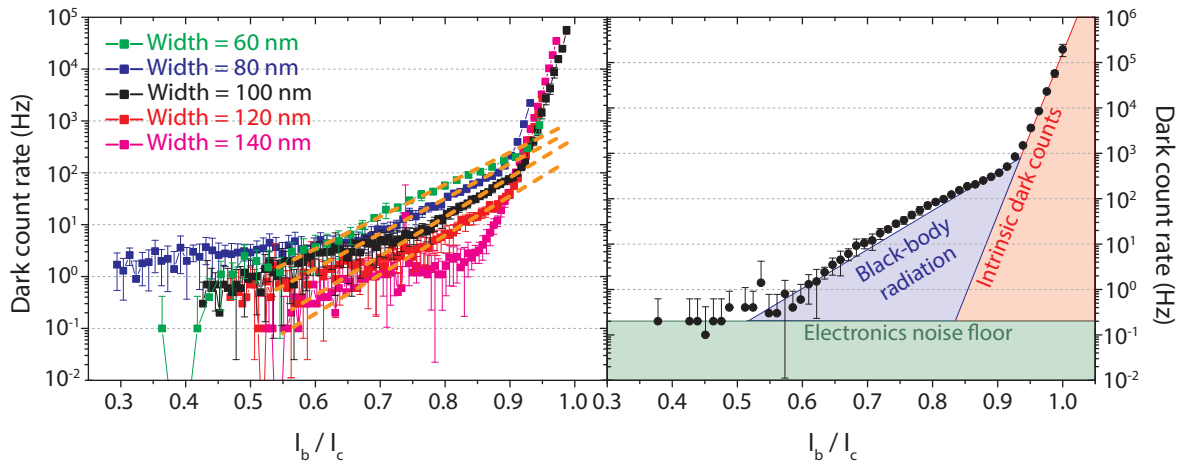


Figure 3.5-6: Left: Dark count rate as a function of normalized bias current measured at 80 μm long integrated SNSPDs; the dashed orange lines indicate the level of black-body photon contribution. Right: Dark count rate as a function of normalized bias current measured at a 60 nm wide, 80 μm long integrated SNSPD; the shaded areas indicate the individual contributions. *This data has been previously published in ref. [193].*

current, a contribution from black-body radiation could be identified as the source (see right graph in Figure 3.5-6). Two checks were performed: the fiber array which is usually positioned on top of the grating couplers for light insertion was moved to a distant position and the measurement was repeated. As no measurable difference was found, it can be concluded that no residual room light entered the photonic circuitry. Secondly, the degree of the contribution of black-body radiation to the dark count curves of SNSPDs with differently wide nanowires was examined. It can be seen from the dashed orange lines in Figure 3.5-6 that the frequency of dark counts in the 60-90% bias current window grows with decreasing wire width. As narrower nanowires exhibit a higher sensitivity to low energy photons, it can be concluded that the unusually high dark count rates in this window are very likely caused by black-body photons.

The well-pronounced detection plateau of the narrow nanowire detectors (shown in Figure 3.5-5) allows for operation at a lower bias current where the dark count contribution is minimized. In order to find the optimal operating point the noise-equivalent power (NEP) is utilized. The NEP can be extracted from the count rate measurements by $NEP = \hbar\omega / \eta_{OCDE} \sqrt{2R_{dc}}$ (see section 2.1.2). In

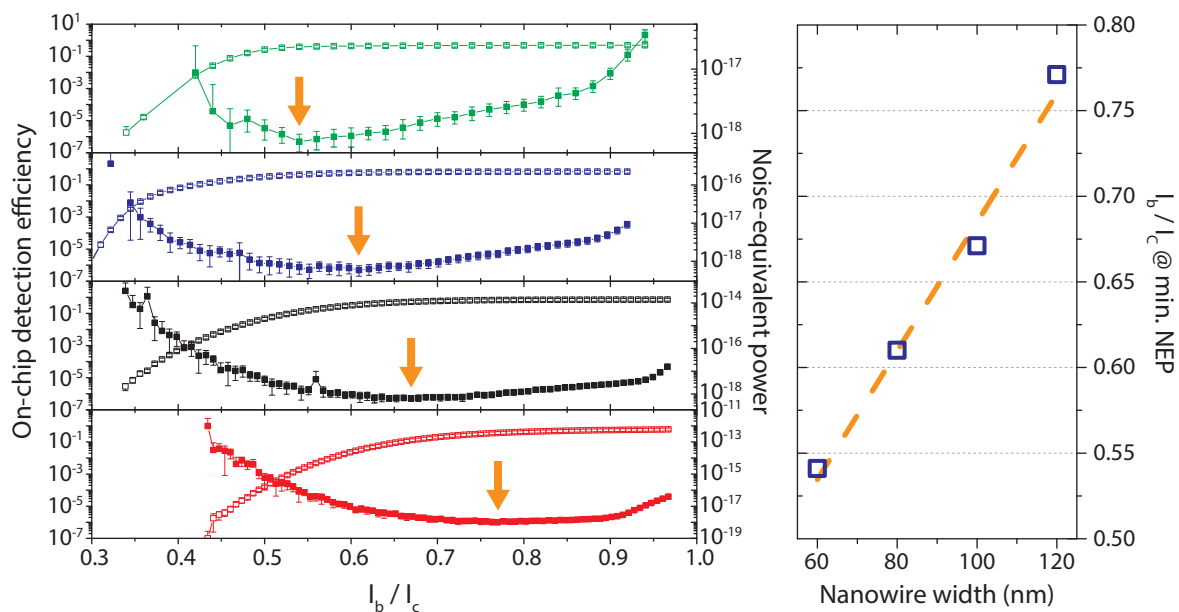


Figure 3.5-7: Left: OCDE (open squares) and NEP (closed squares) for 60 nm wide (green), 80 nm wide (blue), 100 nm wide (black) and 120 nm wide (red) of nanowires as a function of normalized bias current; the arrows indicate the global minima in the NEP. Right: NEP minima plotted vs. bias current. *This data has been previously published in ref. [193].*

Figure 3.5-9 the NEP is depicted alongside the OCDE values from the previous section. The NEP curves show a concave functional dependence on the bias current. Indicated by the orange arrows in the graphs are the global NEP minima. As can be seen in the graphs themselves or in the plot right next to it, the minima positions shift toward smaller normalized current values for narrower wires. This feature in combination with the plateau-like behavior in the OCDE allows for reductions in NEP while maintaining reasonably large OCDE. In the case of the 80 nm wide wire, OCDE above 70% at the 10^{-19} $\text{WHz}^{-1/2}$ level can be obtained at a bias current of 61% of the critical current.

3.5.4 RECOVERY TIME

The recovery time of an integrated SNSPD is evaluated at the electronic output signal. This output signal is a voltage pulse which encompasses contributions from a fast electronic rise and a decay with a slower time constant. The associated time constants were measured using a fast digital sampling oscilloscope (Agilent Infiniium 54855A DSO). The electronic driving circuit and light input layout are identical to the setup used for the determination of the OCDE. Numerous integrated SNSPDs were measured and their rise and decay times extracted. Usually 100 voltage pulse traces are averaged in order to reduce the noise contributions and facilitate fitting.

3.5.4.1 RISE TIME

An exact determination of the detector signal's rise time was limited by the bandwidth of the utilized electronics equipment¹⁷. Measurements with the standard experimental setup as described

¹⁷ 1 GHz bandwidth of MiniCircuits ZFL1000LN+ low-noise amplifier

above consistently yielded values¹⁸ of 270 ± 10 ps (see Figure 3.5-8). While this is certainly within the range of rise times reported in the literature, it is close to the experimental limit. Nevertheless, it can be concluded that all measured rise times exhibit an upper bound of 270 ± 10 ps. Additionally, the right plot in Figure 3.5-8 may suggest that the rise time depends weakly on the wire length with shorter wire showing shorter rise times. A more elaborate examination was precluded by experimental limitations.

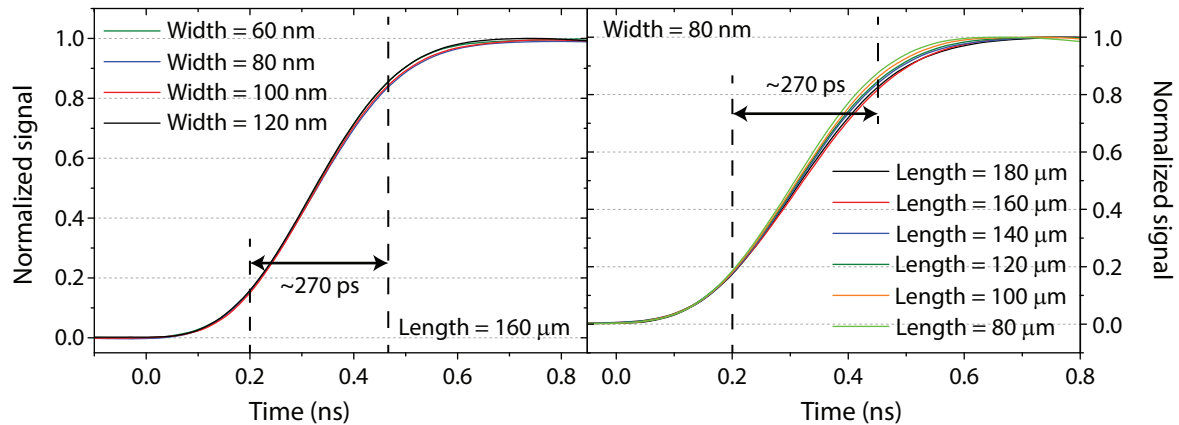


Figure 3.5-8: Rising edge of integrated SNSPD voltage signal trace for varying nanowire width (left) and length (right) showing a rise time of 270 ± 10 ps.

3.5.4.2 DECAY TIME

Several complete voltage signal traces and trend data are shown in Figure 3.5-9. The traces show single exponential decay behavior (orange solid lines in decay plots) which allow for extraction of $1/e$ decay times through appropriate fitting. Usual decay times vary between three and ten nanoseconds depending on the wire geometry. As can be seen from the depicted trend lines (orange dashed lines in the right half of Figure 3.5-9), the decay time of the voltage pulses declines with increasing wire width and grows with increasing wire length. In more detail, the decay time shows reciprocal dependence on the nanowire width and linear dependence on the wire length, i.e. $\tau \propto l/w$. This dependence is reflected by the nanowire's kinetic inductance $L_K \propto l/w$ which indicates that the recovery time of the integrated SNSPD is limited by its kinetic inductance. This also agrees with the theoretical description from section 2.3.2.3.

¹⁸ In analogy to the decay time, the rise time is defined as the duration from $1/e$ to the maximal signal.

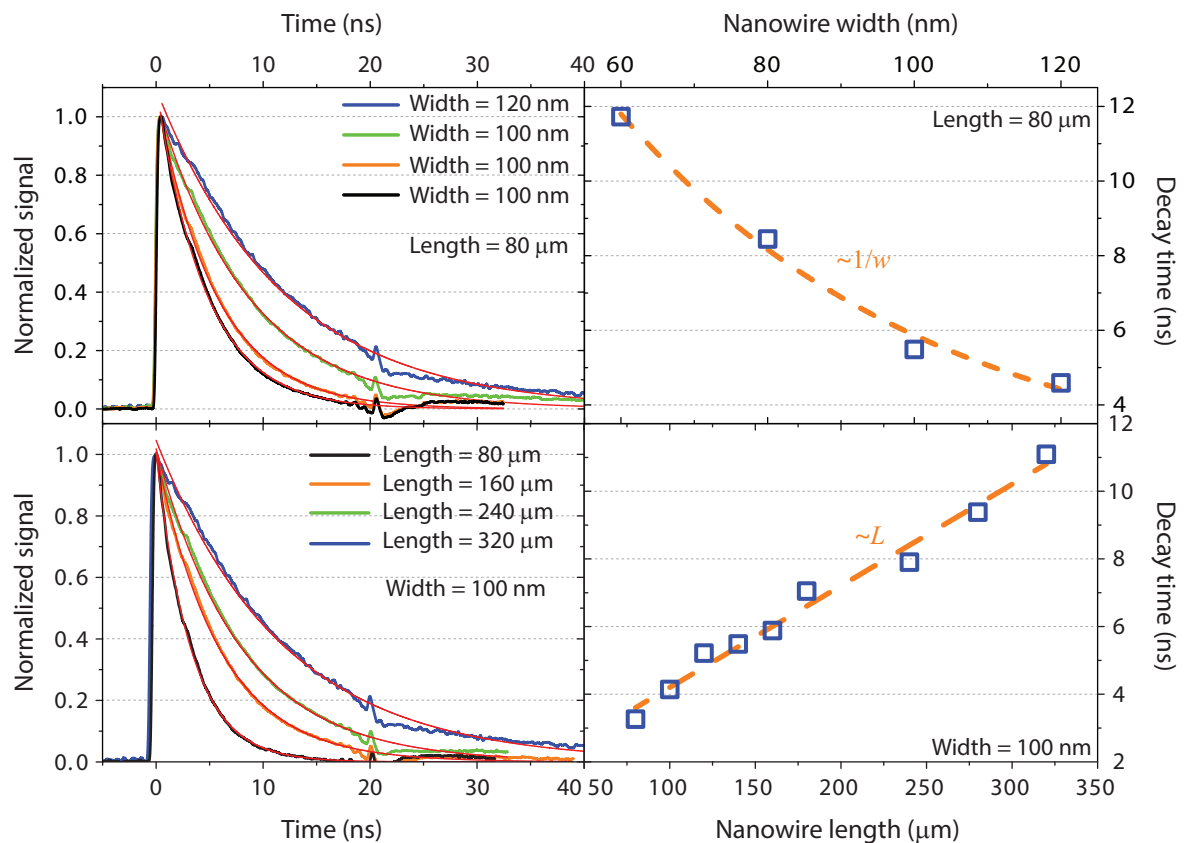


Figure 3.5-9: Left: select decay time curves showing typical $1/e$ -decay times between 3 ns and 11 ns for fixed length (top) and fixed width (bottom); the orange solid lines depict single-exponential fits. Right: decay times plotted in dependence of nanowire width (top) and nanowire length (bottom) including fits (orange dashed line) to indicate functional dependence. *Parts of this data have been previously published in ref. [193].*

COUNT RATE LIMITATION

Commonly, the recovery time – as the name implies – denotes the time in which the detector recovers and is mostly unresponsive. In the case of kinetic inductance-limited integrated SNSPD the bandwidth is thus given by the ratio of nanowire length and width. In the case of a 100 nm wide, 40 μm long integrated SNSPD the recovery is approximately 3 ns and the bandwidth 333 MHz (assuming the usual 4 nm film thickness). The kinetic inductance, however, merely limits the return of the supercurrent into the nanowire and not the recovery of superconductivity. The latter is mostly determined by the phonon escape time which is usually less than 1 ns [167], [196].

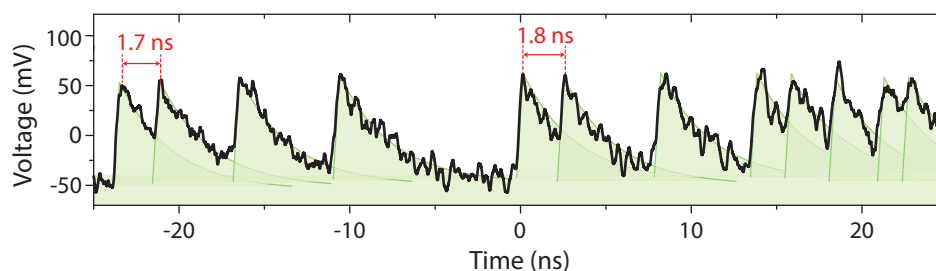


Figure 3.5-10: Oscilloscope trace of a 70 μm long, 80 nm wide integrated SNSPD biased at 4.7 μA (65% of I_c) showing incomplete supercurrent recovery for subsequent detection events. Overlaid in green are the decay lines associated with the recovery of superconductivity set by the kinetic inductance.

Upon closer examination it is found that integrated SNSPDs are responsive even during the time of supercurrent recovery. The voltage trace depicted in Figure 3.5-10 shows that the detector is fully capable of registering photons even when the previous voltage pulse has not fully decayed. This directly implies that higher maximal count rates are possible than the recovery time would suggest. In detail, the depicted voltage trace contains time intervals as short as 1.7 ns between subsequent pulses, which translates into a maximally possible count rate of 588 MHz. This is in contrast to 333 MHz bandwidth set by the kinetic inductance-limited recovery time of 3 ns. This finding therefore suggests that the kinetic inductance is not the ultimate bandwidth limitation. An operational regime in which much higher photon count rates can be achieved is possible if the condition for complete voltage pulse decay is relaxed.

In the proposed mode of operation trigger reliability becomes a challenge. The trigger window is usually determined by the rising edge of the voltage pulse. For incomplete decay of the preceding pulse, the rising edge's magnitude is partially masked and thus substantially reduced. For higher bandwidth, the trigger window reduces at a geometric rate. Additionally, thermal build-up in the substrate causes superconductivity to break down at higher count rates. In this case, the bias current had to be reduced to allow for higher photon fluxes (65% of I_c at 5×10^8 photons per second) in order to sustain superconductivity. The reduction in bias current directly decreases the OCDE such that the high bandwidth potentially becomes overshadowed by lower efficiency. At the reported configuration it was still possible to record count rates of 225 MHz which indicates a moderate OCDE of 45%. Unfortunately, at the time this thesis is written, a more detailed investigation is precluded as the read-out equipment (Agilent 53132A) is limited to 225 MHz and additional noise on the already small rising edge makes reliable triggering hardly possible. Nevertheless, this finding indicates that high bandwidth single-photon detection might be possible using integrated SNSPDs.

3.5.5 TIMING JITTER

3.5.5.1 EXPERIMENTAL SETUP AND MEASUREMENT PROCEDURE

The timing jitter of a SPD represents the temporal variation in the generation of the electronic output signal relative to the time of photon absorption. In order to determine the timing jitter experimentally, the measurement setup depicted in Figure 3.5-11 is used. A picosecond laser (PriTel FFL-40M for 1550 nm / ALS PiLas PiL044X for 440 nm) is employed to send a short (1-2 ps) reference signal to the integrated SNSPD and a fast photoreceiver (New Focus 1611). Both detectors generate electrical pulses which are routed toward a fast digital sampling oscilloscope (Agilent Infiniium 54855A DSO) where they are used as start and stop triggers in order to produce a histogram showing the relative arrival times of the electronic pulses. The histogram's full width at half-maximum (FWHM) represents the timing jitter. As the histogram will be a convolution of the timing jitters of all involved instruments, it is important that the timing jitters of the laser, the photoreceiver and the oscilloscope be significantly smaller

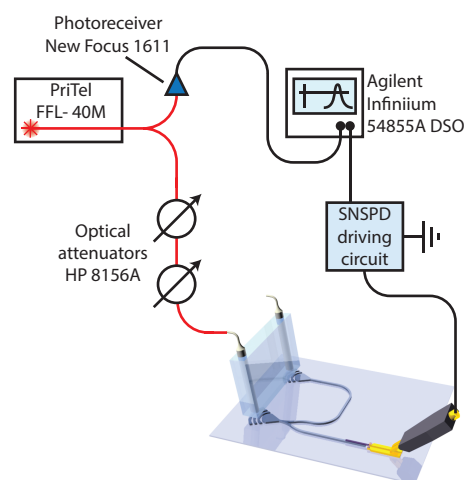


Figure 3.5-11: Experimental setup for timing jitter measurement

than the jitter which is to be measured. The utilized instruments' timing jitters are all smaller than 1 ps.

3.5.5.2 RESULTS AND DISCUSSION

The timing jitter values of numerous devices have been measured throughout this thesis. Here, the salient results will be reviewed. A typical timing jitter histogram is depicted in the left part of Figure 3.5-12. The data was acquired at a SNSPD designed for the visible (detector length 80 μm , stripe width 80 nm, gap 100 nm) and a FWHM timing jitter of 41 ps is extracted from a Gaussian fit. The timing jitter was found to depend on the bias conditions with the jitter decreasing at larger bias currents until it saturates at a specific value (see top right graph in Figure 3.5-12). This trend can be explained by the growing electronic noise contribution for low bias currents. The detector's signal voltage pulse magnitude depends on the bias current (see bottom right graph in Figure 3.5-12). Its exact magnitude is determined by the applied bias current and the amplifier gain. For small bias currents, and therefore small voltage signals, the rising edge is relatively shallow compared to larger voltage signals closer to the critical current (see bottom left graph in Figure 3.5-12). In the case of shallow rising edges at small bias currents, electronic noise contributions are able to introduce additional temporal uncertainties on the rising edge and thereby increase the timing jitter. At larger bias currents, the significance of these contributions reduces due to the steeper rising edge. For

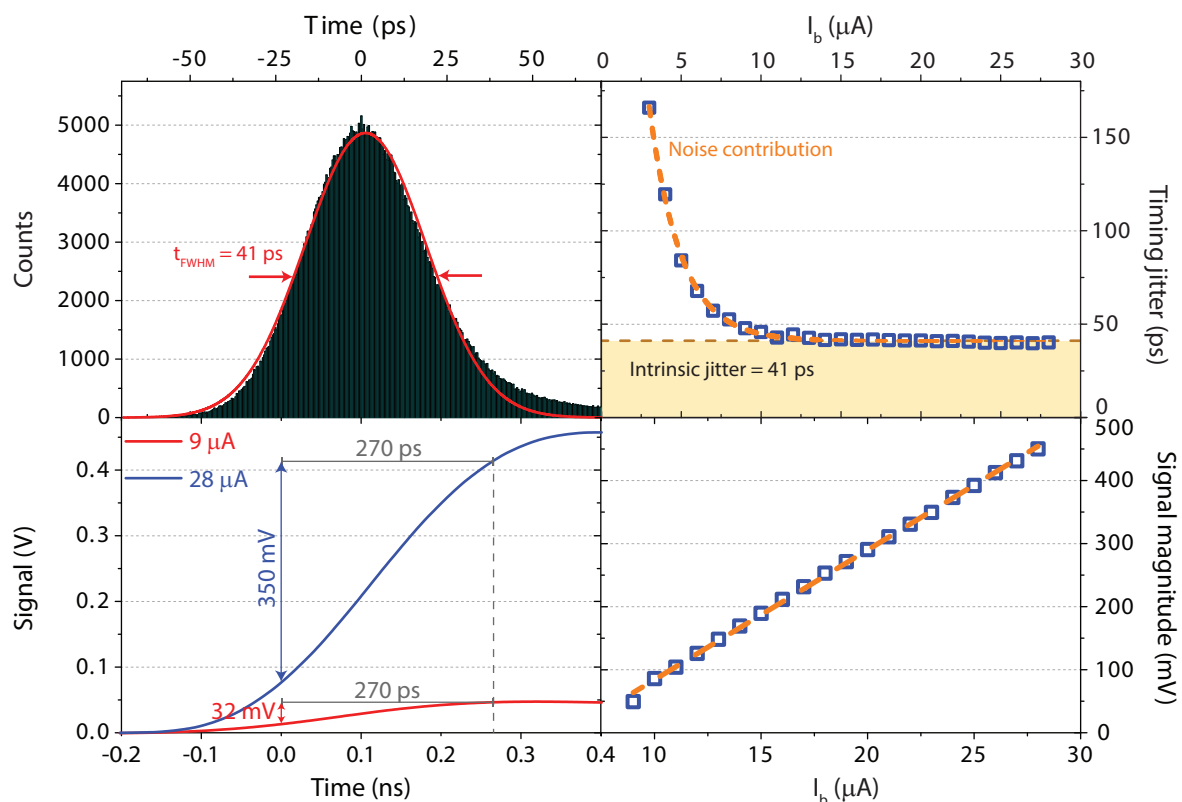


Figure 3.5-12: Top left: arrival time histogram measured at a 80 μm long, 80 nm wide integrated SNSPD at 440 nm including Gaussian fit which yields a 41 ps FWHM timing jitter. Top right: jitter values extracted from histogram data measured at varying bias currents. Bottom left: Rising edge of voltage signal for 9 μA and 28 μA bias current showing shallow and steep rise. Bottom right: Wi-SNSPD voltage pulse magnitude in dependence of bias current; the dashed orange line is obtained theoretically by assuming a $R_L = 50 \Omega$ load resistance and 50 dB amplifier gain. *This data is part of a publication which is currently in preparation (authors: O. Kahl, V. Kovalyuk, S. Ferrari, G. Gol'tsman, W. Pernice).*

sufficiently steep rising edges, i.e. at large bias currents, the noise contributions become negligibly small. This point is reached at a bias current of $10\ \mu\text{A}$ where the voltage pulse magnitude is $80\ \text{mV}$. Two separate contributions to the timing jitter can therefore be distinguished: an intrinsic timing jitter which is determined by the superconductivity breakdown dynamics and a noise-related addition which introduces fluctuations in the signal pulse's rising edge.

In integrated SNSPDs where the bias current is limited by small critical current values the jitter can suffer from significant noise contributions. As the critical current is, furthermore, limited by the wire cross-section, under certain circumstances a dependence of the jitter on the nanowire width can be measured. Such an example is shown in Figure 3.5-1.

Figure 3.5-1 shows the histogram data acquired at $80\ \mu\text{m}$ long SNSPDs with differently wide nanowires at $1550\ \text{nm}$. The bias current was set to 95% of the critical current in all SNSPDs. A FWHM timing jitter value of $35\ \text{ps}$ is reached in the $120\ \text{nm}$ wide nanowire whereas the jitter values in the narrower nanowires gradually increase up to $91\ \text{ps}$ in the $60\ \text{nm}$ wide wire. Since all data was collected at 95% of the SNSPDs' respective critical current, the signal pulses were differently affected by the electronic noise. The critical current values of the SNSPDs were $6.82\ \mu\text{A}$ ($60\ \text{nm}$), $8.33\ \mu\text{A}$ ($80\ \text{nm}$), $10.74\ \mu\text{A}$ ($100\ \text{nm}$), and $14.05\ \mu\text{A}$ ($120\ \text{nm}$). Using the timing jitter vs bias current curve depicted in the top right graph in Figure 3.5-12 as a reference it is likely that the obtained timing jitter values of the $1550\ \text{nm}$ SNSPDs are obstructed by electronic noise. This is mainly due to the low critical current values which disallow operation in the noise-free jitter regime. Ultimately, the data presented above emphasizes the need for high critical current values in integrated SNSPDs.

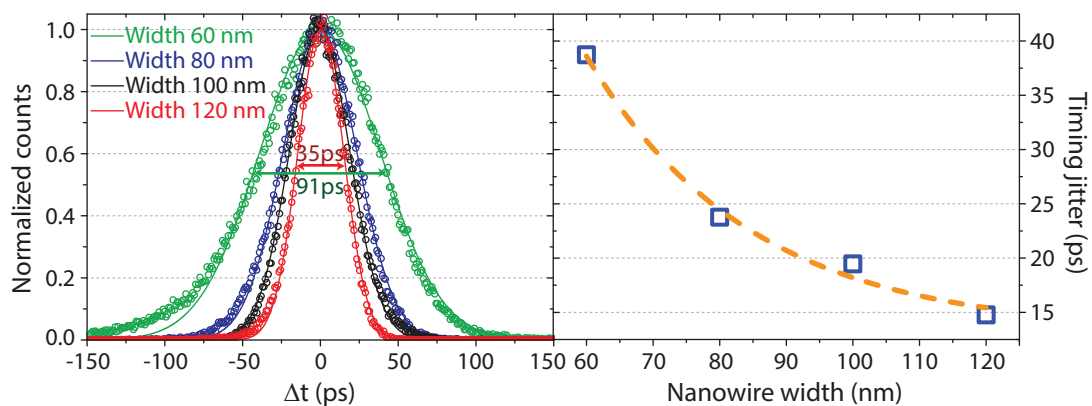


Figure 3.5-1: Left: histogram data measured at $80\ \mu\text{m}$ long SNSPDs with nanowires of different widths (open circles) and Gaussian fits (solid lines). Right: FWHM timing jitter values extracted from the Gaussian fits plotted as a function of nanowire width. The orange line has been inserted to guide the eye. *This data has been previously published in ref. [193].*

3.6 CONCLUDING REMARKS ON THE DETECTOR CHARACTERIZATION

As mentioned at the beginning of this thesis, waveguide integration of superconducting nanowire-based detectors is a new development with extraordinary potential for on-chip quantum optics. Previously, several designs have been realized and the potential to enhance the detection efficiency through near-field coupling demonstrated on several platforms. In this chapter, the implementation

of a design was demonstrated, which reaches near-unity on-chip detection efficiency in the NIR at 1550 nm combined with extremely high temporal accuracy. The design was optimized by experimental assessment of the geometrical parameters. In particular it was found that the internal quantum efficiency approaches unity at a nanowire width of 80 nm. The associated early onset of the detection plateau was shown to allow for operation at bias currents far below the critical current thus allowing for a desirable combination of high detection efficiency and minimized dark count influence. This is a significant improvement over previous implementations of integrated SNSPDs whose detection efficiency did not reach saturation.

Moreover, it could be shown that the SNSPD's maximal count rate is not limited by its decay time. By operating in a low bias current regime, it was found that voltage signal pulses can occur even if the preceding signal has not fully decayed. This is in contrast to the currently established opinion which assumes limitation by the nanowire's kinetic inductance [106]. Future research in this area could lead the way to the realization of gigahertz single-photon counting.

Limitations of the timing jitter were identified. In the low bias current regime, the timing jitter was found to increase due to a noise-related addition to the temporal uncertainty of the voltage pulse's rising edge. The contributions reduce in the high-bias regime and eventually disappear at which point the timing jitter is determined by the superconductivity breakdown dynamics. Limitations of the bias current by low critical current values possibly lead to increased jitter values which emphasize the necessity of large critical current values. Improvements in the fabrication are needed to ensure consistently high critical current densities.

Ultimately, a SPD for the NIR regime was realized, which combines high quality levels in all key detection criteria – detection efficiency, timing accuracy, and bandwidth. These characteristics are attractive for quantum-based technologies as well as classical applications with high demands on detection performance. Single-emitter imaging and fluorescence lifetime measurements benefit from the detector's timing accuracy and high efficiency. In combination with the ability to fabricate countless integrated SNSPDs on a single chip, very attractive device combinations become possible. In chapter 5, one such implementation will be demonstrated which enables the simultaneous temporal and spectral analysis of a fluorescent sample.

4 SINGLE AND MULTI-PHOTON DETECTION

In general, integrated SNSPDs are unable to discriminate photon numbers. They only distinguish between the presence and absence of one or many photons. Its internal response, however, varies with incident photon number and can be exploited to make the detector insensitive to a specific photon number, but sensitive to any larger number. A statistical method known as quantum detector tomography (QDT) is used to characterize the detector's response on a fundamental level and extract its IQE. The technique requires a basic understanding of quantum optics. The chapter will therefore introduce a formal concept of the photon and photon states. Subsequently, the involved photon statistics will be reviewed and the QDT technique will be described. A QDT model specifically for integrated SNSPDs is developed and employed to assess the response of the previously introduced detectors.

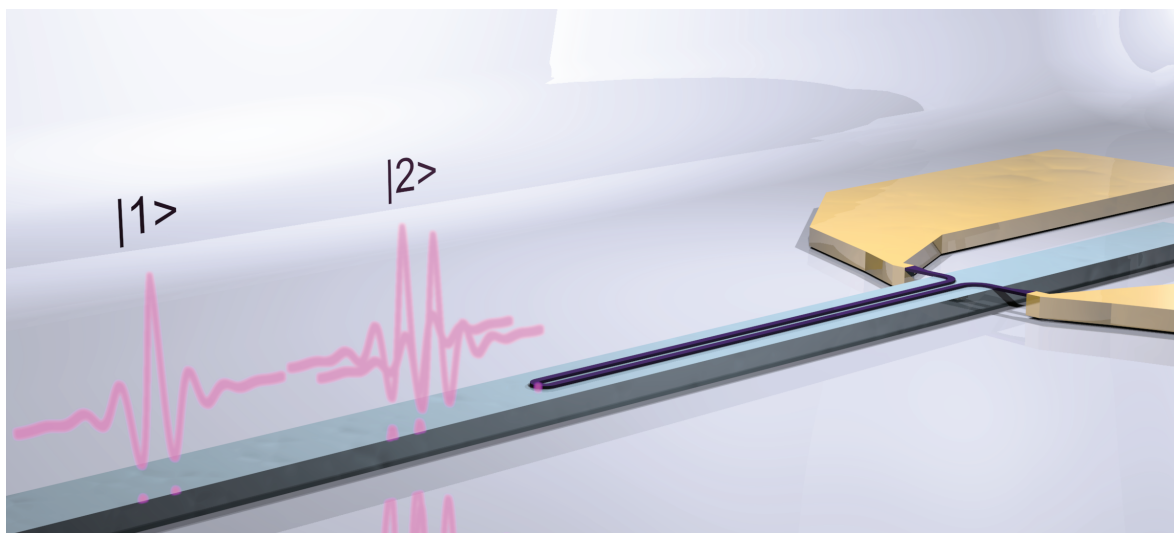


Illustration of different photon states incident on waveguide-integrated SNSPD

4.1 DETECTION REGIMES

In the preceding chapters it was thus far blindly assumed that the voltage pulse which follows some perturbation in the superconducting state was created by a single photon. This was, however, not explicitly tested. The high detection efficiency of almost 90% is a strong indication for single-

photon detection capability, but it is by no means a robust study. In chapter 2 it was argued that local breakdown of superconductivity requires a minimum amount of energy which is supplied in combination by the bias current and the photon. The photon energy might, however, also be supplied by multiple photons instead of a single one. This implicitly gives rise to multiple more detection regimes in which not one, but multiple photons trigger the detector. As we will see it is possible to carefully tune the bias conditions and geometry of an integrated SNSPD in order to make it responsive only to a minimum number of photons. This might be interesting for advanced quantum optical applications where the detector must respond to a particular set of exotic photon states. The details of such a scenario will be elaborated in the following.

Furthermore, a statistical model is developed which allows for the extraction of internal quantum efficiency values for the different detection regimes. These results enable the fine adjustment of the detector's biasing conditions in order to selectively tune the sensitivity toward one particular photon number.

4.2 QUANTUM OPTICAL METHODOLOGY

The focus of this thesis is a detector which is capable of detecting individual photons. Yet, despite the inherently quantized nature of what we are trying to detect no advanced quantum mechanical treatment was necessary. We implicitly assumed the photon was an energy packet of size $\hbar\omega$, but ignored any implications this might have beyond energy quantization. No explicit quantum mechanical treatment was required. For many optical properties and mechanisms – like SPDs or e.g. the laser – such a *semi-classical approach* in which matter is quantized, but the fields maintain their wave character is perfectly sufficient. Other optical phenomena, however, mandate a *complete quantum mechanical treatment*, where light and matter are both quantized. In this chapter, we will introduce a few basic concepts of the purely quantum mechanical picture. This is necessary in order to understand and use the QDT technique which was mentioned in the opening lines of this chapter. In short, QDT utilizes knowledge about a probing photon state in order to characterize an unknown detector parameter [197], [198]. In this section we will, therefore, review the basics of the quantum states of light, their statistics, and eventually the QDT technique.

4.2.1 LIGHT QUANTIZATION AND PHOTON STATES

The notion that light is fundamentally composed of discrete energy packets was originally introduced by Planck's quantum hypothesis [1] and Einstein's description of the photoelectric effect [2]. In a quantum mechanical context, this is reflected in the energy eigenvalue problem given by the time-independent Schrödinger equation $\hat{\mathcal{H}}|\psi\rangle = E|\psi\rangle$. The quantized Hamiltonian $\hat{\mathcal{H}}$ is obtained from the classical field Hamiltonian by imposing appropriate quantization conditions. This is achieved by interpreting the electric and magnetic field amplitudes as conjugate canonical coordinates similar to position and momentum [199]–[203]. The resulting quantum mechanical Hamiltonian for electromagnetic fields is thus given by

$$\hat{\mathcal{H}} = \hbar \sum_j \omega_j \left(\hat{a}_j^\dagger \hat{a}_j + \frac{1}{2} \right) \quad 4.2.1-1$$

which is expressed here in its most common canonical basis using the *creation operator* \hat{a}_j^\dagger and the *annihilation operator* \hat{a}_j . The different j represent the individual Fourier modes¹⁹. It is important to note that this result is formally identical to the Hamiltonian of the quantized harmonic oscillator. Therefore, each field mode is effectively the radiative equivalent of the classical harmonic oscillator [19], [203].

The eigenstates $|n\rangle$ of the single-mode Hamiltonian are commonly referred to as *Fock states* or *Number states* and constitute the most basic states in the quantum theory of light. They form a complete, orthonormal set for a single mode and, most importantly, all other varieties of light can be decomposed into Fock states. Mathematically they are easily manipulated, experimentally, however, they are more complicated to generate than other photon states [199].

The Fock states' energy eigenvalues are given by $E_n = \hbar\omega(n + 1/2)$ where n represents the number of excited photons. In this context, it is important to realize that photons are nothing more than energy quanta. The tempting notion of photons as the localized, mass-less equivalent to corpuscular particles like e.g. the electron are false and must be dismissed [200], [201]. The photon is essentially 'spread out' over its entire mode volume.

Additionally, the photon number is not a conserved quantity as in the case of corpuscular particles; photons have the ability to be created and destroyed. In the quantum mechanical formalism this is achieved through the ladder operators \hat{a}^\dagger and \hat{a} which account for the creation and annihilation of a photon. Through repeated application of \hat{a}^\dagger to the vacuum state $|0\rangle$, it is thus possible to construct any Fock state from the vacuum through $|n\rangle = (\hat{a}^\dagger)^n (n!)^{-1/2} |0\rangle$.

As mentioned above, Fock states form the basis also for other photon states. In general, the state vector of any single-mode photon state can be decomposed into a superposition in the Fock base. One particular superposition is of special interest – the *coherent state*. This photon state has particular properties which lend themselves perfectly for the aforementioned QDT technique.

Coherent states are from a practical application perspective the most interesting linear superpositions of single-mode photon states. They are the quantum-mechanical counterpart to the classical, monochromatic electromagnetic wave of constant amplitude and fixed phase [199], [200], [204]. Such states can be easily produced by a laser operated well above threshold and are, therefore, the most readily available photon states in research environments.

The coherent state is commonly denoted as $|\alpha\rangle$ and, formally, it is the eigenstate of the annihilation operator, i.e. $\hat{a}|\alpha\rangle = \alpha|\alpha\rangle$. The eigenvalue α is a complex, scalar parameter which determines the *average* number of photons contained in the state $|\alpha\rangle$, i.e. $\langle\alpha|\hat{n}|\alpha\rangle = |\alpha|^2$. The coherent states form an overcomplete set of the harmonic oscillator states and are thus non-orthogonal, i.e. $\langle\alpha|\alpha'\rangle \neq 0$. It is, however, worth noting that for $|\alpha - \alpha'| \gg 1$ they approach orthogonality. The states are naturally normalized such that the probabilities sum up to unity. In the Fock base, the coherent state can be expressed as [199]–[201]:

$$|\alpha\rangle = e^{-\frac{|\alpha|^2}{2}} \sum_{n=0}^{\infty} \frac{\alpha^n}{\sqrt{n!}} |n\rangle \quad \mathbf{4.2.1-2}$$

¹⁹ The absence of subscripts implies the excitation of only a single mode.

Although the coherent state possesses other interesting characteristics, most notably minimal uncertainty in its quadrature coordinates regardless of mean photon number $|\alpha|^2$, the most relevant aspect in the scope of this thesis pertains to its photon number statistics which will be elaborated in the following section.

4.2.2 PHOTON NUMBER STATISTICS

From an experimental point of view, different photon states can only be distinguished by their statistics. In turn, knowing the statistical distribution of photons in a particular photon state can help to draw conclusions about certain detector properties. This is the premise for QDT.

Fock states, or Number states, by virtue of its definition and name, imply a well-defined number of photons with zero uncertainty. Quantitatively, this is implicit in its normalization, i.e. the probability of finding n photons in the state $|n\rangle$ is always unity, since $P(n) = |\langle n|n\rangle|^2 = 1$. Its statistical spread about the mean thus vanishes²⁰. This characteristic can be illustrated more intuitively in an experimental context: a hypothetical light source which is calibrated to emit only single-mode Fock states, e.g. the state $|1\rangle$, will *only* emit energy packets of one particular magnitude, namely $\hbar\omega$, without any deviation from it.

This is to be contrasted from other photon states which are composed of multiple Fock states. In particular, the coherent state $|\alpha\rangle$ exhibits a well-defined statistical spread: the probability of finding the Fock state $|n\rangle$ in a single-mode coherent state $|\alpha\rangle$ obeys *Poisson statistics*. This follows from the definition of the coherent state in eqn. 4.2.1-2 since

$$P(n) = |\langle n|\alpha\rangle|^2 = e^{-|\alpha|^2} \frac{|\alpha|^{2n}}{n!} = e^{-\langle\hat{n}\rangle} \frac{\langle\hat{n}\rangle^n}{n!} \quad 4.2.2-1$$

where the relation for the average number of photons $\langle\hat{n}\rangle = \langle\alpha|\hat{n}|\alpha\rangle = |\alpha|^2$ is substituted. The photon number variance of the coherent state is subsequently $(\Delta n)^2 = \langle\alpha|\hat{n}^2|\alpha\rangle - \langle\alpha|\hat{n}|\alpha\rangle^2 = \langle\hat{n}\rangle = |\alpha|^2$. In comparison to the experimental illustration used above, one can imagine a hypothetical light source which is calibrated to emit one particular coherent photon state $|\alpha\rangle$: this source will *on average* emit energy packets of magnitude $|\alpha|^2\hbar\omega$ with a spread of $|\alpha|^2\hbar\omega$ around it; the chance of finding an energy packet of the specific magnitude $n\hbar\omega$, i.e. exactly n photons, is given by the Poisson distribution in eqn. 4.2.2-1.

It is worth noting that the photon number statistics refer only to the time-independent state composition and are not to be confused with temporal correlations of individual photons in a light beam. The latter concerns another important statistical aspect of the quantum nature of light which is commonly referred to as *photon bunching* [205].

4.2.3 QUANTUM DETECTOR TOMOGRAPHY BASICS

QDT is an advanced statistical method used to determine an unknown detector response using a well-known input state [197], [198]. In simple terms, we could ask the following question: given a Fock state $|n\rangle$ on the detector input, what is the probability $P(n)$ that the detector will register this

²⁰ The same result can be obtained by considering the state's variance, i.e. $(\Delta n)^2 = \langle n|\hat{n}^2|n\rangle - \langle n|\hat{n}|n\rangle^2 = 0$.

state. In theory, sending the state $|n\rangle$ onto the detector repeatedly will yield $P(n)$ for sufficiently many repetitions. The experimental predicament is that specific Fock states $|n\rangle$ are far from readily available; the vast majority of optical sources produce photon states with a non-zero statistical spread in photon number $(\Delta n)^2 = \langle \hat{n}^2 \rangle - \langle \hat{n} \rangle^2 > 0$. Furthermore, the detector might respond differently to one and the same input state. This is possible in the case of e.g. a multi-element detector which produces output pulses of variable magnitude depending on how many elements were covered by the input state.

QDT resolves this issue by adopting a statistical approach. Instead of using a pure Fock state with zero spread, one can utilize some other state with variable photon number, but well known spread. The coherent state $|\alpha\rangle$ is a prime candidate in QDT for two reasons: on the one hand, coherent states are readily produced by a laser operated well above threshold; on the other hand, a coherent state remains coherent when attenuated [19], [199], [201]. The latter allows us to experimentally produce coherent states of varying average photon number $|\alpha|^2$ using one and the same laser.

4.2.3.1 MATHEMATICAL FORMULATION

Measurements in quantum mechanics are usually described by an operator set of possible outcomes $\{\pi_n\}$ which in its most general form is complete and positive semi-definite [15], [197], [198]. Assuming our detector is a black box about which we have absolutely no information, then the task of QDT is to determine the operator set $\{\pi_n\}$. To this end, we prepare the system in a state ρ and perform a measurement. The probability $p_{\rho,n}$ of obtaining the result n is then given by

$$p_{\rho,n} = \text{Tr}(\rho\pi_n) \quad 4.2.3-1$$

Because of the aforementioned reasons of experimental ease, the state which we will prepare is a coherent state $|\alpha\rangle$ such that $\rho = |\alpha\rangle\langle\alpha|$. Due to the statistical nature of the coherent state, we have to perform the measurement D times, such that $p_{\alpha_i,n} = \text{Tr}(|\alpha_i\rangle\langle\alpha_i|\pi_n)$ with $i = 1, \dots, D$. Unfortunately, we do not know the $\{\pi_n\}$ *a priori*, so we need to choose a generic expression for π_n in the Fock basis and make a few simplifying assumptions. For instance, we are certain that our integrated SNSPDs are insensitive to the phase of the incident photon, which enables us to neglect potential off-diagonal elements [198]. We can also state with certainty that the detectors produce only one kind of output irrespective of photon number, which allows us to drop the subscript n . With those simplifications we can make the generic ansatz

$$\pi = \sum_k c_k |k\rangle\langle k| \quad 4.2.3-2$$

Remembering the definition of the coherent state $|\alpha\rangle$ from eqn. 4.2.1-2 we can thus rewrite the outcome probability of a measurement as

$$p_{\alpha_i} = e^{-|\alpha_i|^2} \sum_k \frac{|\alpha_i|^{2k}}{k!} c_k \quad 4.2.3-3$$

This result represents a weighted sum of mutually independent Poissonian distributions of identical *average* photon number $|\alpha_i|^2$ and varying *actual* photon number k . The weighting factors c_k depend on the actual photon number k and can thus be interpreted as detector responsivity to a photon state which contains exactly k photons. Effectively, this represents a refined version of the

detector's internal quantum efficiency (IQE), separated into individual contributions from the simultaneous detection of k photons. Various advanced techniques can be found in literature to extract the coefficients c_k mathematically [206]. We are, however, not interested in the full spectrum of the detector, but only its small-photon-number end. In this range, we are able to see how many photons are required to cause superconductivity breakdown.

4.2.3.2 QDT IN INTEGRATED SNSPDS

Established QDT models are mostly concerned with normal incidence detection [47], [207], [208] which is based on a single, infinitely thin detection plane. These models are not directly compatible with the integrated design used in this thesis. As a consequence, a new model based on the formalism suggested by Elezov et al. [207] was devised for this thesis. In order to account for the extended absorption length of the nanowire the stripes are divided into small squares with edge length equal to the stripe width w (see Figure 4.2-1). The marginal contribution of the tip is neglected.

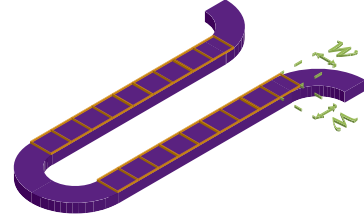


Figure 4.2-1: Nanowire sectioning required for waveguide-integrated QDT model

With this meshed nanowire in mind, let us assume a coherent state $|\alpha_0\rangle$ arrives at the nanowire. Its expected photon number is initially $\langle \alpha_0 | \hat{n} | \alpha_0 \rangle = |\alpha_0|^2$. This expectation value, however, changes along the nanowire due to the wire's finite absorptivity. The number which is expected to arrive at the j -th square has thus reduced to

$$|\alpha_j|^2 = |\alpha_0|^2 \exp(-ajw)[1 - \exp(-aw)] \quad 4.2.3-4$$

where a denotes the absorption coefficient along the nanowire stripe. Given those $|\alpha_j|^2$ expected photons in the j -th square, we next ask, what is the chance that the absorption of exactly k photons inside the j -th square leads to a detection event? The answer is given by the k -th term of the sum in eqn. 4.2.3-3 considering, however, that the expected photon number is reduced to $|\alpha_j|^2$:

$$p_j^{(k)} = e^{-|\alpha_j|^2} \frac{|\alpha_j|^{2k}}{k!} c_k \quad 4.2.3-5$$

Conversely, the probability of *not* absorbing k photons in any other square is given by

$$\zeta_j^{(k)} = \prod_{q=0, q \neq j}^{L/w} (1 - p_j^{(k)}) \quad 4.2.3-6$$

where L denotes the length of the stripe. Ultimately, the probability that the absorption of k photons leads to a detection event given a coherent input state $|\alpha\rangle$ is given by

$$P_\alpha^{(k)} = 2 \sum_j p_j^{(k)} \zeta_j^{(k)} \quad 4.2.3-7$$

The factor 2 accounts for the fact that the nanowire is composed of two stripes. This model will serve as the basis for the analysis of the data obtained in this chapter. In an experimental context,

the k terms are, in general, not separately accessible. Often one term dominates, as will be seen below, but the quantity measured is always the total detection probability $P_\alpha = \sum_k P_\alpha^{(k)}$.

4.3 EXPERIMENTAL IMPLEMENTATION

In order to realize the QDT model described above, we need to be able to reliably generate coherent states $|\alpha\rangle$ with well-defined average photon number $|\alpha|^2$ and relate these to their detection probability P_α . The deliberate generation of coherent states is achieved by accurate attenuation of light produced in a pulsed laser source. The attenuation procedure is very similar to how a precise cw photon flux is generated for the OCDE measurement. The employed experimental setup (see Figure 4.3-1) is, therefore, almost identical to the OCDE setup. The only difference is the use of a pulsed laser source (PriTel FFL-40M) which produces pulses of 1 ps duration at a stable repetition rate of 40 MHz. The remaining setup is identical to the OCDE setup which has already been explained in section 3.5.2.1 with details in annex A3 and will not be repeated here.

The laser pulse duration which is much shorter than the detector's recovery time ensures a maximum of one detection event per pulse, and the repetition rate of 40 MHz leaves sufficient time in between successive pulses for the detector to fully recover. The detection probability P_α of a specific coherent state α is subsequently determined by the ratio of the detector count rate R_c and the laser repetition rate RR , i.e. $P_\alpha = R_c/RR$.

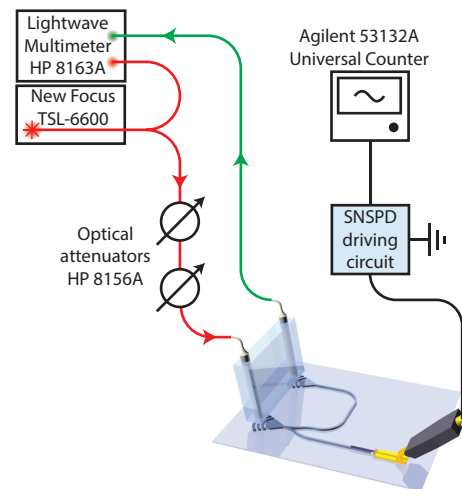


Figure 4.3-1: Experimental setup for QDT measurement

4.4 DETECTION REGIMES

Before the full QDT model which was devised above is employed in order to extract the exact internal quantum efficiency values, a first look at the general detector response is helpful. By this approach, various detection regimes which differ substantially in their sensitivity to a specific photon number can be identified.

4.4.1 SINGLE-PHOTON DETECTION REGIME

The detection probability for 80 nm wide integrated SNSPDs of varying length is depicted in Figure 4.4-1. During the measurement the bias current was kept constant at 90% of the respective critical current. As can be seen, on the log-log scale plot all detectors exhibit the same general trend – a linear increase with identical slope and a roll-off below 5×10^5 photons per second on average which represents the dark count level. The displacement of the curves is due to differences in their OCDEs with the shortest detector exhibiting the lowest efficiency. More important is, however, the slope of

unity which proves the true single-photon detection capability. This can be explained as follows: the single slope in P_α indicates that only one of the $P_\alpha^{(k)}$ terms contributes – otherwise a nonlinear dependence on $|\alpha|^2$ were seen; furthermore, from eqn. 4.2.3-5 it can be seen that $P_\alpha^{(k)} \propto |\alpha|^{2k}$ which for a slope of unity on a log-log plot indicates $k = 1$. In other words, the slope of unity in Figure 4.4-1 confirms that the absorption of $k = 1$ photons somewhere along the nanowire is responsible for causing a detection event.

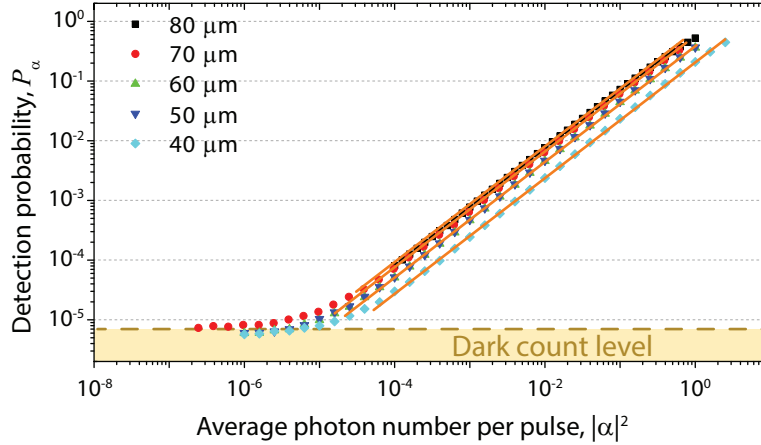


Figure 4.4-1: Detection probability plotted as a function of average photon number for 80 nm wide integrated SNSPDs of varying length, all biased at 90% of their critical current. The linear fits (solid orange lines) all show slope of unity on the log-log scale. *Parts of this data has been previously published in ref. [237].*

It was found in all integrated SNSPDs measured during the work for this thesis that in the high-bias regime the single-photon ($k = 1$) contribution by far dominates. In certain cases [193], it was even the only regime found. In the following section, multi-photon detection regimes and their dependences on geometry and bias current will be presented.

4.4.2 MULTI-PHOTON DETECTION REGIMES

In the data presented above, the bias current was kept constant at a high value of 90% of the critical current. In order to make other detection regimes visible the detector's sensitivity has to be adjusted. Single-photon sensitivity requires bias currents larger than the threshold current (see section 2.3.3.2). If the bias current is reduced below the threshold current, a single photon alone is insufficient for the formation of a normal-conducting domain. Figure 4.4-2 shows the detection probability of a 120 nm wide, 80 μm long integrated SNSPD measured at different bias currents. As can be seen, at a high bias current of 90% of the critical current, the single slope of unity is recovered (indicated by the orange solid line). When the current is, however, reduced to 60% a change in the slope at large photon numbers becomes visible (red solid line). The extent of the second slope grows as the bias current is reduced further to 50% of the critical current until at 40% a third slope appears (magenta solid line). These different slopes arise similarly to the one introduced above: they are sections where one particular term in the sum in eqn. 4.2.3-5 dominates. Again, the dependence is given by $P_\alpha^{(k)} \propto |\alpha|^{2k}$ such that on a log-log plot k determines the slope. It is remarkable that only one of the k terms in the sum is ever dominant while the others appear to vanish almost completely. The dominant term appears to depend on the biasing conditions with the higher order terms becoming dominant for lower bias currents. It should be noted, however, that for mean photon

numbers which are a lot lower than unity, i.e. $|\alpha|^2 \ll 1$, the single-photon ($k = 1$) detection regime always dominates.

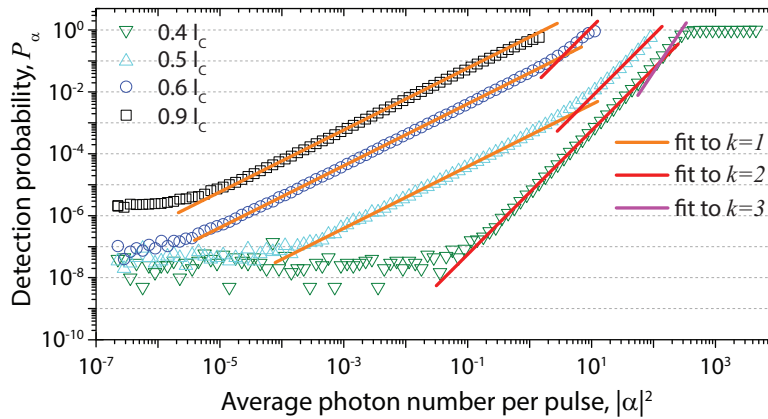


Figure 4.4-2: Detection probability plotted as a function of average photon number for 120 nm wide, 70 μm long integrated SNSPD for various biasing conditions. The single-polynomial fits (solid lines) indicate the different detection regimes. *This data has been previously published in ref. [237].*

A similar trend can be seen when assessing the dependence of the multi-photon detection probability on wire width. Figure 4.4-3 shows the data obtained at integrated SNSPDs of identical length but varying width for the same biasing conditions of 40% of the critical current. As can be seen the narrowest wire (80 nm) shows a single slope of unity ($k = 1$) over the entire photon number range indicating that it is always sensitive to single photons even at low bias. At 100 nm stripe width a second $k = 2$ slope appears for large photon numbers which at the 120 nm wider detector spans the entire photon number range. This clearly indicates an increased multi-photon susceptibility for wider wires.

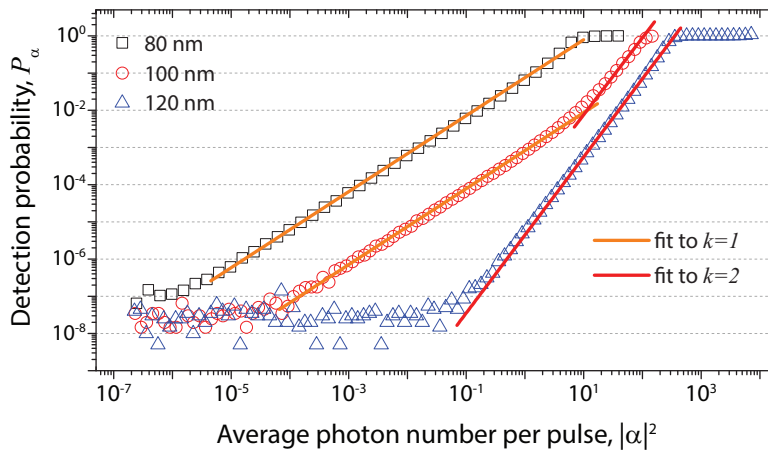


Figure 4.4-3: Detection probability plotted as a function of average photon number for 70 μm long integrated SNSPDs of varying width and identical biasing conditions (40% of the critical current). The single-polynomial fits (solid lines) indicate the different detection regimes. *This data has been previously published in ref. [237].*

On a microscopic basis, our findings can be explained qualitatively in the photon-triggered vortex model [113], [114] as well as the diffusion-based vortex model [159], [168]. Both models assume that the absorption of a single photon leads to a local reduction in the order parameter and a subsequent redistribution of the bias current. These processes locally lower the edge barrier potential and facilitate the formation of vortices which ultimately leads to VPSs and the local destruction of superconductivity. If the current redistribution by itself is too small to induce a VPS

then the absorption of an additional photon can enhance the redistribution and thus facilitate vortex formation. If the energy of two photons is still insufficient, the addition of a third photon can bridge the gap, etc. This explains the dependence and increased chance of multi-photon detection for low bias currents. As the spatial extent of the local order parameter reduction depends on the photon energy, the area can clearly be increased by the absorption of another photon. Hence, the dependence on wire width.

4.5 DETECTOR RESPONSE EXTRACTION

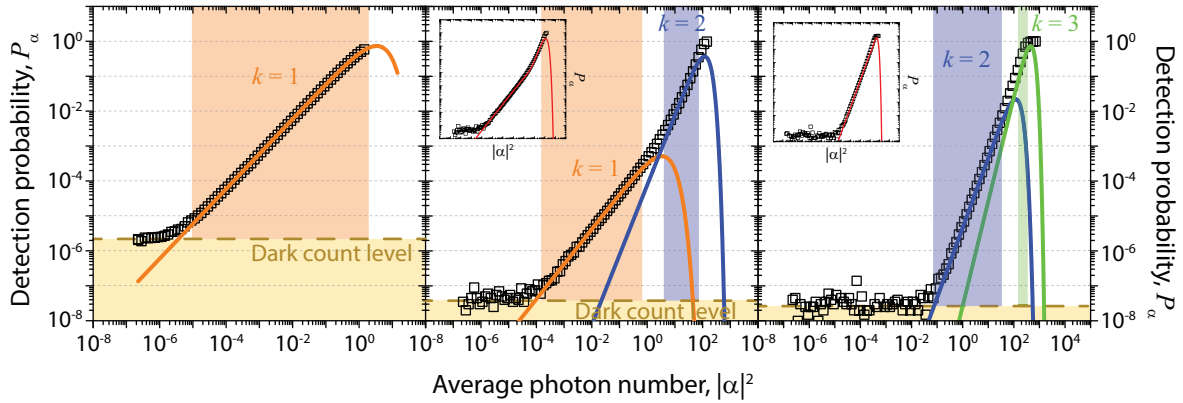


Figure 4.4-1: Detection probability plotted as a function of average photon number for 120 nm wide, 70 μm long integrated SNSPD for various biasing conditions (left: 90% I_c ; center: 50% I_c ; right: 40% I_c). The solid lines represent single $P_\alpha^{(k)}$ fits based on our model. The insets show the full $\sum_k P_\alpha^{(k)}$ fit. The shaded areas indicate the different detection regimes. *Parts of this data has been previously published in ref. [237].*

Having seen how an integrated SNSPD responds in different situations we will now apply the model which was devised in the preceding section. The model allows us to extract the response coefficients c_k which represent the internal quantum efficiencies (IQEs) for different photon numbers. Figure 4.4-1 shows the data of a 120 nm wide, 70 μm long SNSPD for three different bias currents (black squares). The total detection probability $\sum_k P_\alpha^{(k)}$, where $P_\alpha^{(k)}$ is given by eqn. 4.2.3-7, was fit to the data. The orange, blue, and green lines represent individual $P_\alpha^{(k)}$ -terms for $k = 1, 2$, and 3, respectively. The complete $\sum_k P_\alpha^{(k)}$ fit is depicted in the insets. As can be seen from the fits, the sum was not carried out to infinity, but aborted after the last k which were able to see in the initial assessment above. The roll-off in the individual $P_\alpha^{(k)}$ -terms was previously remarked upon. It shows that only one term is ever dominant and is the main reason why the assessment in the preceding section was possible.

From the fits in Figure 4.4-1 we are able to extract the detector's IQE values for the simultaneous detection of k photons. The results for three different 70 μm long detectors are shown in Figure 4.5-3. The red single-photon ($k = 1$) curves show the familiar shape of an on-chip detection efficiency (OCDE) curve which is an indication that this model is consistent with data obtained from a different measurement. The blue 2-photon and green 3-photon curves contribute only in the low bias regime, but reach values close to unity in their respective range. From a practical application point of view, the graphs presented in Figure 4.5-3 indicate the bias current necessary to realize

sensitivity to a specific photon number. As can be seen, the wider wire is more suitable for the detection of larger photon numbers.

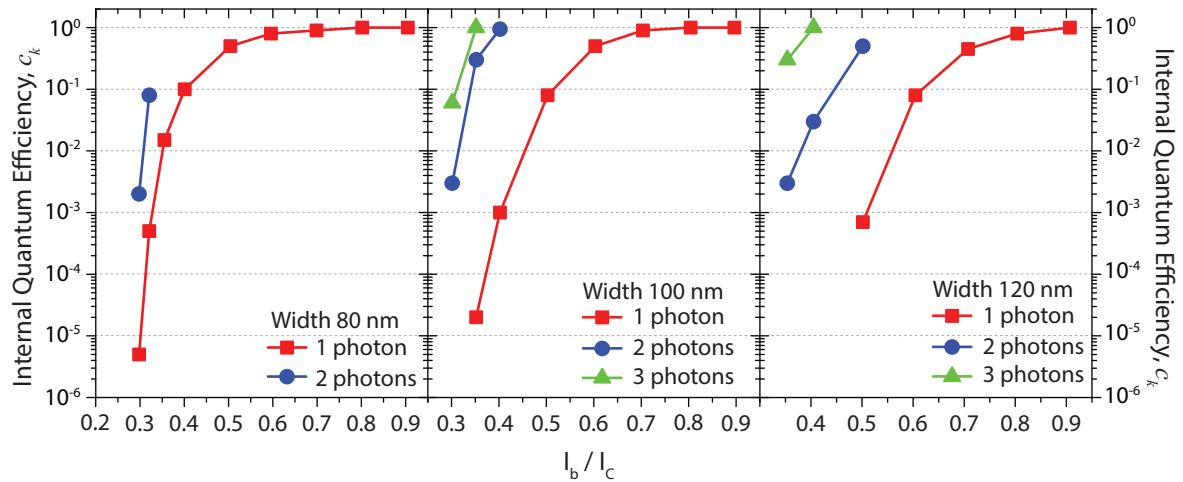


Figure 4.5-3: Internal quantum efficiency / response coefficient as a function of normalized bias current for a 80 nm (left), 100 nm (center), and 120 nm wide, 70 μm long integrated SNSPD. This data has been previously published in ref. [237].

In order to test our model, we compare the IQE values obtained from the QDT model to OCDE values which we have measured directly (see section 3.5.2). It is important to note that in the OCDE measurement the photon flux is sufficiently small to exclude multi-photon contributions. The single-photon IQE should therefore be proportional to the OCDE since the OCDE is given by the product of IQE and absorption efficiency (AE) where the AE is a current-independent scaling factor. Figure 4.5-2 shows the IQE and OCDE values of the same detectors plotted in one chart. It directly appears that the curves follow the same trend and that the IQE is always larger than the OCDE. We furthermore extract the AE values for the three detectors by the ratio of OCDE and IQE and obtain $(58.52 \pm 15.96)\%$ for the 80 nm wide, $(71.10 \pm 10.09)\%$ for the 100 nm wide, and $(43.17 \pm 13.74)\%$ for the 120 nm wide integrated SNSPD. These values are realistic and we interpret this as a confirmation that our model works. The low AE value of the 120 nm wide detector we attribute to the fabrication-related uncertainties.

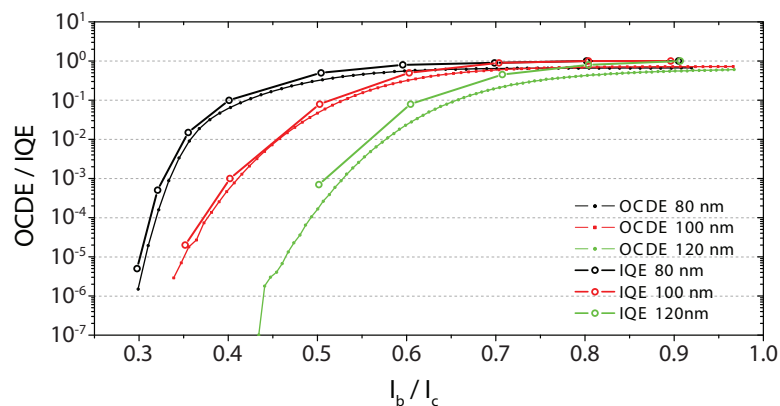


Figure 4.5-2: IQE and OCDE as a function of normalized bias current for a 80 nm (black), 100 nm (red), and 120 nm (green) wide, 70 μm long integrated SNSPD.

4.6 CONCLUDING REMARKS

In this chapter, it was confirmed by statistical means that the integrated SNSPDs are capable of true single photon detection. Furthermore, lower biasing conditions were shown to enable sensitivity to larger photon number and insensitivity to lower photon numbers. Up to three different detection regimes were identified in integrated SNSPDs with nanowires of 80 nm, 100 nm and 120 nm width. The detection regime can be selected by appropriate tuning of the bias current. Tuning curves are provided by IQE curves which were extracted by a QDT model. The specific QDT model was derived from the basic QDT concept in order to account for the travelling wave geometry of the detecting nanowire. It was found that wider wires are more suitable for detection of larger photon numbers. This can be explained by the favorable superconductivity breakdown conditions which are given by multiple photons in wider wires. The QDT model's results were found to be consistent with previously acquired OCDE data.

The detection capability should not be confused with photon number resolution. Truly number-discriminating detectors produce output signals which dependent on the input photon number. Here, only a lower detection limit in the photon number is set which allows for the exclusion of photon states below the limit. In other words, the detector is sensitive to the state $|n\rangle$ and therefore insensitive to the state $|m\rangle$ with $m < n$. Due to the low biasing conditions the noise contribution is also severely reduced. The capability to introduce a lower bound in the SNSPD's photon number sensitivity is assumed to be of interest for applications where selective detection of specific photon states is desired.

5 SINGLE-PHOTON SPECTROMETRY

This chapter serves two purposes. On the one hand, two implementations of single-photon spectrometers are demonstrated, which enable an extremely high level of experimental fidelity. On the other hand, the implementations serve as a proof-of-principle for far more advanced applications in the field of integrated quantum information technology. The spectrometers are based on the simultaneous operation of multiple integrated SNSPDs within one photonic circuit. This constitutes a milestone in the development of integrated quantum optical circuitry as it demonstrates the resolution – if not even elimination – of present issues in scalability and detection performance which currently limit integrated quantum information applications such as QKD or LOQC.

The single-photon spectrometers target two different applications: one layout is designed for operation at telecom wavelengths around 1550 nm and can act as a multi-channel single-photon receiver; the other design is intended for the spectroscopic analysis of silicon vacancy (SiV) color centers which have been proposed as single-photon sources. We resolve the optical emission of SiVs at 740 nm spectrally as well as temporally in a single device, and exploit the detectors' superior timing performance to create a complete fluorescence lifetime image (FLIM).

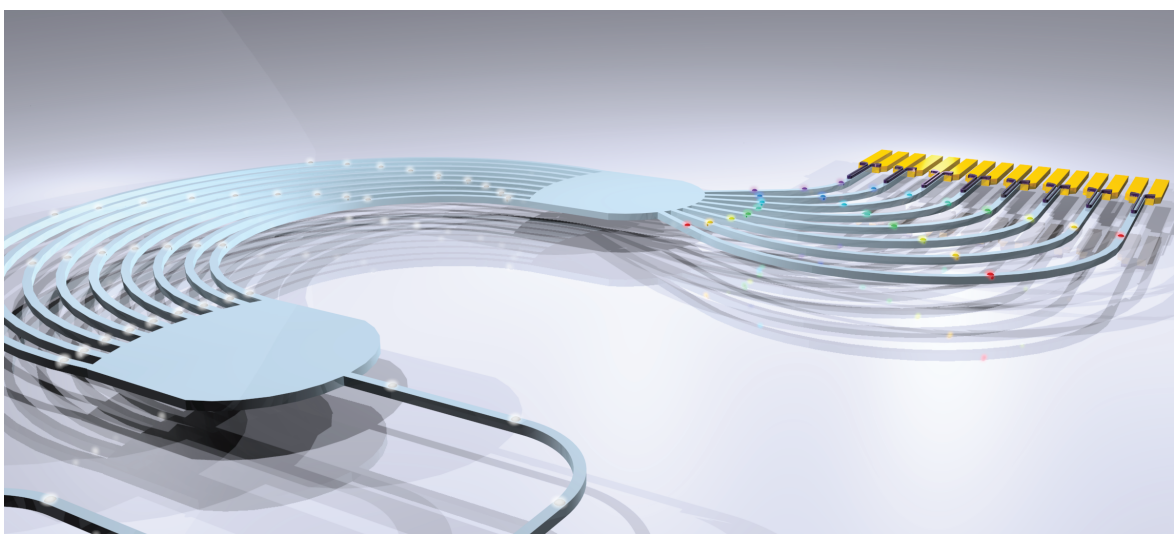


Illustration of arrayed waveguide grating equipped with eight waveguide-integrated SNSPDs

Note: Large parts of the data and the results presented in this chapter are part of a publication which is currently in preparation (authors: O. Kahl, V. Kovalyuk, S. Ferrari, G. Gol'tsman, W. Pernice).

5.1 SPECTROMETER CONCEPT AND DESIGN

In general, photodetectors convert radiant energy into electrical signals while being mostly insensitive to differences in photon energy. Spectrally resolved detection therefore requires the spatial or temporal separation of the spectral components and their individual measurement. A diffraction grating or prism is usually used for the separation and either a single detector or a detector array is utilized for the measurement. In this chapter an *arrayed waveguide grating (AWG)* [179], [209] is employed as the planar, integrated counterpart to the free space grating in order to guide individual fractions of an input spectrum into specific optical waveguides. Each of those output waveguides possesses an integrated SNSPD at its end. The count rates measured in the individual output waveguide *channels* thus allow for the reconstruction of the input spectrum.

The motivation for the use of an AWG in combination with integrated SNSPDs is twofold: on the one hand, it enables the spectral discrimination of an optical broadband signal on a single-photon level; on the other hand, the SNSPDs' high timing accuracy allow for the temporal examination of the individual spectral components. This concept expands the general spectroscopic approach by a temporal dimension and effectively enables spectrally resolved fluorescence lifetime measurements on the single-photon level in one device. This capability will be demonstrated in the following by acquiring a complete fluorescence lifetime image of silicon vacancies (SiVs) from a cluster of nanodiamonds.

The specific implementation presented here contains an array of eight detectors. This number is limited by the constraints of the experimental setup. The general design can be expanded to many more detectors. AWGs with several tens of output channels have been demonstrated [210], [211] and hundreds of integrated SNSPDs can easily be fabricated on a single chip in one fabrication run.

5.1.1 BASIC CONCEPT

Most spectrometers are based on the spatial separation of the incident light's spectrum. In free space, gratings or prisms are usually utilized for this purpose. While the prism's separating effect is based on *refraction*, the grating employs a *diffractive* approach by introducing incremental phase delays inside the light beam (see Figure 5.1-1). Due to mutual interference inside the beam the spectral components effectively separate in space and can be singled out for further analysis or processing [212], [213].

The diffractive separation approach is amenable to photonic integration as is illustrated in Figure 5.1-2. Light inside a waveguide is spread out into multiple identical waveguides which combine again at some later point. In analogy to the free space grating, we now deliberately introduce a phase delay $\Delta\phi$ from one waveguide to the next by incrementally extending the lengths of neighboring waveguides. The division from one into multiple waveguides and vice versa is performed by *star couplers* [179] which are essentially larger slab waveguide or free space regions. Given a suitable geometry, star couplers are capable of homogeneous, low-loss

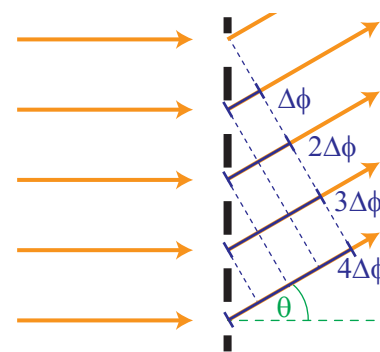


Figure 5.1-1: Schematic illustration of transmission diffraction grating

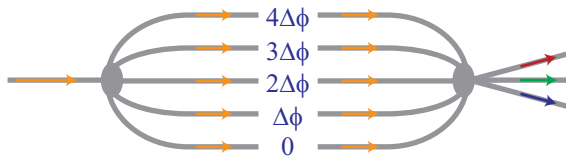


Figure 5.1-2: Illustration of AWG's principle of operation

redistribution of the optical power from one number of input waveguides into another number of output waveguides [179]. The interference which leads to the spatial redistribution of the input spectrum occurs inside the combining star coupler. The star

couplers used for the AWGs in this thesis are based on the Rowland circle geometry which will be explained below.

The AWG concept was first proposed by M. K. Smit in 1988 as de-multiplexing element in photonic networks [214] and was realized soon after by Vellekoop and Smit himself [215], [216]. Today, AWGs are widely used as multiplexers and de-multiplexers in wavelength division multiplexed (WDM) photonic networks. Common AWG implementations are based on a multilayer design for improved transmission characteristics [210], [217]. In order to facilitate fabrication, given our possibilities, we adopt a single-level design.

5.1.2 DESIGN AND PARAMETERIZATION

The principle of operation of an AWG can be explained using Figure 5.1-3. Light is inserted into the AWG through the waveguide on the bottom left. The first star coupler is designed such that light which traverses it excites propagating modes inside the arrayed waveguides. At the end of the waveguide array another star coupler is located where the light exiting the waveguides will constructively interfere in one point on the coupler's focal line (see red line in right drawing of Figure 5.1-3). The star coupler thus effectively mimics the behavior of a focusing lens. The geometry which enables the focusing commonly referred to as *Rowland circle* design or *Rowland mount* [209], [218]. It is composed of two curved facets separated by a distance R (see right schematic in Figure 5.1-3). The radii of curvature are R and $R/2$ on the top and bottom, respectively.

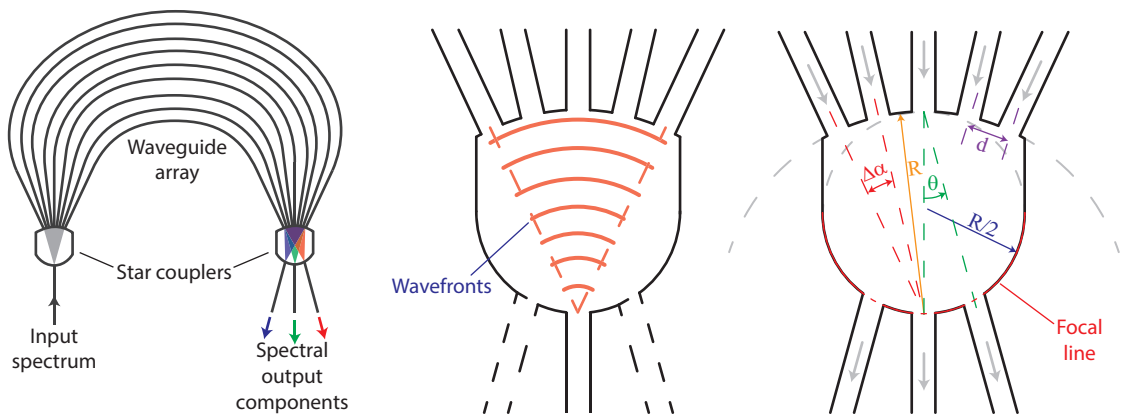


Figure 5.1-3: Left: schematics of AWG. Center: illustration of wave propagation inside star coupler, the principle applies to the input and the output star coupler. Right: geometric layout of star coupler

The simplest case of an AWG is that all waveguides in the array are equal in length or such that their relative length differences result only in phase delays of integer multiples of 2π . In this scenario, interference causes focusing into the central output waveguide. If, however, the length differences ΔL of neighboring waveguides are chosen such that a specific phase difference $\Delta\phi \neq 2m\pi$ with $m \in \mathbb{Z}$ is produced at the waveguides' ends, then the resulting wavefront becomes tilted upon interference and the focal point moves left or right on the focal line. The focal point can

thus be shifted to the location of a specific output waveguide along the focal line by carefully designing ΔL .

Usually, AWGs are designed with a specific input spectrum in mind. The spectrum naturally possesses a central wavelength λ_c which can be used to formulate a condition for the length difference which causes the central wavelength to be focused into the center output waveguide [209]:

$$\Delta L = m \frac{\lambda_c}{n_{eff}(\lambda)} \quad 5.1.2-1$$

Here, $m \in \mathbb{Z}$ denotes the diffraction order of the grating, and $n_{eff}(\lambda)$ is the waveguide's mode index. The associated phase difference is $\Delta\phi = \beta\Delta L$ where $\beta = 2\pi n_{eff}/\lambda$ denotes the mode propagation constant. It should be noted that n_{eff} and therefore β are different in the star coupler and in the waveguide: inside the waveguide light propagation is confined in two dimensions which yields the waveguide's 2D mode index $n_{eff}^{(wg)}$, whereas the large spatial extent of the star coupler allows for one dimensional approximation which produces a 1D slab mode index $n_{eff}^{(slab)}$. From geometrical considerations of the right schematic in Figure 5.1-3 it follows that the angular displacement θ of the focal point is given by

$$\sin \theta = \frac{\Delta L}{d} = \frac{\Delta\phi - 2m\pi}{\beta^{(slab)}d} \quad 5.1.2-2$$

where d denotes the lateral spacing of the arrayed waveguides at the star coupler.

In principle, the description thus far is sufficient for the design of functional AWGs. It is, however, helpful to introduce two other quantities which help in finding suitable values for the parameters ΔL and d . AWGs are often characterized by their dispersion D which describes the angular displacement $ds = R d\theta$ of the focal point relative to a change in optical frequency df . It can be shown that for $R \gg d$ it follows [209]

$$D = \frac{ds}{df} = \frac{\lambda_c}{c} \frac{n_g}{n_{eff}^{(slab)}} \frac{R\Delta L}{d} \quad 5.1.2-3$$

where n_g denotes the group index. The importance of the AWG dispersion D becomes clear as it introduces a dependence on the radius of the star couplers and thereby relates the three AWG design parameters R , ΔL , and d . The second quantity which helps in restricting the possible parameter value range is the well-known *free spectral range (FSR)* which is given by

$$\Delta f_{FSR} = \frac{c}{n_g \Delta L} = \frac{n_{eff}^{(wg)} c}{\lambda_c n_g m} \quad 5.1.2-4$$

It represents the spectral range which separates individual diffraction orders. In order to prevent successive diffraction orders from overlapping, the FSR should be larger than the input spectrum.

5.1.3 TRANSMISSION OPTIMIZATION

Beside scattering loss in the photonic structures and possible absorption at impurities, AWGs are plagued by imperfect light conversion from the slab waveguide region of the first star coupler to the

waveguide array [219]. Such a scenario is displayed in Figure 5.1-4 where significant amounts of light are scattered out of the star coupler. The effect is due to the inherent mismatch between the slab waveguide mode and the modes of the arrayed waveguides. Several methods have been suggested to improve the coupling of the slab mode to the 2D waveguide modes. These include the localized insertion of high refractive index materials [220] or the preparation of a vertical tapering region [219], [221]. Neither of these proposals was realizable within the scope of this thesis. We therefore employ an approach which was suggested by Ohno et al. [222] and is based on the utilization of parabolic tapers [223].

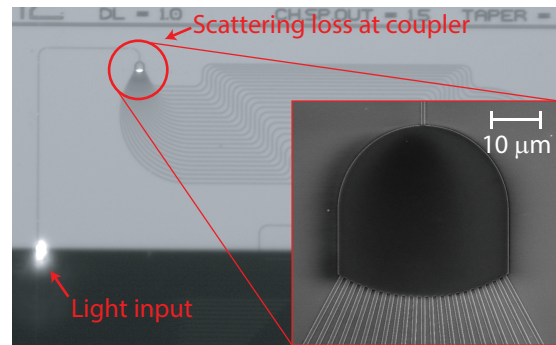


Figure 5.1-4: Scattering loss at first star coupler. Inset: SEM image of star coupler without waveguide tapers

In general, the degree of coupling between two modes is determined by the spatial overlap of the modes' fields [177]. Therefore, in order to optimize the coupling, the field overlap has to be maximized. We use a generic approach in which we consider the horizontal (x) and vertical (y) dimensions separately. 2D mode profiles in the tapers and waveguides are obtained numerically using COMSOL Multiphysics®. 1D slab modes are calculated analytically using standard literature approaches like the one detailed in chapter two of ref. [180]. Furthermore, the arrayed waveguides are carefully designed to only support a single quasi-TE mode.

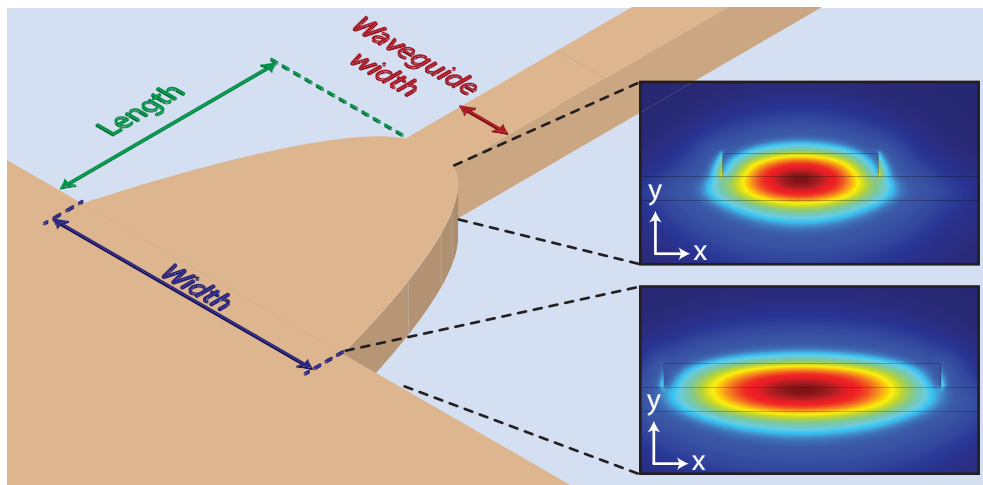


Figure 5.1-5: Design of parabolic taper showing lateral expansion of fundamental waveguide mode

The quasi-1D slab waveguide mode can be assumed to vary weakly in the x -direction [179]. In this case, mode overlap can be improved by laterally increasing the spatial extent of the 2D waveguide modes. To achieve this we employ parabolic waveguide tapers [223] (see Figure 5.1-5). Such tapers have also been suggested to improve field uniformity by deliberately inducing a higher order mode inside the taper [179]. In contrast, we use the tapers adiabatically thus preserving a single mode while expanding its diameter. The width of the taper is given by a simple parabolic equation $W^2(z) = \alpha \lambda_{eff} z + w_0^2$ where λ_{eff} denotes the effective wavelength inside the waveguide, α is an arbitrary design constant smaller than unity, and w_0 is the non-tapered waveguide width. By choosing α smaller than unity, it is ensured that the mode conversion occurs adiabatically [223]. In

theory, the mode overlap can be maximized by expanding the taper width up to the point at which the entire star coupler facet is covered. Realistically, the degree of tapering is limited by the finite resolution of the fabrication processes. Adjacent tapers must be placed sufficiently far apart in order to avoid coalescence.

In the y -direction, we extract a 1D representation of the arrayed waveguide's 2D mode by evaluating the field along a central vertical line at $x = 0$ for comparison with the slab mode. We use a central cutline in the FEM model used for the 2D waveguide mode calculation in order to obtain the field profile. The extracted field distributions are shown in Figure 5.1-6, the cutline in the field mode is depicted in the inset. As can be seen, the profiles hardly differ. Numerical analyses of other waveguide geometries (full and $\frac{3}{4}$ etch) yielded a negligible changes in the field distribution. Changes in the geometry along the y -direction therefore offer limited potential to improve mode coupling, but also do not produce adverse effects.

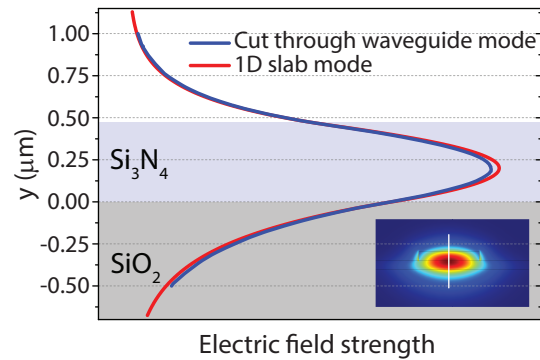


Figure 5.1-6: 1D mode profile of star coupler slab mode for 450 nm thick Si_3N_4 structure (red) and profile along a central cutline through 2D mode of half-etched waveguide (blue). Inset: 2D mode profile including cutline (white)

5.1.4 PARAMETER DESIGN

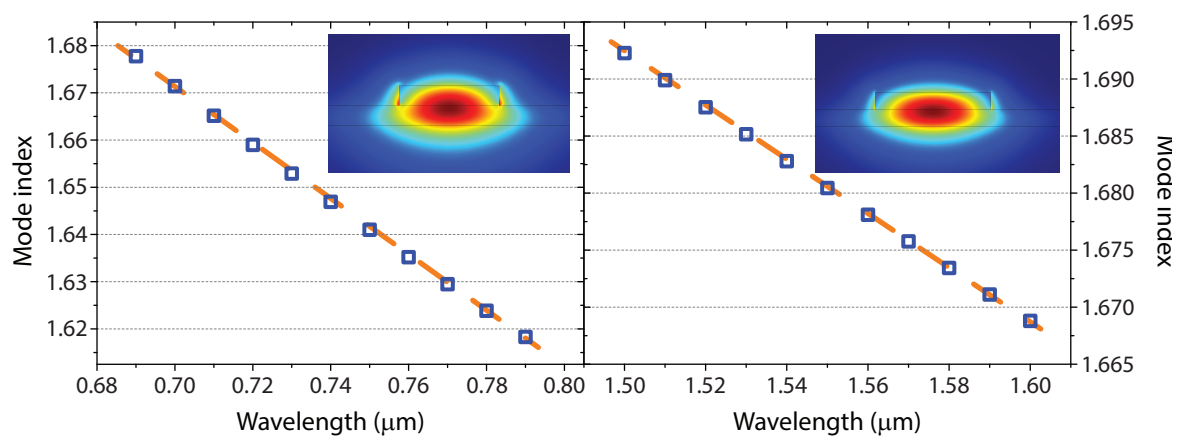


Figure 5.1-7: Effective mode index as a function of wavelength extracted from FEM simulations using COMSOL Multiphysics® for the waveguides designed for 740 nm (left) and 1550 nm (right). The insets show the mode profiles at the central wavelength.

In the case of this thesis, two AWGs were designed – one ranging from 1540 to 1560 nm for the telecom regime, and another one ranging from 720 to 760 nm to collect fluorescence from silicon vacancies centered at 740 nm. The required waveguide parameters for the AWG design were obtained through numerical mode index calculations using COMSOL Multiphysics®. The waveguide structures were designed to carry a single quasi TE mode at the respective wavelength. For 1550 nm the same waveguiding structures as in the detector characterization in chapter 3 were used – a 1.5 μm wide, 225 nm high ridge waveguide made from a 450 nm thick Si_3N_4 film on top of a 2.6 μm thick SiO_2 layer. The design for 740 nm used a 200 nm thick Si_3N_4 film on top of a 2.0 μm thick SiO_2 layer as base material from which 500 nm wide, 100 nm high ridge waveguides were fabricated. The results

of the mode analyses are shown in Figure 5.1-7. From this data the group indices n_g at 740 nm and 1550 nm were extracted – 1.8199 for 740 nm and 2.029 for 1550 nm. The slab indices were calculated analytically following the standard procedure outlined in chapter two of ref. [180]. For the 1550 nm structure the slab index was found to be 1.7301 and for the 740 nm structure 1.7302.

In the following we will introduce the AWG parameters and how they were chosen. Over the time of this thesis the parameters were varied and test devices fabricated in order to find an optimal set. The parameter sets below produced results which best suited the intended application.

We begin our AWG design by choosing a diffraction order which enables a sufficiently large FSR to accommodate a desired bandwidth. In the case of the 1550 nm AWG, we set the diffraction order to $m = 54$ which following eqn. 5.1.2-4 produces a FSR of $\Delta f_{FSR} = 2.978$ THz which corresponds to a wavelength window of 23.9 nm around 1550 nm. The length increment of $\Delta L = 50 \mu\text{m}$ is directly determined by the choice of the diffraction order.

Next we evaluate possibilities for the star coupler radius. For $R = 100 \mu\text{m}$ a dispersion of $D = 0.2595$ THz/ μm is realized. In combination with the result for the FSR this yields a $33.3 \mu\text{m}$ spatial range on the focal line for one diffraction order of 23.9 nm. In this constellation, we place the output waveguides $2.7 \mu\text{m}$ apart in order to achieve $2 \mu\text{m}$ wavelength separation per channel and, therefore, 16 nm optical bandwidth around the central wavelength of 1550 nm. The final transmission spectrum is schematically illustrated in Figure 5.1-8.

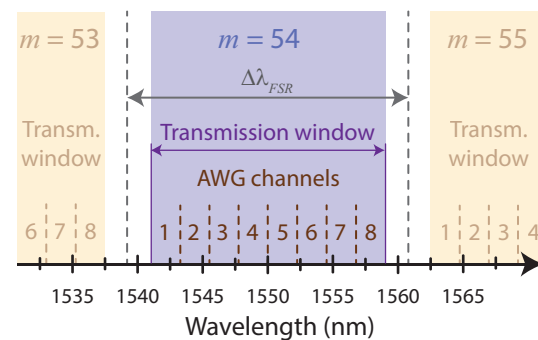


Figure 5.1-8: AWG's transmission channel spectrum illustrated at 1550 nm AWG

The same procedure was employed for the 740 nm AWG. The results are summarized in the table below.

Central wavelength	Diffraction order	FSR	Transmission window	Waveguide separation	Channel FWHM	Taper length	Taper width
1550 nm	54	24 nm	16 nm	$2.7 \mu\text{m}$	2.2 nm	$5.0 \mu\text{m}$	$2.5 \mu\text{m}$
740 nm	11	60 nm	45 nm	$1.75 \mu\text{m}$	6.4 nm	$0.75 \mu\text{m}$	$1.0 \mu\text{m}$

The integration of integrated SNSPDs with an AWG is a straightforward process. The fabrication procedure is identical to the one introduced in section 3.3, only the photonic circuitry is more advanced and multiple detectors are integrated with a single device. The integrated SNSPDs are located at the end of the output waveguides. Optical read-out facility is, however, maintained by a 50:50 Y-splitter before the detector, from which one arm is connected to an ancillary GC. This is necessary in order to enable optical characterization. A finalized detector-integrated AWG is shown in Figure 5.1-9.

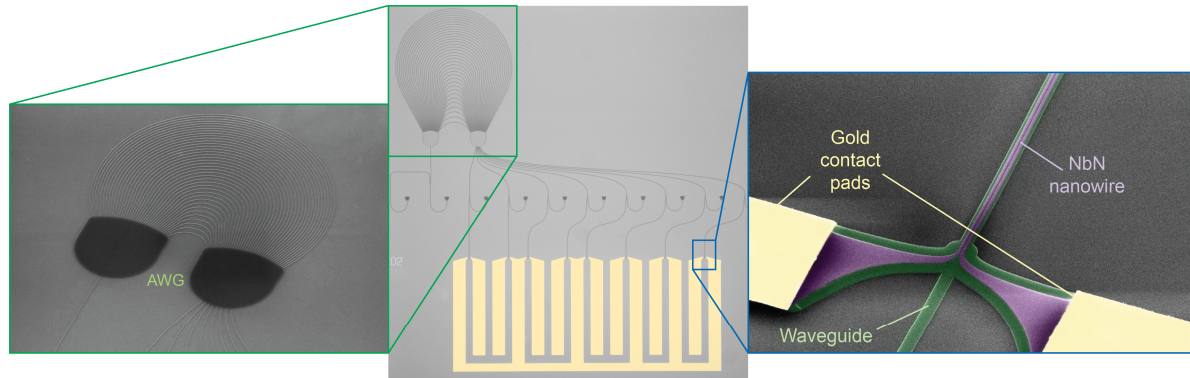


Figure 5.1-9: Left: SEM image of AWG. Center: AWG with integrated SNSPD array; the contact pad (false color yellow) features a common ground for all detectors. Right: False color SEM image showing integrated SNSPD on photonic waveguide and contact pad connection.

In order to realize optimal detector performance, the detector layout which produced the best results at 1550 nm during the previous characterization was chosen. All integrated SNSPDs on the AWGs were therefore 80 nm wide, 80 μm long with a gap of 100 nm between the stripes.

5.2 MULTI-CHANNEL SINGLE-PHOTON RECEIVER AT 1550 NM

5.2.1 OPTICAL CHARACTERIZATION

An initial optical characterization of the AWG is necessary to ensure proper device functionality. The characterization is performed outside the cryostat on an alternate measuring platform since this measurement does not require cryogenic temperatures. A photograph of the setup and a schematic illustration of the mounted sample are depicted in Figure 5.2-1. The sample is situated on a piezo-actuated x-y-translation-rotation stage for accurate positioning underneath a fiber array to couple light into and out from the chip. The fiber array is held by a cantilever which can be raised and lowered for chip installation and removal. Alignment of the on-chip devices is facilitated by real-time

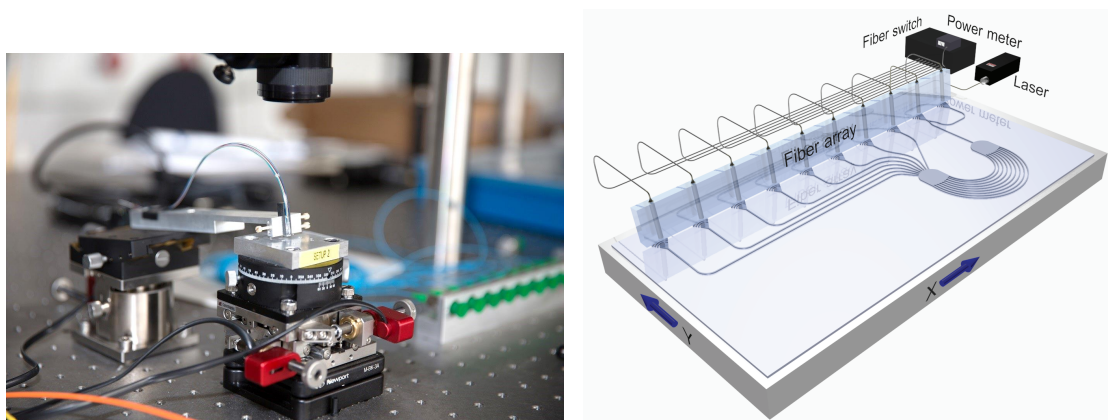


Figure 5.2-1: Left: Photo of transmission setup used for AWG characterization showing piezo-actuated x-y-translation-rotation stage, fiber array mounted in cantilever, and microscope above. Right: Schematic illustration of AWG chip mounted on piezo-driven stage below ten-port fiber array for light insertion and collection.

visual feedback from a CCD camera mounted above the sample stage. Light from a tunable laser is sent through the properly positioned fiber array into the photonic circuit. The transmitted light is collected from the AWG's eight output ports and sent to a fiber switch (Dicon GP700). The active channel, set by the fiber switch, is routed onward to a power meter or calibrated photodetector for measurement of the transmitted optical. By sweeping the laser's wavelength and simultaneously recording the transmitted power, a complete transmission spectrum is obtained. A self-made computer program is used for hardware control and automated data acquisition.

The optical transmission spectrum obtained from the AWG is displayed in Figure 5.2-2. The spectrum has been normalized to the signal measured on the reference GC and adjusted for the 50% loss due to the 50:50 Y-splitter in the output channels. The eight intended transmission bands are immediately visible. The central wavelength is slightly blue-shifted by 3.5 nm from the intended wavelength of 1550 nm. We attribute this to a fabrication-related deviation in the waveguide shape from the design. It does, however, not impair the device's functionality. The designed transmission window and FSR agree well with the measured spectrum, as does the channel width (FWHM) of 2.2 nm. The overall transmission is $(35.65 \pm 8.81)\%$ which corresponds to an *insertion loss* of 4.48 dB. The variation in transmission between the individual channels within one device is characterized by the *insertion loss uniformity* which is defined as the difference between the channels with best and worst transmission within one device. The insertion loss uniformity of our specimen is 4.04 dB (39.4%). The last important characteristic quantity is the *channel cross-talk*. It pertains to the signal leakage between adjacent channels. It is quantitatively assessed by evaluating the largest foreign signal at the center of the channel's transmission window. In our sample the cross-talk level is 12.87 dB. A comparison to commercially available AWGs which provide insertion loss around 3.0 dB, insertion loss uniformity of 1.0 dB, and cross-talk levels below 30 dB [224], shows that there is still room for improvement in the current design. The reached performance levels are, however, acceptable for the demonstrative purposes of this thesis.

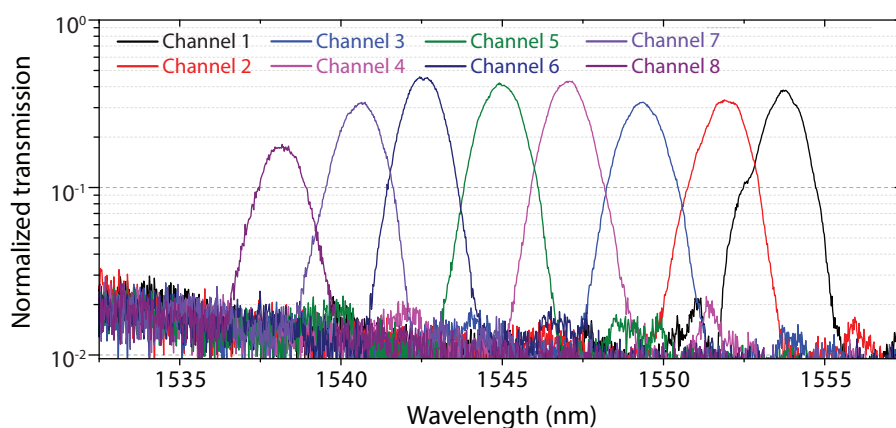


Figure 5.2-2: Optical transmission spectrum of AWG with integrated SNSPD

5.2.2 DETECTOR CHARACTERIZATION

Several reference detectors were included on the chip to allow for a proper detector characterization, i.e. measurement of the on-chip detection efficiency (OCDE), timing jitter, and decay time (see section 3.5). Reference circuits identical to the ones introduced in section 3.3 were

included on the chip with the AWGs. All SNSPDs are identical and feature a 80 nm wide wire, 100 nm gap and 80 μm absorption length. The detector characterization is performed inside the cryostat under the operating conditions which were introduced in section 3.4. The same characterization procedures as the ones outlined in section 3.5 were used. The obtained characteristic parameters were found as follows: OCDE of $(51.89 \pm 6.66)\%$, timing jitter of $(47.56 \pm 4.03)\text{ps}$, and recovery time of $(5.64 \pm 0.44)\text{ns}$.

The data agrees with the results reported in chapter three. The OCDE of $(51.89 \pm 6.66)\%$ is slightly reduced relative to previous results²¹, but it is still at an acceptable level. All of the above data was obtained at a wavelength of 1550 nm. Over the eight-channel wavelength window of 16 nm around 1550 nm the detector characteristics are assumed to change only insignificantly due to the small differences in photon energy. Experimental checks confirm this assumption.

5.2.3 SPECTRALLY RESOLVED SINGLE-PHOTON DETECTION

Having characterized the AWG and detectors individually, we now assess how two components fare in conjunction. The integrated SNSPDs are connected to the same biasing and read-out circuitry as described in section 3.4. The detector count rates are evaluated by the Agilent 53132A high frequency counter. The input laser is strongly attenuated and is swept across a wavelength range. The count rates of the integrated SNSPDs at the end of the AWG's output waveguides are recorded simultaneously. In order to relate the count rate to the input spectrum we introduce the *on-chip device efficiency* in analogy to the OCDE of individual detectors. It compares the number of photons incident on the AWG to the number of photons detected. By measuring the optical power transmitted through the reference port, we directly obtain the optical power entering the AWG. Comparing this power to the detector count rate, we extract the on-chip device efficiency. The coupling losses incurred at the grating couplers are accounted for by the procedure outlined in annex A3. The compiled device efficiency curves are shown in Figure 5.2-3. As can be seen, the individual transmission bands are preserved, but they are blue-shifted by 1 nm relative to the room temperature transmission which is overlaid as grey dotted lines. This shift arises due to the thermo-optic effect in Si_3N_4 which causes the refractive index to change with temperature. The AWG's overall functionality is, however, not impaired by this effect. Combining the results of all eight channels an overall device efficiency of $(18.93 \pm 6.21)\%$ is obtained.

Alternatively, the device efficiency can be found by combining the components' previously assessed efficiencies. The detectors' OCDEs were found to be $(51.89 \pm 6.66)\%$ and the AWG's insertion loss was $(35.65 \pm 8.81)\%$. The combined efficiency, i.e. the device efficiency, is given by the product of its components which yields $(18.50 \pm 5.15)\%$. This is in very good agreement with the approach outlined above and is thus interpreted as confirmation.

It should be noted that due to the application of SPDs as direct on-chip read-out, the channel cross-talk has improved to 17.69 dB from the previously measured 12.87 dB. This is predominantly due to the reduced noise in our integrated SNSPDs. The insertion loss uniformity has improved

²¹ This fabrication run required an oxygen plasma cleaning step to remove residual resist. Apparently this adversely affected the detectors.

slightly to 3.65 dB. This change is, however, mainly due to variations in the grating coupler transmission.

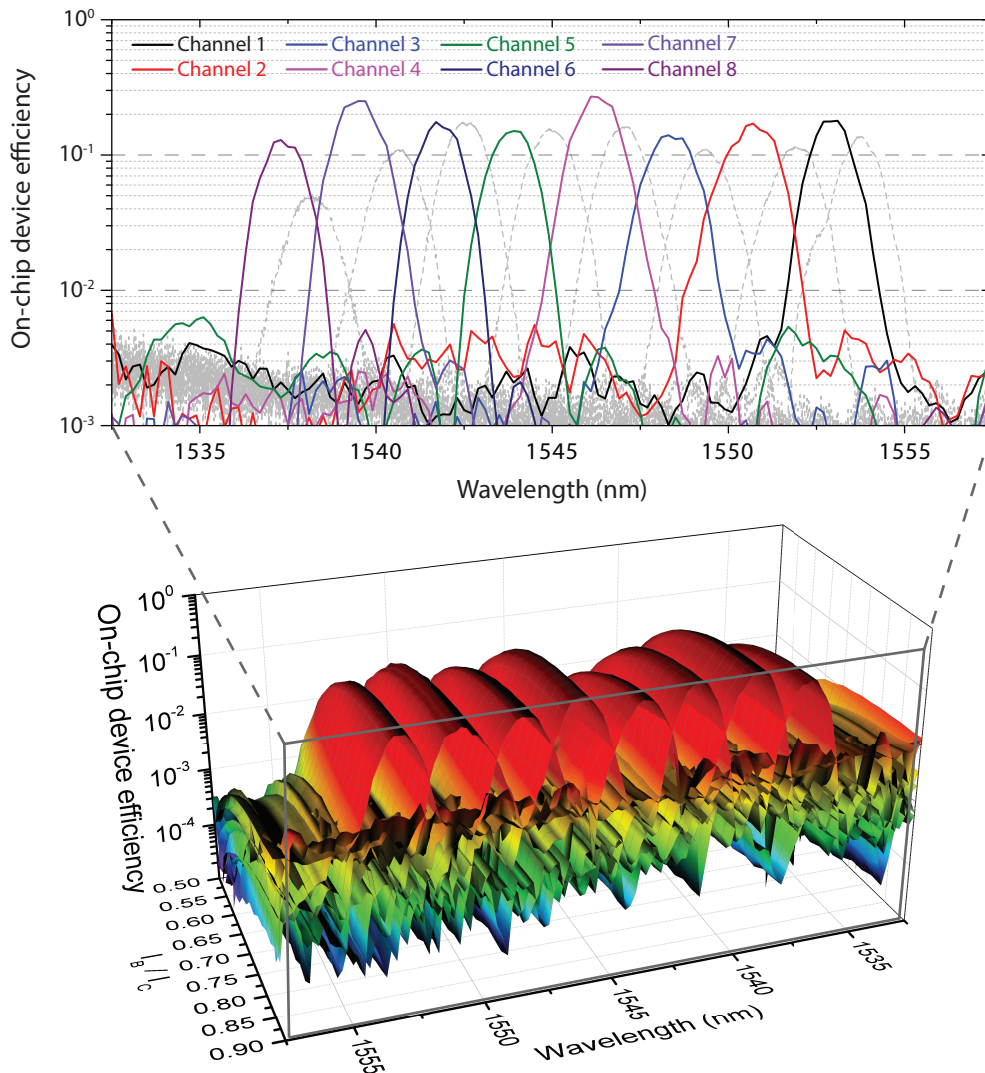


Figure 5.2-3: Efficiency curves of all detector channels. Top: device efficiency curves measured at a bias current of 90% of the critical current. The grey dotted lines represent the optical transmission spectrum obtained at room temperature showing a thermal shift of 1 nm. Bottom: device efficiency as a function of wavelength and bias current.

In general, above results show that an AWG combined with integrated SNSPDs can potentially be employed as a multi-channel single-photon receiver in photonic networks. In a broader context, it demonstrates the possibility to seamlessly integrate multiple integrated SNSPDs with nanophotonic circuitry. Although only eight parallel detectors were realized here, many more can be embedded on the same platform.

5.3 SINGLE-PHOTON SPECTROMETER AT 740 NM

In the following we will expand the utilization of the AWG – integrated SNSPD combination to a metrological application in which the fluorescence spectrum and lifetime of SiV centers will be measured. Such an experiment not only demonstrates the detectors' superior spectroscopic

capabilities, but it also shows the compatibility with SiV centers which are promising candidates for single-photon sources. This is particularly interesting in light of the previously demonstrated feasibility to integrate integrated SNSPDs on diamond [194], [195].

5.3.1 SILICON VACANCIES (SiVs)

The SiV is one of many possible color centers hosted in a diamond lattice. They are referred to as ‘color centers’ as their presence can lend the crystal a characteristic color. On a microscopic scale, SiVs are crystal lattice defects which consist of a silicon impurity and two adjacent vacancies [225] (see inset in Figure 5.3-1). They frequently occur in diamond layers which are grown by chemical vapor deposition (CVD) due to the use of silicon substrates. The presence of SiVs perturbs the optical properties of pure diamond. In particular, the wide bandgap 5.5 eV which provides for broad spectral transparency is interspersed by an additional absorption line. Upon excitation to a higher electronic state, it can directly relax under the emission of a photon producing a sharp, characteristic emission line referred to as zero-phonon line (ZPL). Alternatively, the substitutional silicon atom can exchange energy with the lattice which gives rise to vibronic sub-bands in the emission spectrum. Figure 5.3-1 shows the pertinent spectra measured at our specimen which is an aqueous solution of diamond nanocrystals. The crystals were fabricated at the Fraunhofer Institute of Applied Solid State Physics in Freiburg, Germany. They were designed specifically to host multiple SiV color centers. The absorption curve was measured with a Cary 5000 UV-Vis-NIR spectrophotometer with the nanocrystals suspended in an aqueous solution. The emission spectrum was measured upon cw excitation at 532 nm in a self-made confocal microscope which will be described in detail in the following section. The nanocrystals were drop cast onto a microscope slide and dried out for the fluorescence measurement. The general interest in SiVs stems from their proposed capability to act as single-photon sources [226]. If spatially isolated inside a transparent diamond matrix, they can be individually excited thus emitting a single photon upon relaxation. Our sample contained numerous SiV centers per nanocrystal. The emission therefore contained numerous photons.

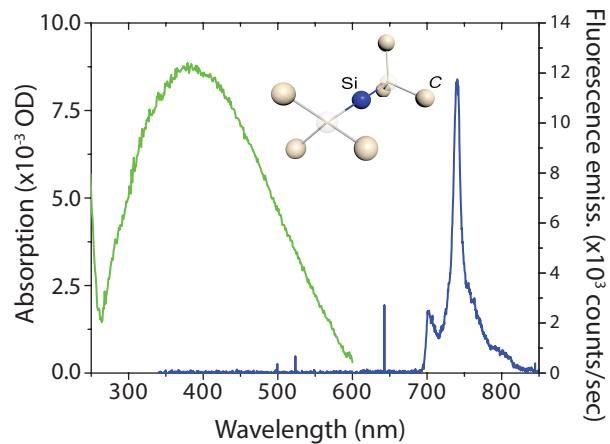


Figure 5.3-1: Absorption (green) and emission (blue) spectrum of SiV. Inset: 3D crystal structure of SiV center comprising Si atom surrounded by two vacancies

5.3.2 SCANNING CONFOCAL MICROSCOPE

The confocal microscope described in this section is used for the simultaneous excitation of the SiV center specimen and the collection of its fluorescence light. Its modular construction also allows for pulsed excitation by another laser source which enables fluorescence lifetime measurements.

5.3.2.1 BASIC CONCEPT

Confocal microscopy is a high contrast optical imaging technique with depth selectivity which is mostly used to analyze fluorescent specimens. The standard principle of operation is depicted in Figure 5.3-2. A light source is used to irradiate and thereby optically excite the sample (purple lines). The fluorescence light (red lines) which is emitted upon relaxation at a longer wavelength is collected by the same focusing optics which were used for the excitation. A dichroic mirror between the light source and the focusing optics transmits the excitation wavelength but reflects the fluorescence light in order to be collected by a photodetector. The imaging capability can be substantially enhanced by the addition of a pinhole which blocks any light from outside the focal volume. By inserting a pinhole at a position in front of the photodetector which is *conjugate* to the focal point on the sample, any light which does not originate from those conjugate focal (*confocal*) points will not pass through the pinhole (green dashed lines) and is thus not detected.

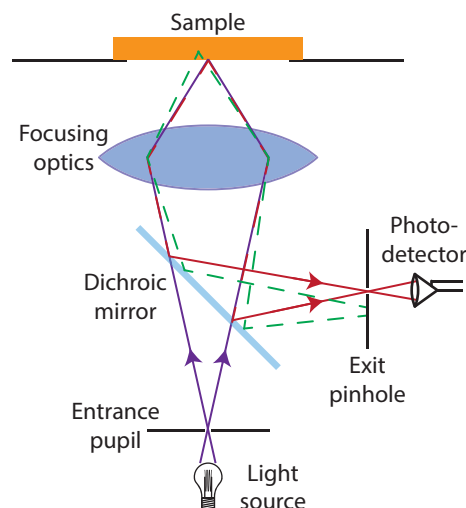


Figure 5.3-2: Schematic illustration of the working principle of a confocal microscope

5.3.2.2 IMPLEMENTATION

The specific implementation of our confocal microscope is shown in Figure 5.3-3. It consists of two separate sections: the upper section is a conventional optical microscope for sample inspection and coarse positioning, and the lower section constitutes the actual confocal microscope. The sample is situated on a 2D translation stage at the interface between the two sections of the setup.

The optical microscope in the upper level uses red light from a LED to illuminate the sample through a 10x objective lens. Reflections from the sample are collected by the same lens and guided toward a CCD camera. A 50:50 beam splitter is used to separate the reflection from the illumination.

The lower section uses a cw laser²² (Thorlabs CPS532) emitting light at 532 nm to excite the sample through a 100x oil

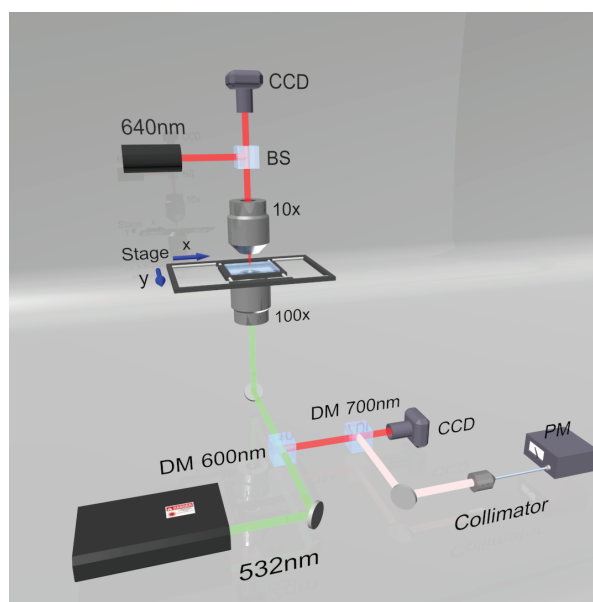


Figure 5.3-3: Illustration of scanning confocal microscope

²² It should be noted that use of the 532 nm cw laser instead of the 440 nm pulsed laser which was used later for the fluorescence lifetime measurement was merely a matter of equipment availability and convenience. The results are unaffected by the choice of excitation wavelength as can be seen in Figure 5.3-1.

immersion objective lens with a numerical aperture of 1.4. The lens collects three wavelengths in the reverse direction: the reflected 532 nm, the transmitted 640 nm from the illuminating LED and the emitted fluorescence at 740 nm in case of SiVs. The excitation light is filtered out by a dichroic mirror with 600 nm cut-off. The illuminating (640 nm) and emitted light (740 nm) are reflected while the 532 nm excitation is transmitted back toward the laser. A second dichroic mirror with cut-off at 700 nm separates the illuminating light from the fluorescence and routes it toward a CCD camera. The emitted fluorescence light is guided onward to a fiber-coupled collimator which is connected to more advanced optical read-out equipment. The pinhole in our setup is mimicked by the optical fiber entrance facet which the collimator focuses into. If properly aligned, only light which is in focus on the sample will couple into the fiber. The entire optical setup is enclosed in a black metal case which provides shielding from ambient radiation.

By collecting the 640 nm illumination light in reflection and transmission through the 10x and 100x lenses, respectively, using the camera feedback highly accurate positioning of the sample is enabled. By moving the translation stage during data acquisition, 2D topographical scans of the specimen can be created. The excitation laser can be easily exchanged – for fluorescence lifetime measurements a pulsed 440 nm laser (ALS PiLas PiL044X) will be used instead. Although the optical analysis can be done by any fiber coupled device, we will clearly use our detector-integrated AWG.

5.3.3 SPECTROMETER CHARACTERIZATION

Here we will perform the characterization for the 740 nm AWG and its integrated SNSPDs. Slight adjustments in the characterization are necessary due to differences in the utilized equipment.

5.3.3.1 OPTICAL CHARACTERIZATION

We follow the same procedure as with the foregoing AWG. The optical transmission is obtained and the salient parameters – insertion loss, insertion loss uniformity, and channel cross-talk – are determined. Due to the change in wavelength regime, we use a white light continuum laser instead of a tunable, monochromatic laser. The transmitted spectrum is analyzed using a modular spectrometer (Ocean Optics JAZ). The measured spectrum is depicted in Figure 5.3-4. It immediately appears that the signal to noise ratio toward the edges of the displayed spectrum drastically decreases. This is due to the spectral limitation of the employed grating couplers, which curtails the

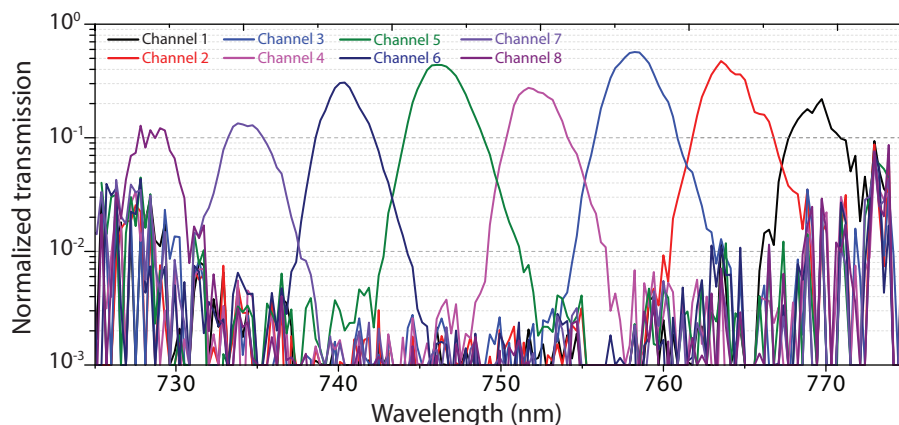


Figure 5.3-4: Optical transmission spectrum of AWG with integrated SNSPD

insertion loss and, particularly, the insertion loss uniformity. It does, however, not represent a fundamental obstacle for the experiment and will be mitigated substantially by the use of the integrated SNSPDs. The transmission bands agree well with the design parameters of 45 nm transmission window and 5.6 nm channel width (FWHM). The transmission level measured at the AWG is $(26.33 \pm 17.44)\%$ which corresponds to an insertion loss of 5.79 dB. The insertion loss uniformity is 10.79 dB and the channel cross-talk 12.73 dB.

5.3.3.2 DETECTOR CHARACTERIZATION

A detector characterization at exactly 740 nm was not possible due to the lack of a suitable laser sources at this wavelength. Instead a tunable cw laser, set to 765 nm, was used for the OCDE measurement. The grating coupler transmission is reduced at 765 nm relative to 740 nm, yet it is sufficiently transmissive to perform OCDE measurements. The timing jitter measurement was performed at 440 nm using a pulsed laser source (ALS PiLas PiL044X) which produces picosecond pulses at 10 MHz repetition rate. The utilized grating couplers possess a higher transmission order

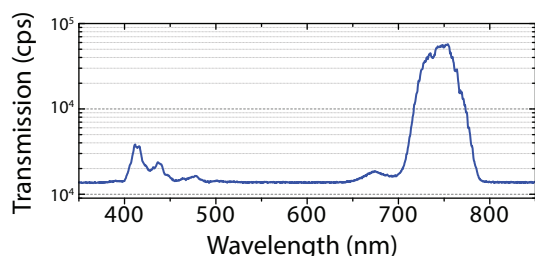


Figure 5.3-5: Optical transmission spectrum of GC designed for 740 nm showing higher order mode at 430 nm

around 430 nm (see Figure 5.3-5) which allows for light insertion for the timing jitter measurement.

The characteristic detector parameters are again determined by the methods and procedures outlined in section 3.5. The detectors' OCDE was found to be at a good level of $(78.02 \pm 11.92)\%$. The timing jitter and decay time are at the usual levels of (41.01 ± 2.31) ps and (2.98 ± 0.32) ns, respectively.

5.3.4 RESULTS AND DISCUSSION

The components described above combine to a highly sensitive, extremely fast detector array which is able to spectrally discriminate photons on eight channels ranging from 720 nm to 775 nm. In combination with the scanning confocal microscope, an extremely high level of experimental fidelity is achieved in a single device. The spectrometer's on-chip device efficiency, defined as the product of the components' detection efficiency and insertion loss, combines to $(20.54 \pm 13.96)\%$.

5.3.4.1 CONFOCAL SPECTROSCOPY

SiV center-containing diamond nanocrystals in a highly dilute aqueous solution are drop-cast onto a microscope slide. The sample is dried out in order to obtain small clusters of diamond nanocrystals in fixed positions, which can be spectroscopically analyzed. The sample is mounted in the self-built confocal microscope described above and a nanocrystal cluster of adequate size ($20 \times 10 \mu\text{m}^2$) is selected for examination. The specimen is excited by a cw laser diode (Thorlabs CPS532) at 532 nm with 4.5 mW output power, the emitted fluorescence light is collected and coupled into an optical fiber which guides the light into our cryostat onto the AWG chip. The wavelength components are separated on-chip and individual spectral fractions are detected by the integrated SNSPDs. The measured count rates on the individual channels are adjusted for the input grating coupler and are depicted in Figure 5.3-6 alongside the SiV fluorescence spectrum. As can be seen the count rates follow the same trend as the fluorescence signal with a clear peak at 740 nm. The measurement with

our on-chip spectrometer thereby allows for an accurate reconstruction of the input fluorescence spectrum.

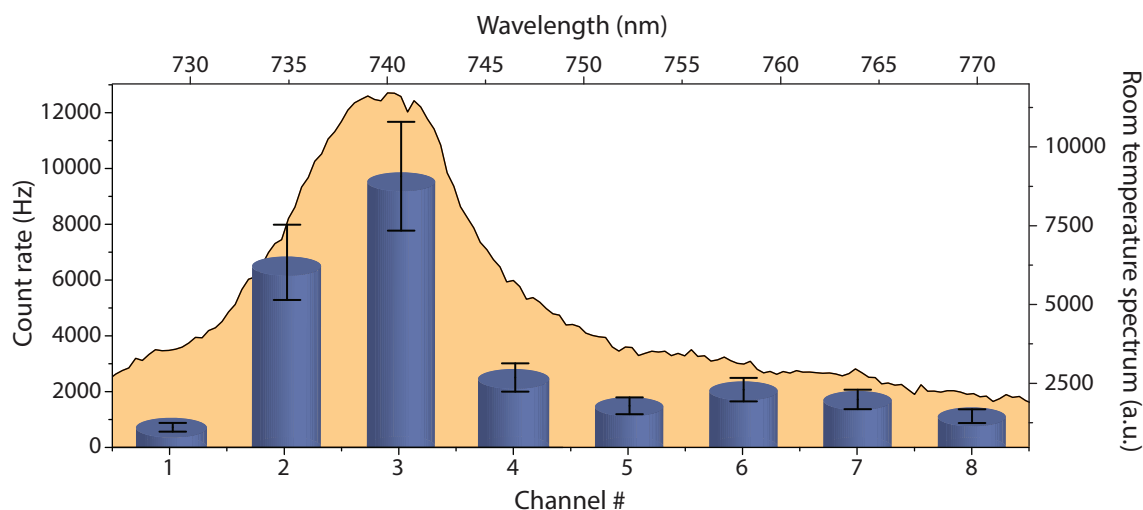


Figure 5.3-6: Count rate spectrum for all measured AWG channels (purple bars) and overlaid SiV fluorescence spectrum (black solid line with orange solid fill)

The 2D translation stage of our microscope allows for a spectrally and spatially resolved examination of the cluster. By scanning the sample in 200 nm steps across the cluster area, the graph shown in Figure 5.3-7 is produced. The scan directly shows one of the benefits of employing integrated SNSPDs instead of conventional spectrometers: next to spectral resolution and sensitivity on the single-photon level, the scan exhibits a background signal of almost zero. Far from the nanodiamond cluster the signal reduces to a count rate below 10 Hz. This count rate is mostly due to residual ambient light and black-body radiation entering the system.

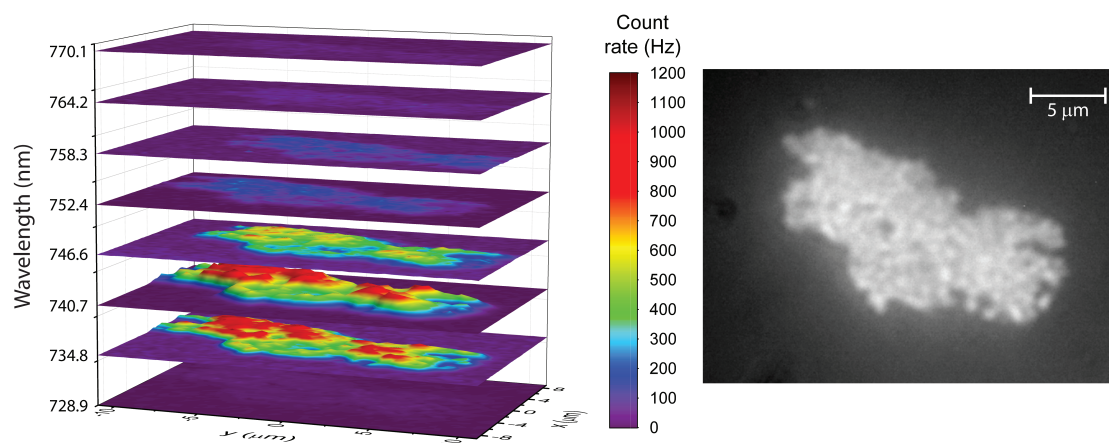


Figure 5.3-7: Left: 2D fluorescence map of nanodiamond cluster. The different levels represent the AWG channels which correspond to the indicated wavelengths. Right: optical microscope image of nanodiamond cluster

5.3.4.2 FLUORESCENCE LIFETIME IMAGING

In combination with advanced timing equipment (PicoHarp 300) and a pulsed laser source (ALS PiL044X), the specimen's fluorescence lifetime can be measured. The setup is very similar to the timing jitter measurement (see section 3.5.5). The laser produces 50 ps pulses at a repetition rate of 10 MHz to excite the sample inside the confocal microscope. The emission is collected as before and

sent to the spectrometer inside the cryostat. We collect delay time histogram data in a start-stop triggered measurement. The laser's trigger output is utilized as a start trigger and the electrical output signal of channel three (centered at 740.7 nm) of the spectrometer is used as stop trigger. The relative time difference between the two trigger signals is recorded. The obtained histogram data is fitted with a single exponential in order to extract the SiV centers' decay time of 471 ps. Owing to the 2D translation stage of the confocal microscope an entire FLIM can be generated by scanning over the cluster area. Most importantly, the collected data – fluorescence spectrum, fluorescence lifetime, and the 2D maps thereof – can all be collected in a single scan. The FLIM is shown in Figure 5.3-8.

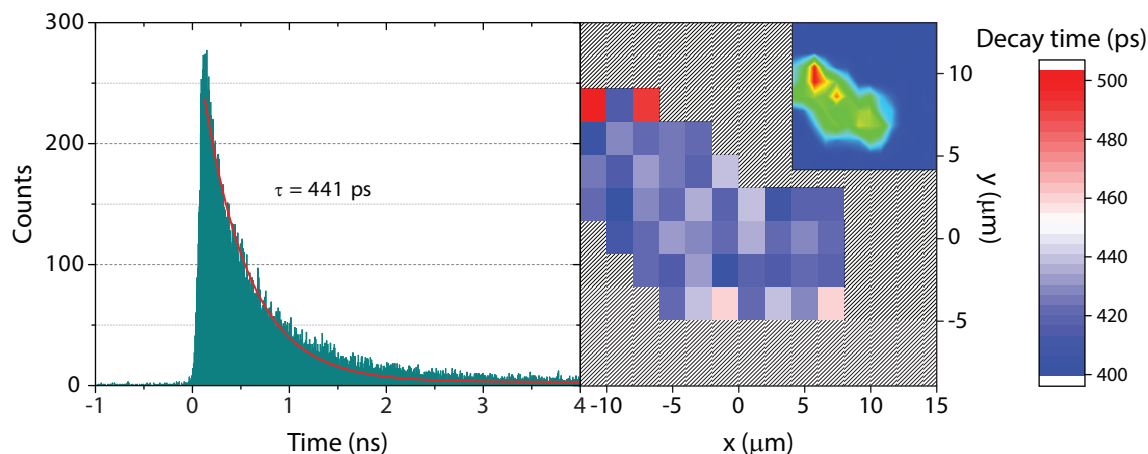


Figure 5.3-8: Left: SiV decay time histogram including single exponential fit (red solid line). Right: FLIM of nanodiamond cluster. Inset: intensity scan of the same cluster acquired simultaneously.

The accuracy of such a fluorescence lifetime measurement depends heavily on the timing accuracy of the employed equipment. The laser's timing jitter is as low as 2 ps and the integrated SNSPDs' timing jitter was found at 41 ps which ensures high timing accuracy.

5.4 CONCLUDING REMARKS

In this chapter we demonstrated how integrated SNSPDs can be integrated with advanced nanophotonic circuitry. Two AWGs were developed and employed as spectrometers in combination with multiple integrated SNSPDs. The realized devices enable wavelength discrimination on a single-photon level. The AWGs were designed for 1550 nm in the NIR and 740 nm in the visible. Identical detector designs were shown to operate flawlessly in both wavelength regimes which are over an octave apart. In the visible, the fluorescence emitted from silicon vacancies in diamond nanocrystals was spectrally resolved. The detector's superior timing characteristics simultaneously enable fluorescence lifetime measurements using the same spectrometer device.

With regard to future developments, the realized devices show that current scalability-related limitations can be reduced or completely eliminated by employing integrated SNSPDs. This is of particular interest to quantum information applications which will also benefit from the detectors' high efficiency and outstanding timing precision. QKD applications can certainly be improved through the implementation of integrated SNSPDs and perhaps even the long standing goal of LOQC can be brought into closer reach.

6 CONCLUSION AND OUTLOOK

In this thesis potentials and capabilities of integrated SNSPDs on Si_3N_4 have been demonstrated. At the end of each chapter, a brief summary and a discussion were included which relate the chapter to the broader context of the field. Here the key results will be summarized followed by an outlook to future research in this field.

The work for this thesis was motivated by the need for photonic integration of quantum optical circuitry as outlined in the introduction. Single-photon detectors constitute one of the key components in such circuits and they have recently been successfully integrated. The integrated detector is based on the superconducting nanowire single-photon detector (SNSPD) which in its non-integrated form exhibits extraordinary detection performance in all categories, except its detection efficiency. The short distance over which photons are absorbed limits the detection efficiency. Integration resolves this issue by enabling absorption over a longer distance in a travelling-wave geometry. Initial implementations show significantly enhanced detection efficiency while the usual high levels of timing accuracy are maintained. The work performed for this thesis connects at this point and expands the detection performance further.

In chapter 3, several integrated SNSPDs were demonstrated. One particular model reaches a detection efficiency of 84% and exhibits a long detection plateau which enables reductions in the bias current to levels at which the noise-equivalent power reaches the $10^{-19} \text{ WHz}^{-1/2}$ mark which corresponds to a dark count rate of $< 10 \text{ Hz}$. It was discovered that this dark count level can be reduced by shielding the detector from spurious black-body radiation.

It was furthermore found that the current notion of a kinetic inductance-limited count rate maximum must be revisited. Oscilloscope traces clearly show the possibility of photon registrations during the voltage decay of the previous registration. Additional experimental investigation is needed, but it appears that single-photon detection at count rates beyond the 1 GHz mark is possible.

Moreover, a bias current-dependent contribution to the timing jitter could be identified. At low bias currents the voltage pulse which follows the absorption of a photon is shallow and thus susceptible to noise contributions which introduce additional temporal uncertainties in the pulse's rising edge. These contributions are significantly reduced for steeper rising edges at stronger bias currents. Limitations by low critical currents, however, curtail the minimally achievable timing jitter. This underlines the need for high critical currents which can only be ensured by flawless fabrication routines.

In chapter 4 the detector response is analyzed using a technique referred to as quantum detector tomography. It is found that the fabricated detectors exhibit detection regimes in which they are

insensitive to single photons, but sensitive to a larger number. The detection regimes are accessed by reducing the bias current below the threshold current at which single-photon detection becomes possible. For such current settings, a larger number of photons is required to induce vortex nucleation which leads to the formation of a normal-conducting barrier. Therefore, the bias current provides a means to reduce the detector's sensitivity to a larger number of photons. This is different from photon-number resolution which inherently discriminates the exact number of photons. In the described detection mode merely a lower bound on the detectable photon number is introduced. Nevertheless, this concept offers the potential to respond only to specific photon states in quantum optical circuitry which is attractive for the counting of exotic photon states.

In chapter 5, fully scalable integration of SNSPDs was demonstrated by realizing multiple detectors within a single integrated photonic circuit. Arrayed waveguide gratings (AWGs) which are commonly used as de-multiplexer in wavelength-division multiplexed (WDM) photonic circuitry were combined with multiple SNSPDs to realize a fully integrated single-photon spectrometer. Two designs were realized, one for the visible regime at 740 nm and one for the near-infrared (NIR) at 1550 nm. The NIR design showed single-photon sensitivity on all eight channels spanning a spectral range of 16 nm. Such a device offers potential for high-bandwidth quantum communication. The 740 nm version was used in combination with a self-built confocal microscope in order to spectrally, temporally, and spatially resolve the fluorescence of silicon vacancy color centers in diamond. The combination of those three dimensions is attractive for single-photon sensing applications and offers the possibility for cross-correlative single-photon imaging on multiple wavelengths. Ultimately, the realization of numerous integrated SNSPDs within a single photonic circuit demonstrates the feasibility of large-scale quantum optical integration. These are key requirements for more advanced applications such as high-bandwidth quantum communication, quantum key distribution (QKD), and the long standing goal of linear optical quantum computing (LOQC).

On a broader scale, the integrated SNSPDs demonstrated in this thesis offer attractive characteristics for classical and quantum optical technologies. While classical applications such as optical coherence tomography or optical time domain reflectometry benefit from the improved signal-to-noise ratio provided by integrated SNSPDs [227], [228], quantum applications in quantum communication, metrology and computing crucially depend on the detector's low-noise performance and minimal timing jitter [8], [58], [59], [62], [229]–[231]. Yet, while the results in detection performance as presented in this thesis are certainly superior to most of the established SPD technologies, in most practical contexts expectations for near-unity detection efficiency have to be curbed due to photon loss resulting from imperfect coupling to the on-chip circuitry. At present, this issue pertains to classical applications as well as quantum optical technology. In the absence of fully integratable single-photon sources, optical implementations of quantum information schemes require external sources, which limits the integrated approach and underlines the need for scalable on-chip single-photon sources.

Integrated SNSPDs have been demonstrated on various substrates. In the search for integratable single-photon sources, substrates which possess an $\chi^{(2)}$ nonlinearity could potentially lead the way to multiplexed on-chip down-conversion sources [232]. This concept has previously been demonstrated in waveguides made from periodically poled lithium niobate [233]. SNSPDs on lithium niobate have already been demonstrated under normal incidence and simulated in the waveguide-integrated configuration [57]. A similar argument applies to the silicon nitride platform which was utilized in this thesis. The recent demonstration of a surface $\chi^{(2)}$ effect [188] may hold potential for

integrated single-photon sources on silicon nitride which falls well in line with the work demonstrated in this thesis. The development of the combined integration of single-photon sources and SNSPDs is an immediate goal which will further enhance practicality and scalability of quantum photonic implementations.

7 REFERENCES

- [1] M. Planck, "Ueber das Gesetz der Energieverteilung im Normalspectrum," *Ann. Phys.*, vol. 309, no. 3, pp. 553–563, 1901.
- [2] A. Einstein, "Über einen die Erzeugung und Verwandlung des Lichtes betreffenden heuristischen Gesichtspunkt," *Ann. Phys.*, vol. 322, no. 6, pp. 132–148, 1905.
- [3] R. P. Feynman, "Simulating physics with computers," *Int. J. Theor. Phys.*, vol. 21, no. 6–7, pp. 467–488, Jun. 1982.
- [4] R. P. Feynman, "Quantum mechanical computers," *Found. Phys.*, vol. 16, no. 6, pp. 507–531, Jun. 1986.
- [5] D. Bouwmeester, A. Ekert, and A. Zeilinger, Eds., *The Physics of Quantum Information*. Berlin, Heidelberg: Springer Berlin Heidelberg, 2000.
- [6] D. Deutsch, "Quantum Theory, the Church-Turing Principle and the Universal Quantum Computer," *Proc. R. Soc. A Math. Phys. Eng. Sci.*, vol. 400, no. 1818, pp. 97–117, Jul. 1985.
- [7] P. Benioff, "The computer as a physical system: A microscopic quantum mechanical Hamiltonian model of computers as represented by Turing machines," *J. Stat. Phys.*, vol. 22, no. 5, pp. 563–591, May 1980.
- [8] N. Gisin, G. Ribordy, W. Tittel, and H. Zbinden, "Quantum cryptography," *Rev. Mod. Phys.*, vol. 74, no. 1, pp. 145–195, Mar. 2002.
- [9] A. K. Ekert, "Quantum cryptography based on Bell's theorem," *Phys. Rev. Lett.*, vol. 67, no. 6, pp. 661–663, Aug. 1991.
- [10] C. H. Bennett and G. Brassard, "Quantum cryptography: Public key distribution and coin tossing," in *Int. Conf. Computers, Systems & Signal Processing, Bangalore, India*, 1984, pp. 175–179.
- [11] C. H. Bennett and G. Brassard, "Quantum cryptography: Public key distribution and coin tossing," *Theor. Comput. Sci.*, vol. 560, pp. 7–11, Dec. 2014.
- [12] N. Gisin and R. Thew, "Quantum communication," *Nat. Photonics*, vol. 1, no. 3, pp. 165–171, Mar. 2007.
- [13] C. Bennett and S. Wiesner, "Communication via one- and two-particle operators on Einstein-Podolsky-Rosen states," *Phys. Rev. Lett.*, vol. 69, no. 20, pp. 2881–2884, 1992.
- [14] C. H. Bennett, G. Brassard, C. Crépeau, R. Jozsa, A. Peres, and W. K. Wootters, "Teleporting an unknown quantum state via dual classical and Einstein-Podolsky-Rosen channels," *Phys. Rev. Lett.*, vol. 70, no. 13, pp. 1895–1899, Mar. 1993.

- [15] M. A. Nielsen and I. L. Chuang, *Quantum Computation and Quantum Information: 10th Anniversary Edition*, 10th Anniv. New York: Cambridge University Press, 2011.
- [16] M. Oxborrow and A. G. Sinclair, "Single-photon sources," *Contemp. Phys.*, vol. 46, no. 3, pp. 173–206, May 2005.
- [17] A. J. Shields, "Semiconductor quantum light sources," *Nat. Photonics*, vol. 1, no. 4, pp. 215–223, Apr. 2007.
- [18] S. Strauf, "Quantum optics: Towards efficient quantum sources," *Nat. Photonics*, vol. 4, no. 3, pp. 132–134, Mar. 2010.
- [19] M. Fox, *Quantum Optics: An Introduction*. Oxford University Press, 2006.
- [20] S. Arora and B. Barak, *Computational Complexity: A Modern Approach*, no. January. Cambridge University Press, 2009.
- [21] J. S. Bell, "On the Einstein-Podolsky-Rosen paradox," *Physics (College Park, Md.)*, vol. 1, no. 3, pp. 195–200, 1964.
- [22] A. Einstein, B. Podolsky, and N. Rosen, "Can Quantum-Mechanical Description of Physical Reality Be Considered Complete?," *Phys. Rev.*, vol. 47, no. 10, pp. 777–780, May 1935.
- [23] S. J. Freedman and J. F. Clauser, "Experimental Test of Local Hidden-Variable Theories," *Phys. Rev. Lett.*, vol. 28, no. 14, pp. 938–941, Apr. 1972.
- [24] A. Aspect, J. Dalibard, and G. Roger, "Experimental Test of Bell's Inequalities Using Time-Varying Analyzers," *Phys. Rev. Lett.*, vol. 49, no. 25, pp. 1804–1807, Dec. 1982.
- [25] A. Aspect, P. Grangier, and G. Roger, "Experimental Realization of Einstein-Podolsky-Rosen-Bohm Gedankenexperiment : A New Violation of Bell's Inequalities," *Phys. Rev. Lett.*, vol. 49, no. 2, pp. 91–94, Jul. 1982.
- [26] G. Weihs, T. Jennewein, C. Simon, H. Weinfurter, and A. Zeilinger, "Violation of Bell's Inequality under Strict Einstein Locality Conditions," *Phys. Rev. Lett.*, vol. 81, no. 23, pp. 5039–5043, Dec. 1998.
- [27] C.-Y. Lu, X.-Q. Zhou, O. Gühne, W.-B. Gao, J. Zhang, Z.-S. Yuan, A. Goebel, T. Yang, and J.-W. Pan, "Experimental entanglement of six photons in graph states," *Nat. Phys.*, vol. 3, no. 2, pp. 91–95, Feb. 2007.
- [28] P. Walther, K. J. Resch, T. Rudolph, E. Schenck, H. Weinfurter, V. Vedral, M. Aspelmeyer, and A. Zeilinger, "Experimental one-way quantum computing," *Nature*, vol. 434, no. 7030, pp. 169–176, Mar. 2005.
- [29] D. Bouwmeester, J.-W. Pan, K. Mattle, M. Eibl, H. Weinfurter, and A. Zeilinger, "Experimental quantum teleportation," *Nature*, vol. 390, no. 6660, pp. 575–579, Dec. 1997.
- [30] S. Kako, C. Santori, K. Hoshino, S. Götzinger, Y. Yamamoto, and Y. Arakawa, "A gallium nitride single-photon source operating at 200 K," *Nat. Mater.*, vol. 5, no. 11, pp. 887–892, Nov. 2006.
- [31] A. J. Bennett, D. C. Unitt, P. Atkinson, D. A. Ritchie, and A. J. Shields, "High performance single photon sources from photolithographically defined pillar microcavities," *Opt. Express*, vol. 13, no. 1, p. 50, 2005.

- [32] X. Brokmann, E. Giacobino, M. Dahan, and J. P. Hermier, "Highly efficient triggered emission of single photons by colloidal CdSe/ZnS nanocrystals," *Appl. Phys. Lett.*, vol. 85, no. 5, p. 712, 2004.
- [33] S. G. Lukishova, A. W. Schmid, A. J. McNamara, R. W. Boyd, and C. R. Stroud, "Room temperature single-photon source: single-dye molecule fluorescence in liquid crystal host," *IEEE J. Sel. Top. Quantum Electron.*, vol. 9, no. 6, pp. 1512–1518, Nov. 2003.
- [34] R. Alléaume, F. Treussart, J.-M. Courty, and J.-F. Roch, "Photon statistics characterization of a single-photon source," *New J. Phys.*, vol. 6, no. 04, pp. 85–85, Jul. 2004.
- [35] S. G. Lukishova, A. W. Schmid, C. M. Supranowitz, N. Lippa, A. J. McNamara, R. W. Boyd, and C. R. Stroud, "Dye-doped cholesteric-liquid-crystal room-temperature single-photon source," *J. Mod. Opt.*, vol. 51, no. 9–10, pp. 1535–1547, Jun. 2004.
- [36] J. McKeever, "Deterministic Generation of Single Photons from One Atom Trapped in a Cavity," *Science (80-.)*, vol. 303, no. 5666, pp. 1992–1994, Mar. 2004.
- [37] M. Hijlkema, B. Weber, H. P. Specht, S. C. Webster, A. Kuhn, and G. Rempe, "A single-photon server with just one atom," *Nat. Phys.*, vol. 3, no. 4, pp. 253–255, Apr. 2007.
- [38] M. Keller, B. Lange, K. Hayasaka, W. Lange, and H. Walther, "Continuous generation of single photons with controlled waveform in an ion-trap cavity system," *Nature*, vol. 431, no. 7012, pp. 1075–1078, Oct. 2004.
- [39] A. Beveratos, R. Brouri, T. Gacoin, A. Villing, J.-P. Poizat, and P. Grangier, "Single Photon Quantum Cryptography," *Phys. Rev. Lett.*, vol. 89, no. 18, p. 187901, Oct. 2002.
- [40] C. Santori, D. Fattal, J. Vucković, G. S. Solomon, and Y. Yamamoto, "Indistinguishable photons from a single-photon device," *Nature*, vol. 419, no. 6907, pp. 594–597, 2002.
- [41] R. B. Patel, A. J. Bennett, I. Farrer, C. A. Nicoll, D. A. Ritchie, and A. J. Shields, "Two-photon interference of the emission from electrically tunable remote quantum dots," *Nat. Photonics*, vol. 4, no. 9, pp. 632–635, Sep. 2010.
- [42] S. Olmschenk, D. N. Matsukevich, P. Maunz, D. Hayes, L.-M. Duan, and C. Monroe, "Quantum Teleportation Between Distant Matter Qubits," *Science (80-.)*, vol. 323, no. 5913, pp. 486–489, Jan. 2009.
- [43] P. Maunz, D. L. Moehring, S. Olmschenk, K. C. Younge, D. N. Matsukevich, and C. Monroe, "Quantum interference of photon pairs from two remote trapped atomic ions," *Nat. Phys.*, vol. 3, no. 8, pp. 538–541, Aug. 2007.
- [44] T. Chanelière, D. N. Matsukevich, S. D. Jenkins, S.-Y. Lan, R. Zhao, T. a B. Kennedy, and A. Kuzmich, "Quantum Interference of Electromagnetic Fields from Remote Quantum Memories," *Phys. Rev. Lett.*, vol. 98, no. 11, p. 113602, Mar. 2007.
- [45] J. Beugnon, M. P. A. Jones, J. Dingjan, B. Darquié, G. Messin, A. Browaeys, and P. Grangier, "Quantum interference between two single photons emitted by independently trapped atoms," *Nature*, vol. 440, no. 7085, pp. 779–782, Apr. 2006.
- [46] M. A. Broome, A. Fedrizzi, S. Rahimi-Keshari, J. Dove, S. Aaronson, T. C. Ralph, and A. G. White, "Photonic boson sampling in a tunable circuit," *Science (80-.)*, vol. 339, no.

- 6121, pp. 794–8, Feb. 2013.
- [47] G. N. Gol'tsman, O. Okunev, G. Chulkova, a. Lipatov, a. Semenov, K. Smirnov, B. Voronov, a. Dzardanov, C. Williams, and R. Sobolewski, "Picosecond superconducting single-photon optical detector," *Appl. Phys. Lett.*, vol. 79, no. 6, p. 705, 2001.
- [48] R. H. Hadfield, "Single-photon detectors for optical quantum information applications," *Nat. Photonics*, vol. 3, no. 12, pp. 696–705, Dec. 2009.
- [49] M. D. Eisaman, J. Fan, a Migdall, and S. V Polyakov, "Invited review article: Single-photon sources and detectors.," *Rev. Sci. Instrum.*, vol. 82, no. 7, p. 071101, Jul. 2011.
- [50] P. Kapusta, M. Wahl, and R. Erdmann, *Advanced Photon Counting*, vol. 15. Cham: Springer International Publishing, 2015.
- [51] G. N. Gol'tsman, K. Smirnov, P. Kouminov, B. Voronov, N. Kaurova, V. Drakinsky, J. Zhang, A. Verevkin, and R. Sobolewski, "Fabrication of nanostructured superconducting single-photon detectors," *IEEE Trans. Applied Supercond.*, vol. 13, no. 2, pp. 192–195, Jun. 2003.
- [52] X. Hu, C. W. Holzwarth, D. Masciarelli, E. A. Dauler, and K. K. Berggren, "Efficiently Coupling Light to Superconducting Nanowire Single-Photon Detectors," *IEEE Trans. Appl. Supercond.*, vol. 19, no. 3, pp. 336–340, Jun. 2009.
- [53] J. P. Sprengers, A. Gaggero, D. Sahin, S. Jahanmirinejad, G. Frucci, F. Mattioli, R. Leoni, J. Beetz, M. Lerner, M. Kamp, S. Höfling, R. Sanjines, and A. Fiore, "Waveguide superconducting single-photon detectors for integrated quantum photonic circuits," *Appl. Phys. Lett.*, vol. 99, no. 18, p. 181110, 2011.
- [54] G. Reithmaier, S. Lichtmannecker, T. Reichert, P. Hasch, K. Müller, M. Bichler, R. Gross, and J. J. Finley, "On-chip time resolved detection of quantum dot emission using integrated superconducting single photon detectors," *Sci. Rep.*, vol. 3, p. 1901, May 2013.
- [55] W. H. P. Pernice, C. Schuck, O. Minaeva, M. Li, G. N. Goltsman, A. V. Sergienko, and H. X. Tang, "High-speed and high-efficiency travelling wave single-photon detectors embedded in nanophotonic circuits," *Nat. Commun.*, vol. 3, p. 1325, Dec. 2012.
- [56] C. Schuck, W. H. P. Pernice, and H. X. Tang, "Waveguide integrated low noise NbTiN nanowire single-photon detectors with milli-Hz dark count rate.," *Sci. Rep.*, vol. 3, p. 1893, Jan. 2013.
- [57] M. G. Tanner, L. S. E. Alvarez, W. Jiang, R. J. Warburton, Z. H. Barber, and R. H. Hadfield, "A superconducting nanowire single photon detector on lithium niobate.," *Nanotechnology*, vol. 23, no. 50, p. 505201, Dec. 2012.
- [58] E. Knill, R. Laflamme, and G. Milburn, "A scheme for efficient quantum computation with linear optics," *Nature*, vol. 409, no. January, 2001.
- [59] H. Takesue, S. W. Nam, Q. Zhang, R. H. Hadfield, T. Honjo, K. Tamaki, and Y. Yamamoto, "Quantum key distribution over a 40-dB channel loss using superconducting single-photon detectors," *Nat. Photonics*, vol. 1, no. 6, pp. 343–348, Jun. 2007.
- [60] J. L. O'Brien, A. Furusawa, and J. Vučković, "Photonic quantum technologies," *Nat. Photonics*, vol. 3, no. 12, pp. 687–695, Dec. 2009.

- [61] C. M. Natarajan, A. Peruzzo, S. Miki, M. Sasaki, Z. Wang, B. Baek, S. Nam, R. H. Hadfield, and J. L. O'Brien, "Operating quantum waveguide circuits with superconducting single-photon detectors," *Appl. Phys. Lett.*, vol. 96, no. 21, p. 211101, 2010.
- [62] J. L. O'Brien, "Optical quantum computing," *Science (80-.)*, vol. 318, no. December, pp. 1567–1571, 2007.
- [63] G. A. Morton, "Photomultipliers for scintillation counting," *RCA Rev.*, vol. 10, pp. 525–553, 1949.
- [64] G. a. Morton, "PULSE HEIGHT RESOLUTION OF HIGH GAIN FIRST DYNODE PHOTOMULTIPLIERS," *Appl. Phys. Lett.*, vol. 13, no. 10, p. 356, 1968.
- [65] R. E. Simon, "NEW HIGH-GAIN DYNODE FOR PHOTOMULTIPLIERS," *Appl. Phys. Lett.*, vol. 13, no. 10, p. 355, 1968.
- [66] S. Pellegrini, R. E. Warburton, L. J. J. Tan, J. S. Ng, A. B. Krysa, K. Groom, J. P. R. David, S. Cova, M. J. Robertson, and G. S. Buller, "Design and Performance of an InGaAs–InP Single-Photon Avalanche Diode Detector," *IEEE J. Quantum Electron.*, vol. 42, no. 4, pp. 397–403, Apr. 2006.
- [67] M. Ghioni, A. Gulinatti, I. Rech, F. Zappa, and S. Cova, "Progress in Silicon Single-Photon Avalanche Diodes," *IEEE J. Sel. Top. Quantum Electron.*, vol. 13, no. 4, pp. 852–862, 2007.
- [68] S. E. Miller, Tingye Li, and E. A. J. Marcatili, "Part II: Devices and systems considerations," *Proc. IEEE*, vol. 61, no. 12, pp. 1726–1751, 1973.
- [69] R. H. Haitz, "Mechanisms Contributing to the Noise Pulse Rate of Avalanche Diodes," *J. Appl. Phys.*, vol. 36, no. 10, p. 3123, 1965.
- [70] S. Cova, "Towards picosecond resolution with single-photon avalanche diodes," *Rev. Sci. Instrum.*, vol. 52, no. 3, p. 408, 1981.
- [71] "<http://excelitas.com/Pages/Product/Avalanche-Photodiodes-APD.aspx>; retrieved on 12/27/2015." .
- [72] M. a. Itzler, X. Jiang, M. Entwistle, K. Slomkowski, A. Tosi, F. Acerbi, F. Zappa, and S. Cova, "Advances in InGaAsP-based avalanche diode single photon detectors," *J. Mod. Opt.*, vol. 58, no. 3–4, pp. 174–200, Feb. 2011.
- [73] A. Lacaita, F. Zappa, S. Cova, and P. Lovati, "Single-photon detection beyond 1 μm : performance of commercially available InGaAs/InP detectors.," *Appl. Opt.*, vol. 35, no. 16, pp. 2986–96, Jun. 1996.
- [74] A. Yoshizawa, R. Kaji, and H. Tsuchida, "Gated-mode single-photon detection at 1550 nm by discharge pulse counting," *Appl. Phys. Lett.*, vol. 84, no. 18, p. 3606, 2004.
- [75] C. Kurtsiefer, P. Zarda, S. Mayer, and H. Weinfurter, "The breakdown flash of Silicon Avalanche Photodiodes - backdoor for eavesdropper attacks?," *J. Mod. Opt.*, vol. 48, no. 13, pp. 2039–2047, 2001.
- [76] B. Cabrera, R. M. Clarke, P. Colling, a. J. Miller, S. Nam, and R. W. Romani, "Detection of single infrared, optical, and ultraviolet photons using superconducting transition edge sensors," *Appl. Phys. Lett.*, vol. 73, no. 6, p. 735, 1998.
- [77] T. Gerrits, N. Thomas-Peter, J. C. Gates, A. E. Lita, B. J. Metcalf, B. Calkins, N. a.

- Tomlin, A. E. Fox, A. L. Linares, J. B. Spring, N. K. Langford, R. P. Mirin, P. G. R. Smith, I. a. Walmsley, and S. W. Nam, "On-chip, photon-number-resolving, telecommunication-band detectors for scalable photonic information processing," *Phys. Rev. A*, vol. 84, no. 6, p. 060301, Dec. 2011.
- [78] A. J. Miller, S. W. Nam, J. M. Martinis, and A. V. Sergienko, "Demonstration of a low-noise near-infrared photon counter with multiphoton discrimination," *Appl. Phys. Lett.*, vol. 83, no. 4, pp. 791–793, 2003.
- [79] A. E. Lita, A. J. Miller, and S. W. Nam, "Counting near-infrared single-photons with 95% efficiency," *Opt. Express*, vol. 16, no. 5, p. 3032, 2008.
- [80] D. Rosenberg, A. Lita, A. Miller, and S. Nam, "Noise-free high-efficiency photon-number-resolving detectors," *Phys. Rev. A*, vol. 71, no. 6, p. 061803, Jun. 2005.
- [81] D. Fukuda, G. Fujii, T. Numata, A. Yoshizawa, H. Tsuchida, H. Fujino, H. Ishii, T. Itatani, S. Inoue, and T. Zama, "Photon number resolving detection with high speed and high quantum efficiency," *Metrologia*, vol. 46, no. 4, pp. S288–S292, Aug. 2009.
- [82] E. J. Gansen, M. A. Rowe, M. B. Greene, D. Rosenberg, T. E. Harvey, M. Y. Su, R. H. Hadfield, S. W. Nam, and R. P. Mirin, "Photon-number-discriminating detection using a quantum-dot, optically gated, field-effect transistor," *Nat. Photonics*, vol. 1, no. 10, pp. 585–588, Oct. 2007.
- [83] a. J. Shields, M. P. O'Sullivan, I. Farrer, D. a. Ritchie, R. a. Hogg, M. L. Leadbeater, C. E. Norman, and M. Pepper, "Detection of single photons using a field-effect transistor gated by a layer of quantum dots," *Appl. Phys. Lett.*, vol. 76, no. 25, p. 3673, 2000.
- [84] H. Kosaka, D. Rao, H. Robinson, P. Bandaru, T. Sakamoto, and E. Yablonovitch, "Photoconductance quantization in a single-photon detector," *Phys. Rev. B*, vol. 65, no. 20, p. 201307, 2002.
- [85] M. a. Rowe, E. J. Gansen, M. Greene, R. H. Hadfield, T. E. Harvey, M. Y. Su, S. W. Nam, R. P. Mirin, and D. Rosenberg, "Single-photon detection using a quantum dot optically gated field-effect transistor with high internal quantum efficiency," *Appl. Phys. Lett.*, vol. 89, no. 2006, pp. 6–9, 2006.
- [86] B. E. Kardynał, S. S. Hees, a. J. Shields, C. Nicoll, I. Farrer, and D. a. Ritchie, "Photon number resolving detector based on a quantum dot field effect transistor," *Appl. Phys. Lett.*, vol. 90, no. 18, p. 181114, 2007.
- [87] J. C. Blakesley, P. See, a. J. Shields, B. E. Kardynał, P. Atkinson, I. Farrer, and D. a. Ritchie, "Efficient Single Photon Detection by Quantum Dot Resonant Tunneling Diodes," *Phys. Rev. Lett.*, vol. 94, no. 6, p. 067401, Feb. 2005.
- [88] H. W. Li, B. E. Kardynał, P. See, a. J. Shields, P. Simmonds, H. E. Beere, and D. a. Ritchie, "Quantum dot resonant tunneling diode for telecommunication wavelength single photon detection," *Appl. Phys. Lett.*, vol. 91, no. 7, p. 073516, 2007.
- [89] S. Komiyama, O. Astafiev, V. Antonov, T. Kutsuwa, and H. Hirai, "A single-photon detector in the far-infrared range," *Nature*, vol. 403, no. 6768, pp. 405–407, Jan. 2000.
- [90] M. a. Albota and F. N. C. Wong, "Efficient single-photon counting at 1.55 μm by means of frequency upconversion," *Opt. Lett.*, vol. 29, no. 13, p. 1449, 2004.

- [91] A. P. Vandevender and P. G. Kwiat, "High efficiency single photon detection via frequency up-conversion," *J. Mod. Opt.*, vol. 51, no. 9–10, pp. 1433–1445, Jan. 2004.
- [92] C. Langrock, E. Diamanti, R. V Roussev, Y. Yamamoto, M. M. Fejer, and H. Takesue, "Highly efficient single-photon detection at communication wavelengths by use of upconversion in reverse-proton-exchanged periodically poled LiNbO₃ waveguides," *Opt. Lett.*, vol. 30, no. 13, p. 1725, 2005.
- [93] H. Takesue, E. Diamanti, T. Honjo, C. Langrock, M. M. Fejer, K. Inoue, and Y. Yamamoto, "Differential phase shift quantum key distribution experiment over 105 km fibre," *New J. Phys.*, vol. 7, no. 11, pp. 232–232, Nov. 2005.
- [94] E. Waks, K. Inoue, W. D. Oliver, E. Diamanti, and Y. Yamamoto, "High-efficiency photon-number detection for quantum information processing," *IEEE J. Sel. Top. Quantum Electron.*, vol. 9, no. 6, pp. 1502–1511, Nov. 2003.
- [95] S. Takeuchi, J. Kim, Y. Yamamoto, and H. H. Hogue, "Development of a high-quantum-efficiency single-photon counting system," *Appl. Phys. Lett.*, vol. 74, no. 8, p. 1063, 1999.
- [96] J. Kim, S. Takeuchi, Y. Yamamoto, and H. H. Hogue, "Multiphoton detection using visible light photon counter," *Appl. Phys. Lett.*, vol. 74, no. 7, p. 902, 1999.
- [97] "http://www.hamamatsu.com/resources/pdf/etd/PMTmodules_TPMO0010E.pdf; retrieved on 12/27/2015." .
- [98] C. Gobby, Z. L. Yuan, and a. J. Shields, "Quantum key distribution over 122 km of standard telecom fiber," *Appl. Phys. Lett.*, vol. 84, no. 19, pp. 3762–3764, 2004.
- [99] a R. Dixon, Z. L. Yuan, J. F. Dynes, a W. Sharpe, and a J. Shields, "Gigahertz decoy quantum key distribution with 1 Mbit/s secure key rate," *Opt. Express*, vol. 16, no. 23, p. 18790, Nov. 2008.
- [100] B. Baek, K. S. McKay, M. J. Stevens, J. Kim, H. H. Hogue, and S. W. Nam, "Single-photon detection timing jitter in a visible light photon counter," *IEEE J. Quantum Electron.*, vol. 46, no. 6, pp. 991–995, 2010.
- [101] N. K. Sherman, "Superconducting Nuclear Particle Detector," *Phys. Rev. Lett.*, vol. 8, no. 11, pp. 438–439, Jun. 1962.
- [102] G. N. Gol'tsman, A. D. Semenov, Y. P. Gousev, M. A. Zorin, I. G. Godidze, E. M. Gershenzon, P. T. Lang, W. J. Knott, and K. F. Renk, "Sensitive picosecond NbN detector for radiation from millimetre wavelengths to visible light," *Supercond. Sci. Technol.*, vol. 4, no. 9, pp. 453–456, Sep. 1991.
- [103] F. Marsili, F. Najafi, E. Dauler, F. Bellei, X. Hu, M. Csete, R. J. Molnar, and K. K. Berggren, "Single-photon detectors based on ultranarrow superconducting nanowires.," *Nano Lett.*, vol. 11, no. 5, pp. 2048–53, May 2011.
- [104] H. Shibata, M. Asahi, T. Maruyama, T. Akazaki, H. Takesue, T. Honjo, and Y. Tokura, "Optical Response and Fabrication of MgB₂ Nanowire Detectors," *IEEE Trans. Appl. Supercond.*, vol. 19, no. 3, pp. 358–360, Jun. 2009.
- [105] R. Lusche, A. Semenov, K. Ilin, M. Siegel, Y. Korneeva, A. Trifonov, A. Korneev, G. Goltsman, D. Vodolazov, and H.-W. Hübers, "Effect of the wire width on the intrinsic detection efficiency of superconducting-nanowire single-photon detectors," *J. Appl.*

- Phys.*, vol. 116, no. 4, p. 043906, Jul. 2014.
- [106] A. J. Kerman, E. a. Dauler, W. E. Keicher, J. K. W. Yang, K. K. Berggren, G. Gol'tsman, and B. Voronov, "Kinetic-inductance-limited reset time of superconducting nanowire photon counters," *Appl. Phys. Lett.*, vol. 88, no. 11, p. 111116, 2006.
- [107] A. J. Annunziata, O. Quaranta, D. F. Santavicca, A. Casaburi, L. Frunzio, M. Ejrnaes, M. J. Rooks, R. Cristiano, S. Pagano, A. Frydman, and D. E. Prober, "Reset dynamics and latching in niobium superconducting nanowire single-photon detectors," *J. Appl. Phys.*, vol. 108, no. 8, p. 084507, 2010.
- [108] K. M. Rosfjord, J. K. W. Yang, E. A. Dauler, A. J. Kerman, V. Anant, B. M. Voronov, G. N. Gol'tsman, and K. K. Berggren, "Nanowire single-photon detector with an integrated optical cavity and anti-reflection coating," *Opt. Express*, vol. 14, no. 2, p. 527, 2006.
- [109] B. Baek, J. a Stern, and S. W. Nam, "Superconducting nanowire single-photon detector in an optical cavity for front-side illumination," *Appl. Phys. Lett.*, vol. 95, no. 19, p. 191110, 2009.
- [110] D. Liu, S. Miki, T. Yamashita, L. You, Z. Wang, and H. Terai, "Multimode fiber-coupled superconducting nanowire single-photon detector with 70% system efficiency at visible wavelength," *Opt. Express*, vol. 22, no. 18, p. 21167, Sep. 2014.
- [111] F. Marsili, V. B. Verma, J. a. Stern, S. Harrington, a. E. Lita, T. Gerrits, I. Vayshenker, B. Baek, M. D. Shaw, R. P. Mirin, and S. W. Nam, "Detecting single infrared photons with 93% system efficiency," *Nat. Photonics*, vol. 7, no. 3, pp. 210–214, Feb. 2013.
- [112] A. Engel, J. J. Renema, K. Il'in, and A. Semenov, "Detection mechanism of superconducting nanowire single-photon detectors," *Supercond. Sci. Technol.*, vol. 28, no. 11, p. 114003, Nov. 2015.
- [113] L. N. Bulaevskii, M. J. Graf, C. D. Batista, and V. G. Kogan, "Vortex-induced dissipation in narrow current-biased thin-film superconducting strips," *Phys. Rev. B*, vol. 83, no. 14, p. 144526, Apr. 2011.
- [114] L. N. Bulaevskii, M. J. Graf, and V. G. Kogan, "Vortex-assisted photon counts and their magnetic field dependence in single-photon superconducting detectors," *Phys. Rev. B*, vol. 85, no. 1, p. 014505, Jan. 2012.
- [115] A. Engel and A. Schilling, "Numerical analysis of detection-mechanism models of superconducting nanowire single-photon detector," *J. Appl. Phys.*, vol. 114, no. 21, p. 214501, 2013.
- [116] A. Engel, J. Lonsky, X. Zhang, and A. Schilling, "Detection Mechanism in SNSPD: Numerical Results of a Conceptually Simple, Yet Powerful Detection Model," *IEEE Trans. Appl. Supercond.*, vol. 25, no. 3, pp. 1–7, Jun. 2015.
- [117] A. N. Zotova and D. Y. Vodolazov, "Photon detection by current-carrying superconducting film: A time-dependent Ginzburg-Landau approach," *Phys. Rev. B*, vol. 85, no. 2, p. 024509, Jan. 2012.
- [118] A. Engel, A. Semenov, H.-W. Hübers, K. Ilin, and M. Siegel, "Dark counts of a superconducting single-photon detector," *Nucl. Instruments Methods Phys. Res. Sect. A Accel. Spectrometers, Detect. Assoc. Equip.*, vol. 520, no. 1–3, pp. 32–35, Mar. 2004.
- [119] a Semenov, A. Engel, K. Il'in, M. Siegel, and H.-W. Hubers, "Noise of a

- Superconducting Photon Detector," *IEEE Trans. Applied Supercond.*, vol. 15, no. 2, pp. 518–521, Jun. 2005.
- [120] J. Kitaygorsky, J. Zhang, a. Verevkin, a. Sergeev, a. Korneev, V. Matvienko, P. Kouminov, K. Smirnov, B. Voronov, G. Gol'tsman, and R. Sobolewski, "Origin of Dark Counts in Nanostructured NbN Single-Photon Detectors," *IEEE Trans. Applied Supercond.*, vol. 15, no. 2, pp. 545–548, Jun. 2005.
- [121] M. Bell, A. Sergeev, V. Mitin, J. Bird, A. Verevkin, and G. Gol'tsman, "One-dimensional resistive states in quasi-two-dimensional superconductors: Experiment and theory," *Phys. Rev. B*, vol. 76, no. 9, p. 094521, Sep. 2007.
- [122] A. Engel, A. Semenov, H.-W. Hübers, K. Il'in, and M. Siegel, "Fluctuations and dark count rates in superconducting NbN single-photon detectors," *Phys. status solidi*, vol. 2, no. 5, pp. 1668–1673, Mar. 2005.
- [123] J. Kitaygorsky, I. Komissarov, A. Jukna, D. Pan, O. Minaeva, N. Kaurova, A. Divochiy, A. Korneev, M. Tarkhov, B. Voronov, I. Milostnaya, G. Gol'tsman, and R. R. Sobolewski, "Dark Counts in Nanostructured NbN Superconducting Single-Photon Detectors and Bridges," *IEEE Trans. Appl. Supercond.*, vol. 17, no. 2, pp. 275–278, Jun. 2007.
- [124] T. Yamashita, S. Miki, K. Makise, W. Qiu, H. Terai, M. Fujiwara, M. Sasaki, and Z. Wang, "Origin of intrinsic dark count in superconducting nanowire single-photon detectors," *Appl. Phys. Lett.*, vol. 99, no. 16, p. 161105, 2011.
- [125] C. Qiu and T. Qian, "Numerical study of the phase slip in two-dimensional superconducting strips," *Phys. Rev. B*, vol. 77, no. 17, p. 174517, May 2008.
- [126] J. R. Clem and K. K. Berggren, "Geometry-dependent critical currents in superconducting nanocircuits," *Phys. Rev. B*, vol. 84, no. 17, p. 174510, Nov. 2011.
- [127] H. L. Hortensius, E. F. C. Driessen, T. M. Klapwijk, K. K. Berggren, and J. R. Clem, "Critical-current reduction in thin superconducting wires due to current crowding," *Appl. Phys. Lett.*, vol. 100, no. 18, p. 182602, 2012.
- [128] D. Henrich, P. Reichensperger, M. Hofherr, J. M. Meckbach, K. Il'in, M. Siegel, A. Semenov, A. Zotova, and D. Y. Vodolazov, "Geometry-induced reduction of the critical current in superconducting nanowires," *Phys. Rev. B*, vol. 86, no. 14, p. 144504, Oct. 2012.
- [129] M. Tinkham, *Introduction to Superconductivity*, 2nd editio. McGraw-Hill, 1996.
- [130] V. V. Schmidt, *The Physics of Superconductors*. Berlin, Heidelberg: Springer Berlin Heidelberg, 1997.
- [131] M. P. Marder, *Condensed Matter Physics*, 2nd Editio. Wiley, 2010.
- [132] J. F. Annett, "Superconductivity, Superfluids and Condensates," no. May, p. 140, 2004.
- [133] P. Seidel, *Applied Superconductivity*. Wiley, 2015.
- [134] J. Bardeen, L. Cooper, and J. Schrieffer, "Microscopic Theory of Superconductivity," *Phys. Rev.*, vol. 106, no. 1, pp. 162–164, Apr. 1957.
- [135] J. Bardeen, L. N. Cooper, and J. R. Schrieffer, "Theory of Superconductivity," *Phys. Rev.*, vol. 108, no. 5, pp. 1175–1204, Dec. 1957.

- [136] L. N. Cooper, "Bound Electron Pairs in a Degenerate Fermi Gas," *Phys. Rev.*, vol. 104, no. 4, pp. 1189–1190, Nov. 1956.
- [137] A. Bezryadin, *Superconductivity in Nanowires*. Wiley, 2013.
- [138] R. Gross and A. Marx, *Festkörperphysik*. Oldenbourg Wissenschaftsverlag, 2012.
- [139] N. N. Bogoljubov, V. V. Tolmachov, and D. V. Širkov, "A New Method in the Theory of Superconductivity," *Fortschritte der Phys.*, vol. 6, no. 11–12, pp. 605–682, 1958.
- [140] J. G. Valatin, "Comments on the theory of superconductivity," *Nuovo Cim.*, vol. 7, no. 6, pp. 843–857, Mar. 1958.
- [141] H. Ibach and H. Lüth, *Solid-State Physics*. Berlin, Heidelberg: Springer Berlin Heidelberg, 2009.
- [142] F. London and H. London, "The Electromagnetic Equations of the Supraconductor," *Proc. R. Soc. A Math. Phys. Eng. Sci.*, vol. 149, no. 866, pp. 71–88, Mar. 1935.
- [143] L. D. Landau, "On the theory of phase transitions," *Zh. Eks. Teor. Fiz.*, vol. 7, no. 1937, pp. 19–32, 1937.
- [144] V. L. Ginzburg and L. D. Landau, "On the theory of superconductivity," *Zh. Eksp. Teor. Fiz.*, vol. 20, pp. 1064–1082, 1950.
- [145] A. A. Abrikosov, "On the Magnetic Properties of Superconductors of the Second Group," *JETP*, vol. 5, p. 1174, 1957.
- [146] B. I. Halperin and D. R. Nelson, "Resistive transition in superconducting films," *J. Low Temp. Phys.*, vol. 36, no. 5–6, pp. 599–616, Sep. 1979.
- [147] B. I. Halperin, G. Refael, and E. Demler, "RESISTANCE IN SUPERCONDUCTORS," *Int. J. Mod. Phys. B*, vol. 24, no. 20n21, pp. 4039–4080, Aug. 2010.
- [148] J. Pearl, "CURRENT DISTRIBUTION IN SUPERCONDUCTING FILMS CARRYING QUANTIZED FLUXOIDS," *Appl. Phys. Lett.*, vol. 5, no. 4, p. 65, 1964.
- [149] K. K. Likharev, "Superconducting weak links," *Rev. Mod. Phys.*, vol. 51, no. 1, pp. 101–159, Jan. 1979.
- [150] J. D. Jackson, *Classical Electrodynamics*, 3rd editio. Wiley, 1999.
- [151] K. Fossheim and A. Sudbø, *Superconductivity*. Chichester, UK: John Wiley & Sons, Ltd, 2004.
- [152] R. P. Huebener, *Magnetic Flux Structures in Superconductors*, vol. 6. Berlin, Heidelberg: Springer Berlin Heidelberg, 2001.
- [153] C. P. Bean and J. D. Livingston, "Surface Barrier in Type-II Superconductors," *Phys. Rev. Lett.*, vol. 12, no. 1, pp. 14–16, Jan. 1964.
- [154] I. L. Maksimov and G. M. Maksimova, "Stability limits, structure, and relaxation of a mixed state in superconducting films with an edge barrier," *J. Exp. Theor. Phys. Lett.*, vol. 65, no. 5, pp. 423–429, Mar. 1997.
- [155] G. M. Maksimova, "Mixed state and critical current in narrow semiconducting films," *Phys. Solid State*, vol. 40, no. 10, pp. 1607–1610, Oct. 1998.
- [156] G. Stan, S. B. Field, and J. M. Martinis, "Critical Field for Complete Vortex Expulsion from Narrow Superconducting Strips," *Phys. Rev. Lett.*, vol. 92, no. 9, p. 097003, Mar.

- 2004.
- [157] M. Benkraouda and J. R. Clem, "Magnetic hysteresis from the geometrical barrier in type-II superconducting strips," *Phys. Rev. B*, vol. 53, no. 9, pp. 5716–5726, Mar. 1996.
- [158] A. Engel, A. D. Semenov, H.-W. Hübers, K. Il'in, and M. Siegel, "Fluctuation effects in superconducting nanostrips," *Phys. C Supercond. its Appl.*, vol. 444, no. 1–2, pp. 12–18, Sep. 2006.
- [159] D. Y. Vodolazov, "Current dependence of the red boundary of superconducting single-photon detectors in the modified hot-spot model," *Phys. Rev. B*, vol. 90, no. 5, p. 054515, Aug. 2014.
- [160] J. E. Mooij, "Two-Dimensional Transition in Superconducting Films and Junction Arrays," in *Percolation, Localization, and Superconductivity*, Boston, MA: Springer US, 1984, pp. 325–370.
- [161] J. M. Kosterlitz and D. J. Thouless, "Ordering, metastability and phase transitions in two-dimensional systems," *J. Phys. C Solid State Phys.*, vol. 6, no. 7, pp. 1181–1203, Apr. 1973.
- [162] Y. Liu, D. B. Haviland, L. I. Glazman, and A. M. Goldman, "Resistive transitions in ultrathin superconducting films: Possible evidence for quantum tunneling of vortices," *Phys. Rev. Lett.*, vol. 68, no. 14, pp. 2224–2227, Apr. 1992.
- [163] M. Hofherr, D. Rall, K. Il'in, A. Semenov, H.-W. Hübers, and M. Siegel, "Dark Count Suppression in Superconducting Nanowire Single Photon Detectors," *J. Low Temp. Phys.*, vol. 167, no. 5–6, pp. 822–826, Jun. 2012.
- [164] F. Tafuri, J. R. Kirtley, D. Born, D. Stornaiuolo, P. G. Medaglia, P. Orgiani, G. Balestrino, and V. G. Kogan, "Dissipation in ultra-thin current-carrying superconducting bridges; evidence for quantum tunneling of Pearl vortices," *Eur. Lett.*, vol. 73, p. 948, 2006.
- [165] D. E. McCumber and B. I. Halperin, "Time Scale of Intrinsic Resistive Fluctuations in Thin Superconducting Wires," *Phys. Rev. B*, vol. 1, no. 3, pp. 1054–1070, Feb. 1970.
- [166] J. S. Langer and V. Ambegaokar, "Intrinsic Resistive Transition in Narrow Superconducting Channels," *Phys. Rev.*, vol. 164, no. 2, pp. 498–510, Dec. 1967.
- [167] A. D. Semenov, G. N. Gol'tsman, and R. Sobolewski, "Hot-electron effect in superconductors and its applications for radiation sensors," *Supercond. Sci. Technol.*, vol. 15, no. 4, pp. R1–R16, Apr. 2002.
- [168] A. N. Zotova and D. Y. Vodolazov, "Intrinsic detection efficiency of superconducting nanowire single photon detector in the modified hot spot model," *Supercond. Sci. Technol.*, vol. 27, no. 12, p. 125001, Dec. 2014.
- [169] J. J. Renema, R. Gaudio, Q. Wang, Z. Zhou, a. Gaggero, F. Mattioli, R. Leoni, D. Sahin, M. J. a. de Dood, a. Fiore, and M. P. van Exter, "Experimental Test of Theories of the Detection Mechanism in a Nanowire Superconducting Single Photon Detector," *Phys. Rev. Lett.*, vol. 112, no. 11, p. 117604, Mar. 2014.
- [170] A. Korneev and V. Matvienko, "Quantum efficiency and noise equivalent power of nanostructured, NbN, single-photon detectors in the wavelength range from visible to infrared," *IEEE Trans. Appl. Supercond.*, vol. 15, no. 2, pp. 571–574, 2005.

- [171] G. Gol'tsman, O. Minaeva, a. Korneev, M. Tarkhov, I. Rubtsova, a. Divochiy, I. Milostnaya, G. Chulkova, N. Kaurova, B. Voronov, D. Pan, J. Kitaygorsky, a. Cross, a. Pearlman, I. Komissarov, W. Slysz, M. Wegrzecki, P. Grabiec, and R. Sobolewski, "Middle-Infrared to Visible-Light Ultrafast Superconducting Single-Photon Detectors," *IEEE Trans. Appl. Supercond.*, vol. 17, no. 2, pp. 246–251, Jun. 2007.
- [172] L. You, X. Yang, Y. He, W. Zhang, D. Liu, W. Zhang, L. Zhang, L. Zhang, X. Liu, S. Chen, Z. Wang, and X. Xie, "Jitter analysis of a superconducting nanowire single photon detector," *AIP Adv.*, vol. 3, no. 7, p. 072135, 2013.
- [173] E. A. Dauler, A. J. Kerman, B. S. Robinson, J. K. W. Yang, B. Voronov, G. Goltsman, S. A. Hamilton, and K. K. Berggren, "Photon-number-resolution with sub-30-ps timing using multi-element superconducting nanowire single photon detectors," *J. Mod. Opt.*, vol. 56, no. 2–3, pp. 364–373, Jan. 2009.
- [174] R. E. Correa, E. A. Dauler, G. Nair, S. H. Pan, D. Rosenberg, A. J. Kerman, R. J. Molnar, X. Hu, F. Marsili, V. Anant, K. K. Berggren, and M. G. Bawendi, "Single photon counting from individual nanocrystals in the infrared," *Nano Lett.*, vol. 12, no. 6, pp. 2953–8, Jun. 2012.
- [175] R. W. Heeres, S. N. Dorenbos, B. Koene, G. S. Solomon, L. P. Kouwenhoven, and V. Zwiller, "On-Chip Single Plasmon Detection," *Nano Lett.*, vol. 10, no. 2, pp. 661–664, Feb. 2010.
- [176] R. W. Heeres, L. P. Kouwenhoven, and V. Zwiller, "Quantum interference in plasmonic circuits," *Nat. Nanotechnol.*, vol. 8, no. 10, pp. 719–722, Aug. 2013.
- [177] A. Yariv and P. Yeh, *Photonics*, 6th editio. New York: Oxford University Press, 2007.
- [178] M. Calvo and V. Lakshminayaranan, "Optical waveguides: from theory to applied technologies." p. 401, 2007.
- [179] K. Okamoto, *Fundamentals of Optical Waveguides*. 2006.
- [180] J.-M. Liu, *Photonic Devices*. Cambridge: Cambridge University Press, 2005.
- [181] L. D. Landau and E. M. Lifshitz, *Electrodynamics of Continuous Media*, 1st Editio. Pergamon Press, 1960.
- [182] C. Schuck, W. H. P. Pernice, and H. X. Tang, "NbTiN superconducting nanowire detectors for visible and telecom wavelengths single photon counting on Si₃N₄ photonic circuits," *Appl. Phys. Lett.*, vol. 102, no. 5, p. 051101, 2013.
- [183] C. H. Henry, R. F. Kazarinov, H. J. Lee, K. J. Orlowsky, and L. E. Katz, "Low loss Si(3)N(4)-SiO(2) optical waveguides on Si.," *Appl. Opt.*, vol. 26, no. 13, pp. 2621–4, Jul. 1987.
- [184] C. a. Barrios, B. Sánchez, K. B. Gylfason, A. Griol, H. Sohlström, M. Holgado, and R. Casquel, "Demonstration of slot-waveguide structures on silicon nitride / silicon oxide platform," *Opt. Express*, vol. 15, no. 11, p. 6846, 2007.
- [185] A. Gondarenko, J. S. Levy, and M. Lipson, "High confinement micron-scale silicon nitride high Q ring resonator," *Opt. Express*, vol. 17, no. 14, p. 11366, Jun. 2009.
- [186] D. J. Moss, R. Morandotti, A. L. Gaeta, and M. Lipson, "New CMOS-compatible platforms based on silicon nitride and Hydex for nonlinear optics," *Nat. Photonics*, vol. 7, no. 8, pp. 597–607, Jul. 2013.

- [187] S. V. Deshpande, E. Gulari, S. W. Brown, and S. C. Rand, "Optical properties of silicon nitride films deposited by hot filament chemical vapor deposition," *J. Appl. Phys.*, vol. 77, no. 12, p. 6534, 1995.
- [188] J. S. Levy, M. a. Foster, A. L. Gaeta, and M. Lipson, "Harmonic generation in silicon nitride ring resonators," *Opt. Express*, vol. 19, no. 12, pp. 11415–11421, 2011.
- [189] T. Bååk, "Silicon oxynitride; a material for GRIN optics," *Appl. Opt.*, vol. 21, no. 6, p. 1069, Mar. 1982.
- [190] R. P. Frankenthal, "Thermal Oxidation of Niobium Nitride Films at Temperatures from 20°–400°C," *J. Electrochem. Soc.*, vol. 130, no. 10, p. 2056, 1983.
- [191] P. K. Gallagher, "Oxidation of Sputtered Niobium Nitride Films," *J. Electrochem. Soc.*, vol. 130, no. 10, p. 2054, 1983.
- [192] X. Hu, "Efficient Superconducting-Nanowire Single-Photon Detectors and Their Applications in Quantum Optics," *PhD Thesis, MIT*. 2011.
- [193] O. Kahl, S. Ferrari, V. Kovalyuk, G. N. Goltsman, A. Korneev, and W. H. P. Pernice, "Waveguide integrated superconducting single-photon detectors with high internal quantum efficiency at telecom wavelengths," *Sci. Rep.*, vol. 5, no. February, p. 10941, 2015.
- [194] O. Kahl, W. Pernice, O. Kahl, S. Ferrari, P. Rath, A. Vetter, and C. Nebel, "High efficiency, on-chip single-photon detection for diamond nanophotonic circuits," *J. Light. Technol.*, vol. 8724, no. c, pp. 1–1, 2015.
- [195] P. Rath, O. Kahl, S. Ferrari, F. Sproll, G. Lewes-Malandrakis, D. Brink, K. Ilin, M. Siegel, C. Nebel, and W. Pernice, "Superconducting single-photon detectors integrated with diamond nanophotonic circuits," *Light Sci. Appl.*, vol. 4, no. 10, p. e338, Oct. 2015.
- [196] a. D. Semenov, R. S. Nebosis, Y. P. Gousev, M. a. Heusinger, and K. F. Renk, "Analysis of the nonequilibrium photoresponse of superconducting films to pulsed radiation by use of a two-temperature model," *Phys. Rev. B*, vol. 52, no. 1, pp. 581–590, Jul. 1995.
- [197] J. S. Lundeen, a. Feito, H. Coldenstrodt-Ronge, K. L. Pregnell, C. Silberhorn, T. C. Ralph, J. Eisert, M. B. Plenio, and I. a. Walmsley, "Tomography of quantum detectors," *Nat. Phys.*, vol. 5, no. 1, pp. 27–30, 2009.
- [198] A. Feito, J. S. Lundeen, H. Coldenstrodt-Ronge, J. Eisert, M. B. Plenio, and I. a. Walmsley, "Measuring measurement: theory and practice," *New J. Phys.*, vol. 11, no. 9, p. 093038, Sep. 2009.
- [199] R. Loudon, *The Quantum Theory of Light*. Oxford University Press, 1997.
- [200] M. O. Scully and M. S. Zubairy, *Quantum Optics*. Cambridge University Press, 1997.
- [201] C. Gerry and P. Knight, *Introductory Quantum Optics*. Cambridge University Press, 2005.
- [202] H. Haken and H. C. Wolf, *The Physics of Atoms and Quanta*, 7th editio. Springer, 2005.
- [203] P. Meystre and M. Sargent, *Elements of Quantum Optics*, 4th editio. Berlin: Springer, 2007.
- [204] R. J. Glauber, "The Quantum Theory of Optical Coherence," *Phys. Rev.*, vol. 130, no. 6, pp. 2529–2539, Jun. 1963.

- [205] X. T. Zou and L. Mandel, "Photon-antibunching and sub-Poissonian photon statistics," *Phys. Rev. A*, vol. 41, no. 1, pp. 475–476, 1990.
- [206] S. Boyd and L. Vandenberghe, *Convex Optimization*. Cambridge: Cambridge University Press, 2004.
- [207] M. S. Elezov, A. V. Semenov, P. P. An, M. A. Tarkhov, G. N. Goltsman, A. I. Kardakova, and A. Y. Kazakov, "Investigating the detection regimes of a superconducting single-photon detector," *J. Opt. Technol.*, vol. 80, p. 435, 2013.
- [208] J. J. Renema, G. Frucci, Z. Zhou, F. Mattioli, A. Gaggero, R. Leoni, M. J. A. de Dood, A. Fiore, and M. P. van Exter, "Modified detector tomography technique applied to a superconducting multiphoton nanodetector," *Opt. Express*, vol. 20, no. 3, pp. 2806–13, Jan. 2012.
- [209] M. K. Smit and C. Van Dam, "PHASAR-based WDM-devices: Principles, design and applications," *IEEE J. Sel. Top. Quantum Electron.*, vol. 2, no. 2, pp. 236–250, Jun. 1996.
- [210] P. Cheben, J. H. Schmid, A. Delâge, A. Densmore, S. Janz, B. Lamontagne, J. Lapointe, E. Post, P. Waldron, and D.-X. Xu, "A high-resolution silicon-on-insulator arrayed waveguide grating microspectrometer with sub-micrometer aperture waveguides," *Opt. Express*, vol. 15, no. 5, p. 2299, 2007.
- [211] L. Chen, C. R. Doerr, L. Buhl, Y. Baeyens, and R. A. Aroca, "Monolithically Integrated 40-Wavelength Demultiplexer and Photodetector Array on Silicon," *IEEE Photonics Technol. Lett.*, vol. 23, no. 13, pp. 869–871, Jul. 2011.
- [212] E. Hecht, *Optics*, 4th editio. Addison Wesley, 2002.
- [213] M. Bass, E. Van Stryland, D. Williams, and W. Wolfe, *OSA Handbook of Optics, Volume I - Fundamentals, Techniques, and Design*, 2nd editio. New York: McGraw-Hill, 1995.
- [214] M. . Smit, "New focussing and dispersive planar component based on an optical phased array," *Electron. Lett.*, vol. 24, no. 7, pp. 385–386, 1988.
- [215] A. R. Vellekoop and M. K. Smit, "Low-loss planar optical polarisation splitter with small dimensions," *Electron. Lett.*, vol. 25, no. 15, p. 946, 1989.
- [216] A. R. Vellekoop and M. K. Smit, "Four-channel integrated-optic wavelength demultiplexer with weak polarization dependence," *J. Light. Technol.*, vol. 9, no. 3, pp. 310–314, Mar. 1991.
- [217] P. Dumon, W. Bogaerts, D. Van Thourhout, D. Taillaert, R. Baets, J. Wouters, S. Beckx, and P. Jaenen, "Compact wavelength router based on a Silicon-on-insulator arrayed waveguide grating pigtailed to a fiber array," *Opt. Express*, vol. 14, no. 2, p. 664, 2006.
- [218] R. März, *Integrated Optics: Design and Modeling*. Artech House Publishers, 1995.
- [219] C. van Dam, A. A. M. Staring, E. J. Jansen, J. J. M. Binsma, T. van Dongen, M. K. Smit, and B. H. Verbeek, "Loss reduction for phased-array demultiplexers using a double etch technique," in *Integrated Photonics Research*, 1996, p. IMC6.
- [220] K. Maru, T. Chiba, M. Okawa, H. Ishikawa, K. Ohira, S. Sato, and H. Uetsuka, "Low-loss arrayed-waveguide grating with high index regions at slab-to-array interface," *Electron. Lett.*, vol. 37, no. 21, p. 1287, 2001.
- [221] a. Sugita, A. Kaneko, K. Okamoto, M. Itoh, A. Himeno, and Y. Ohmori, "Very low

- insertion loss arrayed-waveguide grating with vertically tapered waveguides," *IEEE Photonics Technol. Lett.*, vol. 12, no. 9, pp. 1180–1182, Sep. 2000.
- [222] F. Ohno, K. Sasaki, A. Motegi, and T. Baba, "Reduction in Sidelobe Level in Ultracompact Arrayed Waveguide Grating Demultiplexer Based on Si Wire Waveguide," *Jpn. J. Appl. Phys.*, vol. 45, no. 8A, pp. 6126–6131, Aug. 2006.
- [223] W. K. Burns, A. F. Milton, and A. B. Lee, "Optical waveguide parabolic coupling horns," *Appl. Phys. Lett.*, vol. 30, no. 1, p. 28, 1977.
- [224] "http://www.ntt-electronics.com/en/products/photronics/awg_mul_d.html; retrieved on 12/27/2015." .
- [225] I. Aharonovich, S. Castelletto, D. A. Simpson, C.-H. Su, A. D. Greentree, and S. Praver, "Diamond-based single-photon emitters," *Reports Prog. Phys.*, vol. 74, no. 7, p. 076501, Jul. 2011.
- [226] C. Wang, C. Kurtsiefer, H. Weinfurter, and B. Burchard, "Single photon emission from SiV centres in diamond produced by ion implantation," *J. Phys. B At. Mol. Opt. Phys.*, vol. 39, no. 1, pp. 37–41, Jan. 2006.
- [227] P. Eraerds, M. Legré, and J. Zhang, "Photon counting OTDR: advantages and limitations," *J. Light. Technol.*, vol. 28, no. 6, pp. 952–964, 2010.
- [228] F. Stellari, P. Song, and A. Weger, "Single Photon Detectors for Ultra Low Voltage Time-Resolved Emission Measurements," *Quantum Electron. IEEE ...*, vol. 47, no. 6, pp. 841–848, Jun. 2011.
- [229] A. Korneev, Y. Vachtomin, O. Minaeva, A. Divochiy, K. Smirnov, O. Okunev, G. Gol'tsman, C. Zinoni, N. Chauvin, L. Balet, F. Marsili, D. Bitauld, B. Alloing, L. Li, A. Fiore, L. Lunghi, A. Gerardino, M. Halder, C. Jorel, and H. Zbinden, "Single-Photon Detection System for Quantum Optics Applications," *IEEE J. Sel. Top. Quantum Electron.*, vol. 13, no. 4, pp. 944–951, 2007.
- [230] V. Giovannetti, S. Lloyd, and L. Maccone, "Advances in quantum metrology," *Nat. Photonics*, vol. 5, no. 4, pp. 222–229, Apr. 2011.
- [231] a. Gaggero, S. J. Nejad, F. Marsili, F. Mattioli, R. Leoni, D. Bitauld, D. Sahin, G. J. Hamhuis, R. Nötzel, R. Sanjines, and A. Fiore, "Nanowire superconducting single-photon detectors on GaAs for integrated quantum photonic applications," *Appl. Phys. Lett.*, vol. 97, no. 15, p. 151108, 2010.
- [232] A. L. Migdall, D. Branning, and S. Castelletto, "Tailoring single-photon and multiphoton probabilities of a single-photon on-demand source," *Phys. Rev. A*, vol. 66, no. 5, p. 053805, Nov. 2002.
- [233] S. Tanzilli, W. Tittel, H. De Riedmatten, H. Zbinden, P. Baldi, M. Demicheli, D. B. Ostrowsky, and N. Gisin, "PPLN waveguide for quantum communication," *Eur. Phys. J. D*, vol. 18, no. 2, pp. 155–160, 2002.
- [234] A. Bezryadin, C. Lau, and M. Tinkham, "Quantum suppression of superconductivity in ultrathin nanowires," *Nature*, vol. 404, no. 6781, pp. 971–4, May 2000.
- [235] W. a. Little, "Decay of Persistent Currents in Small Superconductors," *Phys. Rev.*, vol. 156, no. 2, pp. 396–403, Apr. 1967.
- [236] V. Kovalyuk, W. Hartmann, O. Kahl, N. Kaurova, A. Korneev, G. Goltsman, and W. H. P.

References

- Pernice, "Absorption engineering of NbN nanowires deposited on silicon nitride nanophotonic circuits," *Opt. Express*, vol. 21, no. 19, pp. 22683–92, Sep. 2013.
- [237] S. Ferrari, O. Kahl, V. Kovalyuk, G. N. Goltsman, A. Korneev, and W. H. P. Pernice, "Waveguide-integrated single- and multi-photon detection at telecom wavelengths using superconducting nanowires," *Appl. Phys. Lett.*, vol. 106, no. 15, p. 151101, Apr. 2015.

APPENDIX

A1. LITTLE PHASE SLIPS

In one-dimensional (1D) superconductors (i.e. width $w < \xi$ and thickness $d < \xi$), the wavefunction of the superconducting condensate is completely uniform across the entire wire cross-section and only depends on the position x along the wire, i.e. $\psi(\mathbf{r}) \rightarrow \psi(x)$ [112], [129]. In this case, any local change to the phase of ψ affects the wire's superconducting properties on a global scale [234]. The predominant effect is an altered dependence of resistance vs. temperature relative to a bulk superconductor of the same material. William D. Little offered an explanation based on incremental reductions in the order parameter's phase [235] which are nowadays referred to as *Little phase slips* (LPSs). For a constant, time-independent supercurrent along a 1D nanowire of length L , one can assume $\psi(x) = \sqrt{n_s} \exp(ikx)$. The function $\psi(x)$ can be plotted in the complex plane extended by the spatial dimension x . It is easy to imagine that the result is a spiral of constant radius $\sqrt{n_s}$ and $n = kL/2\pi$ rotations (see Figure A1-1). Little argued that any fluctuation which exceeds the effective condensation energy inside a local volume $wd\xi$ would cause ψ to vanish locally and cause the global phase $\theta = kx$ to *slip* (reduce) by 2π [137], [235]. Following the London theory description, a reduction in the number of rotations n decreases the phase gradient $\nabla\theta = k$ from $k = 2n\pi/L$ to $k' = 2(n-1)\pi/L$, which directly leads to a decrease in the supercurrent density $j_s \propto \nabla\theta = k$. In a nanowire which carries a persistent transport current without an external

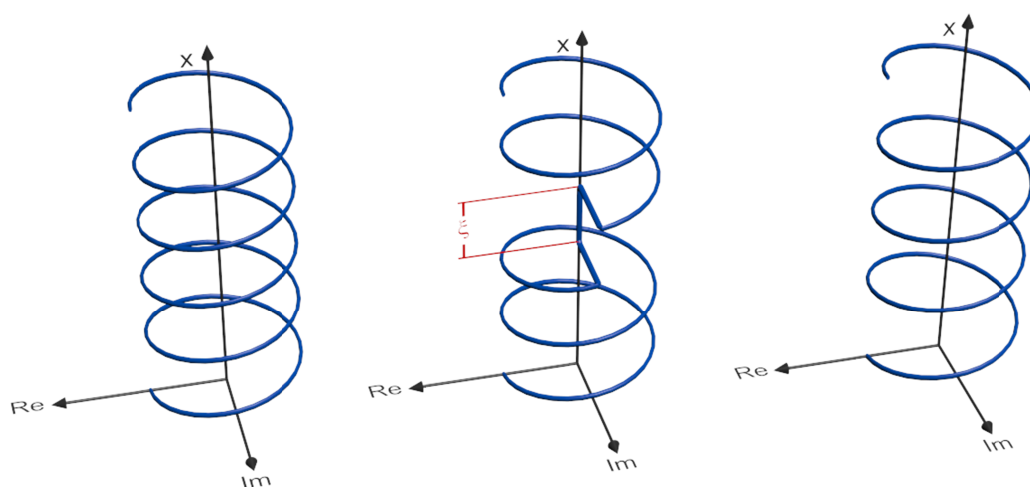


Figure A1-1: Schematic illustration of Little phase slip. Left: initial state of order parameter before phase slip, $n = 5$; Center: phase slip reduces amplitude across phase slip center (red). Right: final state of order parameter after phase slip, $n = 4$

driving source, phase slips cause the current to dissipate over time. The volume $wd\xi$ in which a phase slip occurs is commonly referred to as *phase slip center*. In 2D nanowires, similar phase slips exist, yet they originate from the nucleation of vortices.

A2. FABRICATION RECIPES

I. Alignment markers and contact pads

1. Sonicate chip in acetone for 5min
2. Bake on hotplate: 1min, 120°C
3. Spin coat 800nm thick PMMA 8.0 film: 4000rpm, 1000rpms, 90s
4. Bake on hotplate: 3min, 120°C
5. e-beam lithography (JEOL): 500uC/cm², 6nA, step size 12nm, no PEC
6. Development: 60-120sec MIBK:Isopropanol 1:3
7. Deposit 5nm Cr and 150nm Au via PVD
8. Lift-off: for structures >1um: sonicate in acetone for 2-3 min; otherwise (structures <1um) soak in acetone bath for >15min, use syringe to blow off gold

II. Nanowires and connection wings

1. Deposit 5nm SiO₂ (adhesion layer for HSQ) via PVD
2. Take HSQ 2.0% from refrigerator and warm up to room temperature (takes ca. 15min)
3. Sonicate chip in acetone for 5min
4. Bake on hot plate: 80°C, 1min
5. Spin coat ~50nm HSQ 2.0%: 3000 RPM, 1000 RPM/sec, 60sec
6. Bake on hotplate (5min, 90°C)
7. e-beam lithography (JEOL): Wires and wings using PEC (base dose 2200uC/cm² x 1.6), patches overlapping gold contacts 1200uC/cm²; 100pA, step size 4nm
8. Development: 4min TMAH 6.25%, stop in H₂O (1min)
9. Remove SiO₂ + etch NbN nanowires, RIE: 30sccm CF₄, 100W RF power, 1.3Pa, 45sec (10 sec to remove SiO₂ + 35sec to etch 4nm NbN)

III. Waveguides

1. Bake on hotplate: 120°C, 10min
2. Spin coat Ti-Prime (adhesion promoter): 3000rpm, 1000rpm/s, 23sec
3. Bake on hotplate: 120°C, 2min
4. Spin coat ~340nm maN 2403: 400rpm, 4sec; 3400RPM, 60sec; 1000rpm/s
5. Bake on hotplate: 90°C, 2min
6. e-beam lithography (JEOL): 180uC/cm², 100pA, step size 4nm
7. Development: 1min MF319
8. Etch waveguides, RIE: 50sccm CHF₃, 2sccm O₂, 175W RF power, 55 mTorr -> 1.1nm/s
9. Remove residual ma-N, RIE: 20sccm O₂, 60W RF power, 50mTorr, 5min

A3. PHOTON FLUX CALIBRATION

In order to ensure a well-calibrated photon flux toward the detector several loss contributions have to be accounted for. These include the grating couplers (GCs) used for coupling light into and out of the chip and waveguide propagation losses. The latter are small with 0.4 dB/mm (obtained from standard ring resonator measurements) while the GC losses can be significant. In Figure A3-1, the transmissivities are labelled as C for the GCs, S denotes the splitting ratio and WGL_{ref} and WGL_{det} refer to the waveguide losses toward the reference port and detector, respectively. Coming from the input GC, the following relation between the input power P_{in} and the output power on the reference port P_{ref} can be derived

$$P_{ref} = P_{in} C^2 S \times WGL_{ref} \quad \text{A2-1}$$

An analogous equation exists for the relation between the input power P_{in} and the optical power which arrives at the detector

$$P_{det} = P_{in} C S \times WGL_{det} \quad \text{A2-2}$$

By monitoring the input power and the power on the reference port, the exact photon flux at the detector can be calculated by

$$\Phi_{det} = P_{det} \frac{\lambda}{hc} = \frac{1}{2} P_{in} \sqrt{\frac{2P_{ref}}{P_{in} \times WGL_{ref}}} \times WGL_{det} \times \frac{\lambda}{hc} \quad \text{A2-3}$$

It should be noted that for this analysis that GC losses are assumed to be identical, which is a valid approximation for functional GCs.

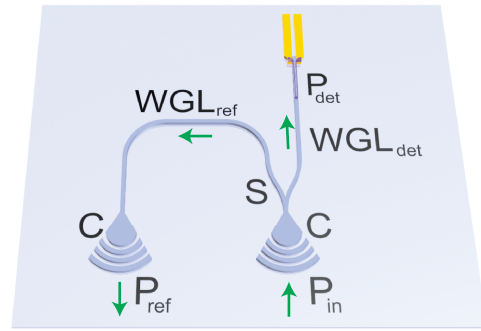


Figure A3-1: Photonic circuit layout for SNSPD OCDE characterization

ACKNOWLEDGMENTS

At this point in my thesis, I would like to express my gratitude to all those people who helped and supported me on my way toward the PhD.

First and foremost, I am immensely grateful to my advisor Professor Wolfram Pernice not only for giving me the opportunity to work on this exciting topic, but also for providing a friendly and scientifically stimulating environment. Wolfram gave me the freedom to explore my own ideas, provided guidance where necessary, and always lent a helping hand when needed.

Secondly, I would like to thank Professor Martin Wegener for co-advising and co-refereeing this work. We met several times throughout my PhD and I genuinely appreciate the critical, but supportive assessment that was given.

I am hugely indebted to Simone Ferrari and Vadim Kovalyuk. Most of the work presented in this thesis was a group effort and would not have been possible without Simone and Vadim. Simone is probably the most altruistic person I know. Without his help and support from setting up the cryo-measurement platform to proofreading this thesis, large parts of my work would not have gone as swiftly and unimpededly as they did. Vadim's prior experience with SNSPDs was invaluable for performing various experiments and would have likely not been as fruitful without him. Ultimately, large parts of this thesis were only possible because of their unyielding support – and, of course, the countless days and nights of measuring at the cryostat.

During my last measurements, I was happy to receive additional support from Andreas Vetter. Although he has been with the group only for a short time, he quickly became integrated into the team and his help was enormous.

I also want to express my gratitude to Stefan Kühn and Silvia Diewald at KIT's Center for Functional Nanostructures. Stefan and Silvia operated the electron beam lithograph which was an indispensable tool in the fabrication of my samples. I thank them both for fruitful discussions on how to optimize the related fabrication routines and, of course, for performing the lithography.

I, furthermore, would like to thank Nico Gruhler for his preparatory work on the silicon nitride platform including the development and refinement of the etch process. By the same token, Wladick Hartmann deserves mention for the initial development of the niobium nitride etch recipe.

Scientific progress lives through the exchange of ideas. In this regard, I would like to thank all the group members for the lively discussions we have had. Beyond that, I have had a really good time with everyone from working together on smaller projects to discussing different world views over lunch or coffee. The time of my PhD would have not been the same without the congenial atmosphere within the group of Anna Ovvyan, Nico Gruhler, Matthias Stegmaier, Patrik Rath, Svetlana Kasminskaya, Simone Ferrari, and, of course, Wolfram Pernice.

Lastly, I would like to thank my family and friends: my dad, Jens, for doing his best trying to explain quantum chemistry to an eight year old kid who wanted to know everything; my mom, Birgit, for being the supportive, kind-hearted soul in every situation of my life; my brothers, Marian and Julian, for being able to conquer the world together; my girlfriend, Susanne, for being here for me whenever I need her, especially during this writing period.